Using Molecular Design to Influence Intermolecular Interactions

Christine Laura Schenck

Submitted in partial fulfillment of the
requirements for the degree of
Doctor of Philosophy
in the Graduate School of Arts and Sciences

COLUMBIA UNIVERSITY

2013

ABSTRACT

Using Molecular Design to Influence Intermolecular Interactions

Christine Laura Schenck

This thesis describes the impact of molecular design on intermolecular interactions. Chapter 2 explores tuning the properties of contorted hexabenzocoronene (HBC) derivatives to improve photovoltaic performance. First, the interaction between contorted HBC derivatives with varying degrees of "bowl" character and fullerenes are explored in solution. Association constants were determined by fluorescence quenching experiments with fullerenes C_{70}, C_{60}, and Phenyl-C_{61}-butyric acid methyl ester (PCBM). NMR titration experiments mimic fluorescence quenching results that suggest that association in solution increases with shape-complementarity between donor and acceptor. Second, efforts towards the synthesis of azulene HBC, an HBC derivative with red-shifted absorption, are discussed. Calculations of this target molecule and a selected intermediate are compared to those of the parent contorted HBC. Finally, an azulene HBC synthetic intermediate is explored as a potential sensor. Chapter 3 presents a study of the single molecule conductance of cobalt chalcogenide clusters. The synthesis of cobalt chalcogenide clusters decorated with a variety of conjugated molecular connectors was developed. Single molecule conductance of these clusters was shown to take place through the molecular connectors, and was tunable by controlling the substitution of the connectors. The tunability of cluster conductance that was demonstrated in the single molecule experiments was shown to extend to thin film experiments in chapter 4. Preliminary investigation into the mechanism of conductance of these films is discussed. In chapter 5, a family of nickel telluride clusters with a variety of ligands is synthesized. The X-ray crystal structures of these clusters are analyzed and insight into how ligand sterics and electronics influence the final cluster structure is discussed.

TABLE OF CONTENTS

ACKNOWLEDGEMENTS

My experience as a graduate student in the Nuckolls lab has been an unforgettable journey, one that I could not have completed without the support of my advisor, professors, peers, and loved ones. I would like to express my gratitude to the many people who have been such a crucial part of my last four years. I am so grateful to have chosen Colin Nuckolls to be my graduate school advisor. He has shown me what it is to be a great scientist and has provided me the freedom to explore many subfields of materials chemistry and an environment of amazing scientists and tools to research in. His constant encouragement through good and bad research results gave me the strength to persevere and I will forever be grateful for his support of my choice to pursue a career in secondary education.

I would also like to acknowledge my committee members Jim Leighton and Mike Steigerwald for being a great support system throughout my time at Columbia. They made my second year defense and original research proposal truly valuable and even pleasurable experiences. Mike Steigerwald has been an amazing mentor. I have grown so much by conversing with him about science and life. I was hesitant to join the cluster project at first because of the unpredictable and mysterious nature of the research. Mike patiently taught me to embrace inorganic cluster chemistry and the “just try it and see what happens” attitude that the field sometimes requires. His scientific curiosity and insight is inspiring and contagious.

To the post-docs who have come and gone throughout my graduate career, you have had a lasting impact on me as scientists and friends. Kyle Plunkett and Brycelyn Boardman were the first post-docs to interact with me when I arrived and it truly was a warm welcome. I owe my introduction to cluster chemistry to Bryce and a lot of my organic synthesis technique to Kyle. In addition, most of chapter two was done in collaboration with Kyle during my first year. Thank you to both for the laughs and the ongoing friendships. I appreciate the time Alon Gorodetsky and Seok Ju Kang spent teaching me about solar cell device fabrication and Felix Fisher for the inspiring conversation. I am fortunate to have interacted with Bekka Klausen, who is a truly inspirational woman scientist. I shared desk space, conversation, and scientific ideas with Sujin

Wu and Kumar Bharat. I appreciate the editing suggestions given by Brandon Fowler, Christopher Bejger, and Bumjung Kim. All of these post-docs have made my graduate school experience pleasant and were a vital part of my scientific and personal development over the past four years.

I owe so much to Xavier Roy, who pulled me out of my research slump after what felt like unending disappointment. He believed in me as a scientist when I felt like I was a failure and invited me to join him on the cluster project. He spent a lot of time teaching me about proper organometallic synthesis techniques during my third and fourth year of graduate school, without which I would not have been able to perform most of the research in this thesis. He is an incredible scientist and has been a true pleasure to work with. To the rest of team cluster- Jaeeun Yu, Ari Turkiewicz, Chulho Lee, and Christopher Bejger- we have made a great team and have produced some amazing work. I will miss working with all of you.

To the many Nuckolls lab graduate students I was fortunate enough to share my experience with; you have all played an important role in my development as a scientist and as a person. The Nuckolls lab has to be the most pleasant and least dramatic work environment at Columbia because of all of you. I know we are all going to do amazing things, and I will miss you all. I would especially like to acknowledge Ying Wu for sharing the daily trials and tribulations of graduate school in our lab bay and Dan Paley for his helpful editing suggestions. K.O. Campbell and Michael Ewing provided me with administrative support so that I could focus on my research as well as non-science distractions when I needed them. They are both extremely intelligent and incredibly supportive. I appreciate all that they have done to help me complete my doctorate. In addition, I would like to thank Anna Ghurbanyan for her friendship and for the opportunity to be involved with the Columbia Science Honors Program. Without this experience, I may not have known that my true passion lies in secondary education. To the special friends I have made through this program, Paolomi Merchant, Markrete Krikorian, Gregory Chin, and Linda Suen, although we met in the context of chemistry, you have enriched my life in all aspects. I feel fortunate to call you all my friends.

I owe everything to my parents. They have been sacrificing for me and supporting me for my entire life and I could not have come this far without them. I thank my mom for instilling in me a “can do” attitude, the drive to be successful, and for teaching me about organization, presentation, and selflessness. I thank my dad for always pushing the limits of my knowledge, for the many intellectual conversations that shaped my ability to problem solve, and for providing me with a great example of a hard worker and an altruistic person. I love you both so much.

To Amedeo, my motivator, my distraction, my best friend, and my love; I could not have made it through graduate school without you. Just as we have persevered through the ups and downs of graduate school and emerged stronger, I look forward to sharing the ups and downs of life with you.

For My Family

“I don’t care how poor a man is; if he has family, he’s rich.”

-Dan Wilcox and Thad Mumford

Chapter 1. Introduction

In 1965, Intel co-founder Gordon E. Moore wrote a seminal paper describing his prediction that "the number of transistors incorporated in a chip will approximately double every 24 months."[1] This prediction has become a reality, allowing for extremely rapid advancement in a host of technologies. Today, technology is integrated into almost every aspect of our lives and has dramatically transformed social, political, and economic norms. Continuing the trend of "Moore's law" requires that transistors continue to shrink in size, with the current Intel transistor size being 22 nm. In a 1959 lecture, physicist Richard Feynman called for developments of bottom-up approaches to nanoscale device fabrication.[2] Since this lecture, there has been tremendous growth in the field of nanotechnology, which encompasses development of synthetic approaches to materials as well as development of nanoscale fabrication and device measurement.[3-5] This introductory chapter gives an overview of small molecule nanoscale electronic materials is provided, as well as a discussion of the types of electrical measurements used for small molecule devices.

1.1 Small Molecules as Electronic Materials

The first electronic materials were solid state compounds.[5] These solid state materials are generally metals or ionic solids formed by heating precursor materials to form the bulk, with little control over the fine structure. An alternative approach uses rational chemical synthesis to make electronic materials from the bottom-up. This relatively young field has explored polymers, organic small molecules,[7] inorganic complexes,[8] dendrimers,[9] molecular clusters,[10] and quantum dots[11] as materials for electronic and optoelectronic applications. This thesis focuses on the development and understanding of novel organic small molecules and molecular clusters as electronic materials. In this section, an overview of small molecule organic semiconductors and molecular clusters will be explored. Some of the mechanisms through which these molecules are known to electronically communicate will be discussed.

1.1.1 Small Molecule Organic Semiconductors

Organic semiconductors possess the ability to transport charge carriers. These molecules exist in the form of polymers or small molecules, and for the purpose of this thesis, only the latter will be discussed. It should be noted that small molecules offer the advantages of solubility, precise chemical structure, and reproducibility over their polymer counterparts.[7] π-conjugated molecules provide a delocalization pathway for carriers to flow. In addition, π-conjugated small molecules can form highly ordered stacks of two-dimensional sheets. These π-π interactions present a conduit for carrier delocalization across many molecules.[12] Recently, the number of small molecule organic semiconductors has expanded rapidly.[7,13] It is useful to categorize these molecules as electron donors (p-type semiconductors) or electron acceptors (n-type semiconductors), as this determines which applications the molecule is suitable for.

As the name implies, electron donors give up electrons in the presence of an appropriate electron acceptor. In order for this to happen, the donor's highest occupied molecular orbitals (HOMOs) must be high in energy relative to the electron acceptor's lowest unoccupied molecular orbital (LUMO). The resulting oxidized donor must exist as a stable species. Polycyclic aromatic hydrocarbons (PAH) represent one of the largest classes of electron donors, and this class of molecules is most relevant to this thesis.[14-16] Acenes, which can be characterized as linearly fused aromatic hydrocarbons, are the simplest set of molecules within this class.[17] Acenes have been isolated in sizes ranging from the smallest two-unit system, naphthalene, to the largest nine-unit system, nonacene (Figure 1.1a).[18] Pentacene and rubrene are the most well studied acenes in the class, and are the paragon for small-molecule organic field-effect transistors (OFETs) (Figure 1.1a).[19,20]

Larger PAHs extend in two dimensions, compared to the one-dimensional extension of acenes, and have been investigated for their superior light absorption and stability relative to acenes.[16] Their structure and properties can be tuned by varying the number and connectivity of aromatic rings. For example, placement of five benzene rings around a central cyclopentane ring

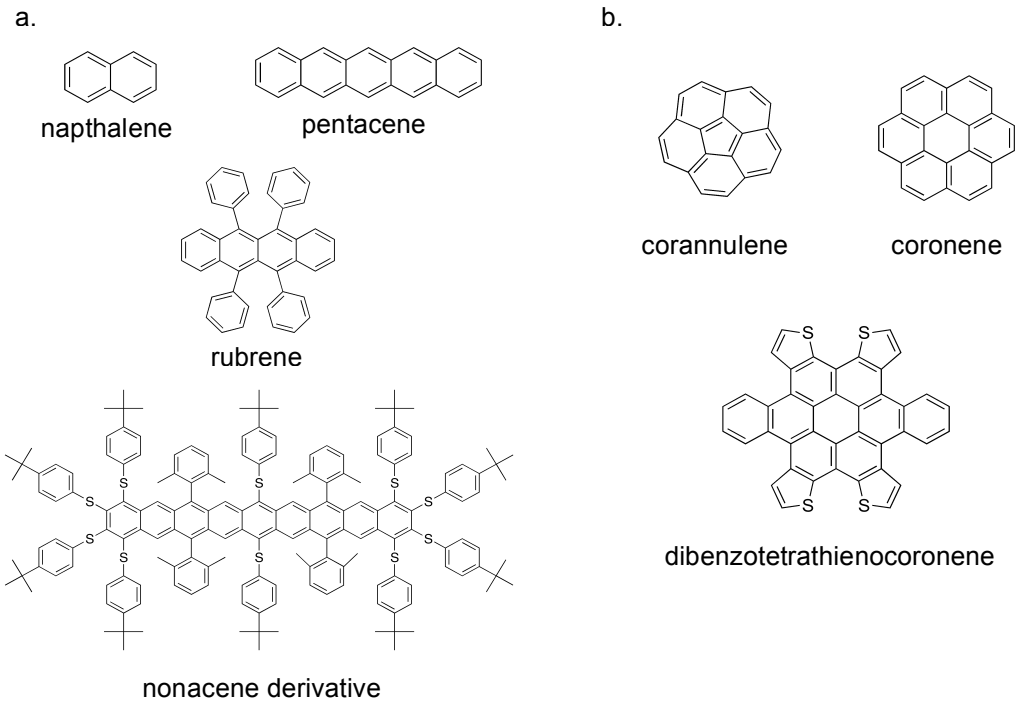

Figure 1.1. Examples of small molecule organic electron donors. a) Acenes b) Polycyclic aromatic hydrocarbons.

gives corannulene, a bowl-shaped structure, while placement of six benzene rings around a central cyclohexane ring gives coronene, a completely planar structure (Figure 1.1b). The electronic properties of PAHs are principally dependent on the size and external functionality of the molecules. Larger PAHs have wider windows of absorption and lower energy absorption due to extended π-conjugation.[21] However, larger PAHs suffer from limited solubility due to stronger π-stacking interactions.[21] Solubilizing alkyl chains are sometimes installed on the periphery to remedy this.[21] In addition, functionalization of PAHs by incorporating heteroatoms into the backbone or with peripheral electron-donating or -withdrawing groups can have a large impact on the functionality and packing structure of PAHs. Recently, Anthony and co-workers tuned the electronics of pentacene by incorporating cyano and trifluoromethyl groups to shift the HOMO and lowest occupied molecular orbital (LUMO) of pentacene from p-type to n-type (Figure 1.2a).[22] These n-type pentacene derivatives were shown to act as acceptors in solar cells with P3HT.[23] Installation of thiophene units into a contorted hexabenzocoronene structure has been shown to

change the intermolecular packing structure of the molecule through sulfur-sulfur interactions (Figure 1.1b).[24]

The synthesis of PAHs relies heavily on reaction chemistry that achieves fused aromatics. The development of catalytic aryl-aryl coupling reactions, such as Suzuki[25] and Heck,[26] has progressed with the field of synthetic materials chemistry, providing a large toolset for building PAH systems. Cyclization reactions also play an important role, by either building up the PAH framework or, in the case of photocyclizations,[27] closing bonds of an existing framework to expand aromatization. Another important method of aromatic cylization is the Scholl reaction, which accomplishes Lewis acid assisted oxidative intramolecular aryl-aryl bond formation.[28]

The counterpart to electron donors is the class of organic semiconductors known as electron acceptors. These molecules have lower energy HOMO-LUMO levels and are relatively stable in

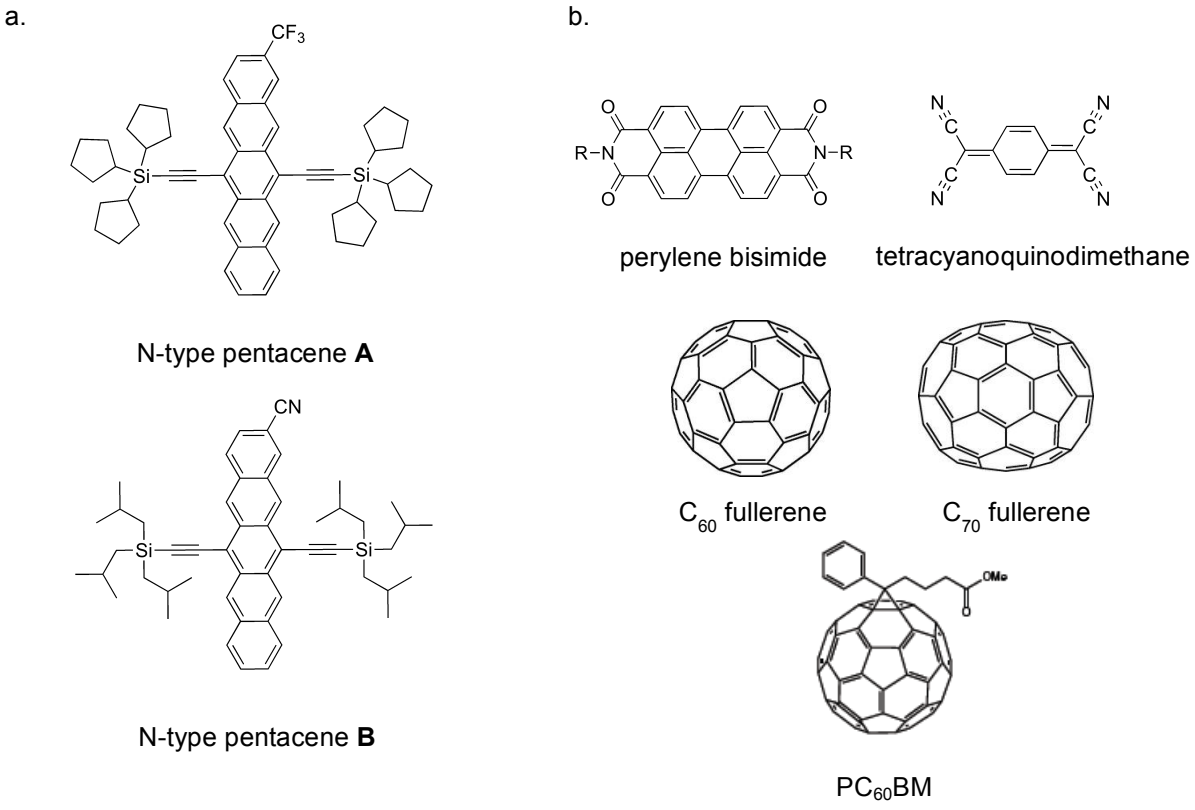

Figure 1.2. Examples of small molecule organic electron acceptors. a) n-type pentacenes b) common families of acceptors. R = alkyl chains

the reduced form. There are fewer known electron acceptors than electron donors. This is largely due to the fact that organic anions are less stable in air than organic cations.[29] There are three main classes of n-type semiconductors: fullerene, perylene bisimide, and tetracyanoquinodimethane (TCNQ) (Figure 1.2).[7] Of these, fullerenes are the most widely used of the three and are the only acceptor used in this thesis.

In 1985, Kroto, Curl, and Smalley discovered a new allotrope of carbon that has become one of the most popular electron acceptor materials.[30] This discovery eventually won them the Nobel Prize in Chemistry. This new allotrope of carbon was composed of a number of six and five-membered rings fused to form a spherical cage. These carbon molecules, called "fullerenes," form with an even number of carbons. C_{60} and C_{70} are the most widely used, although C_{72}, C_{76}, C_{84}, and C_{100} can also be obtained (Figure 1.2b). In each of the fullerenes, there are 12 pentagons, each surrounded by a number of hexagons determined by the fullerene size. Each carbon is bonded to three other carbons, making them sp^2 hybridized. Fullerenes are air stable, fairly soluble in organic solvents, and can accept between four and six electrons, depending on

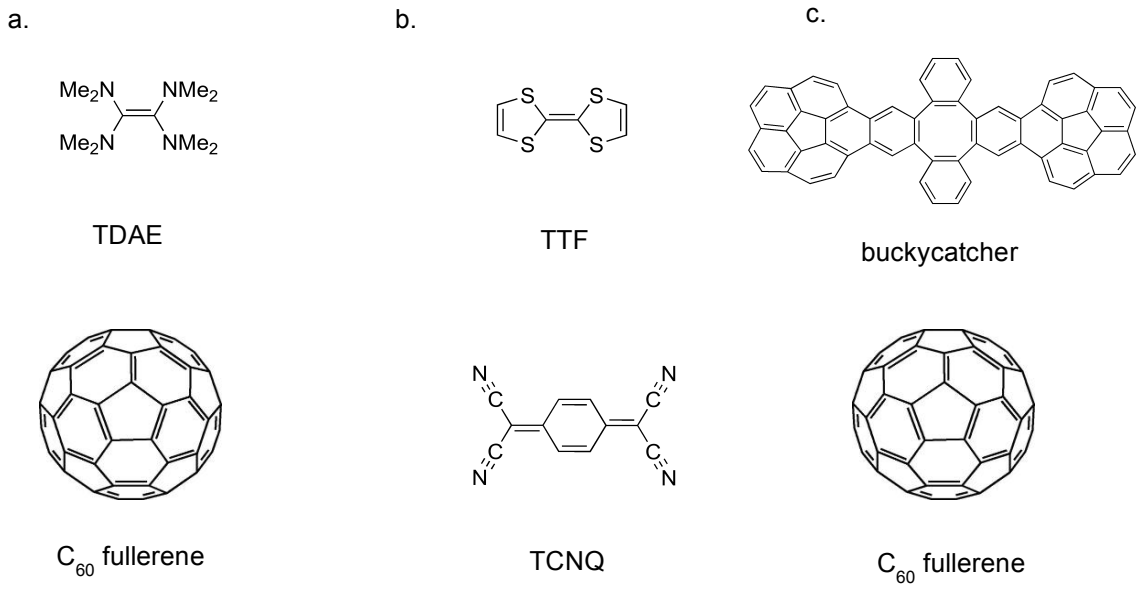

Figure 1.3. Examples of charge transfer complexes. Donor material is shown on top, and acceptor material is shown on bottom. a) Complete charge transfer complex between TDAE and C_{60} fullerene. b) Partial charge transfer complex between TTF and TCNQ. a) Supramolecular complex between buckycatcher and C_{60} fullerene.

the fullerene. More soluble forms of fullerenes, such as phenyl-C61-butyric acid methyl ester ($PC_{60}BM$) and phenyl-C71-butyric acid methyl ester ($PC_{70}BM$), retain the favorable stability and accepting power of their unsubstituted counterparts (Figure 1.2b).[31] A complete review of fullerene chemistry and properties can be found elsewhere.[32,33]

While charges flow through the crystal lattice of solid state materials within an electronic device, small molecules rely on intermolecular interactions for electronic communication. π-π stacking was mentioned previously as an important structural feature in small molecule design for electronic materials. This π-π stacking is a very weak intermolecular interaction that encourages close packing and electronic communication of large π-conjugated molecules. However, to get very conductive materials, a gradient is necessary within a device to encourage charge transport through the material. This gradient can come in the form of an external electric field, such as that in a field effect transistor (FET), or in the form of charge transfer interactions between donors and acceptors, such as that found at the interface of a solar cell.[34]

Charge transfer complexes have been vital to the development of organic small molecule electronics. In 1973, a charge transfer complex comprised of tetrathiofulvalene (TTF) and tetracyanoquinonedimethane (TCNQ) became the first example of an organic system with metallic properties and conductivities as high as 100 $\Omega^{-1}cm^{-1}$ (Figure 1.3b).[35] Prior to this discovery, several examples of organic charge transfer complexes with semiconducting properties had been observed.[36]

Charge transfer complexes can be categorized based on degree of charge transfer. Complete charge transfer results in the formation of a radical ion-pair ($D^{n+}A^{n-}$), whose strong intermolecular interactions give interesting properties.[37] An ionic salt is formed between tetrakis(dimethylamino)ethylene (TDAE) and C_{60} fullerene that shows a ferromagnetic transition at a high temperature relative to other organic systems (Figure 1.3a).[38] TTF-TCNQ is an example of a partial charge transfer, where the complex can be represented as $D^{\delta+}A^{\delta-}$ (Figure 1.3b).[35] Finally, charge transfer that is close to zero is the result of a supramolecular complexes. Concave-convex π-π interactions, such as that between a “buckycatcher” and fullerene (Figure

1.3c) have recently been explored as supramolecular complexes with fairly high association constants.[39]

In Chapter 2 of this thesis, the interaction between a family of contorted hexabenzocoronene small molecule organic electron donors and fullerene electron acceptors was investigated as a function of shape matching. These solution studies indicate the importance of shape complementarity for the formation of supramolecular complexes and for electronic interactions; work that could have implications for molecular design of molecules at device interfaces. In the second part of Chapter 2, the electronics of a small molecule organic electron donor material, contorted hexabenzocoronene, is tuned to absorb longer wavelength light by functionalization with azulene.

1.1.2 Molecular Clusters

Solid state semiconductors have been the material of choice during the development of electronics. However, production of these materials generally requires very high temperatures, which is costly on an industrial scale. In addition, there is often no ability to design new solid state semiconductor materials, as their chemical structure is largely unpredictable and not well understood. In an effort to understand how bulk semiconductors form from precursors, nanocrystals were investigated as intermediates in this process.[40,41] These nanocrystals can be thought of as small chunks of semiconductor, usually less than 100 nm in diameter, that are capped with ligands to keep them from aggregating. They were shown to have unique properties as compared to their solid state relatives, including optical and electronic effects of quantum confinement.[42] Within this relatively small size range, many different types of nanocrystals have been synthesized and characterized. Larger, monodisperse semiconductors are generally referred to as quantum dots, and have been studied extensively as optical and electronic materials in the literature.[43,44] In contrast, while many atomically precise molecular clusters have been isolated and characterized, their materials applications have been largely unexplored. These molecular clusters offer advantages of solubility and tunable structural diversity over solid state compounds, and structural characterization with X-ray diffraction techniques over

monodisperse quantum dots.[45] In this thesis, metal chalcogenide molecular clusters will be synthesized and investigated as electronic materials.

Metal chalcogenide molecular clusters are particularly attractive as a class of molecules with tunable structures and properties, which stems from the ability to choose almost any combination of transition metal, chalcogen (S, Se, or Te), and ligand. Changing the metal in the cluster can have large impacts on the electronics of the resulting molecular cluster. For example it is easy to imagine that a molecular cluster containing early transition metals will have a very different electronic structure than that of clusters containing middle or late transition metals. For example, one of the largest structural families of metal chalcogenide molecular clusters is the

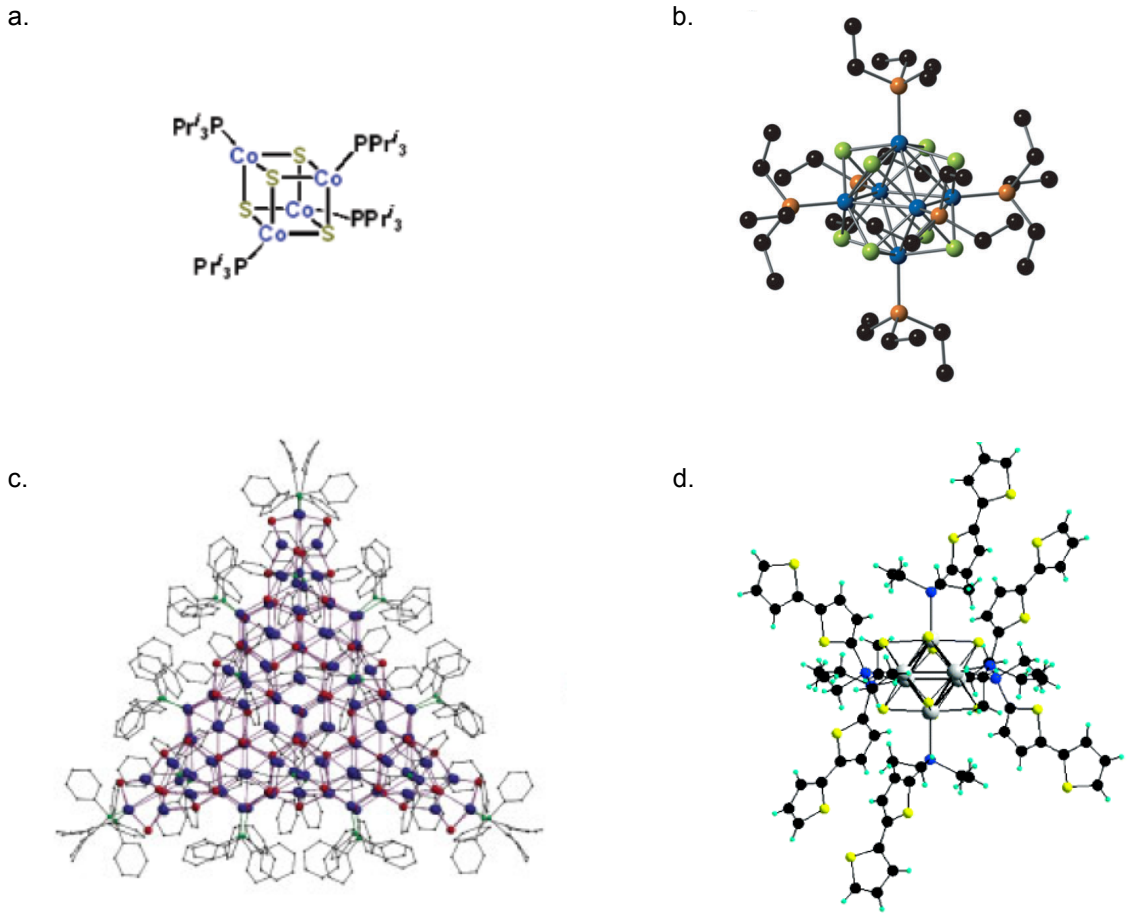

Figure 1.4. Examples of molecular clusers. a) Cubane cluster shape; $Co_4S_4(P\textit{i}\text{-}Pr_3)_4$ b) octahedral $M_6Ch_8(PR_3)_6$, where Ch is blue, M is green, PR_3 is orange, and black is carbon. c) $Cu_{146}Se_{73}(PPh_3)_{30}$, where P is green, Se is red, and Cu is blue. d) $W_6S_8(PR_3)_6$ where R is dithiophene, P is blue, S is yellow, W is white, C is black, and H is teal.

cubanes, M_4Ch_4, where M is metal and Ch is chalcogenide (Figure 1.4a). This cluster core has been explored with a variety of metals and can be described as the outer four metal atoms of a tetrahedron overlaid with the outer four chalcogenide atoms of a tetrahedron to form a cube, with each metal bound to three chalcogenides and each chalcogenide bound to three metals.[46-49] Middle transition metals, such as cobalt[48] and iron,[47] have been shown to form electron-rich cubanes with a valence electron count of 72 while early transition metal cubanes, such as $Ti_4S_4(i\text{-}PrCp)_4$[46] give an electron-deficient species with 52 valence electrons. In other cases, the diversity in reactivity between early, middle, and late transition metals produces different cluster cores. In addition to reactivity, the availability of metal precursors dictates the synthetic strategy and the types of cluster cores that are accessible for that metal.

Changing the chalcogenide is another way to tune the properties of clusters. The octahedral $M_6Ch_8L_6$ cluster family, where L is ligand, is a well known example of this (Figure 1.4 b).[50] Changing the chalcogenide of the cobalt cluster leaves the structure largely unchanged, while producing a significant shift in the optical absorption. From S to Se to Te, the absorption moves to longer wavelengths, although in all cases there are three transitions observed. In other cases, such as the family of copper chalcogenide clusters synthesized from silylated chalcogenide precursors, different chalcogenides produce different cluster structures as a result of difference in electron affinities, ionization potentials, and size between chalcogenides.[51,52] This has led to an extremely diverse structural library within this family and has produced some of the largest metal chalcogenide molecular clusters, including the $Cu_{146}Se_{73}(PPh_3)_{30}$ (Figure 1.4c).[53,54]

Ligand structure also has a large impact on molecular cluster structure and properties. Ligands in particular have the potential to be the most diversifiable synthetic handle on molecular clusters. The choice of capping ligand a particular cluster is dictated by the method of cluster synthesis. For example, the reaction of a phosphine chalcogenide with a M(0) source gives a metal chalcogenide molecular cluster where L is a phosphine.[50,55,56] In contrast, soluble chalcogenide anions, formed by reduction of chalcogenide with an alkali metal, can react with metal salts or metal carbonyls to form chalcogen-capped clusters or carbonyl capped clusters.[57-59] Added complexity results from the fact that the choice of capping ligand also dictates the size

and structure of the resulting cluster. For example, when bis(cyclooctatetraene)iron is reacted with phosphine telluride, the resulting cluster structure is shown to be dependent on the phosphine ligand.[56] Triethylphosphine and bulkier triisopropyl phosphine both give an Fe_4Te_4 cluster while trimethylphosphine gives a larger Fe_6Te_8 cluster core.[56]

Choice of ligand on a molecular cluster can control the intermolecular communication and spacing, a vital consideration for the use of molecular clusters in electronic devices. In an effort to enhance inter-cluster communication, DiSalvo and co-workers have done extensive work to incorporate ligands, such as cyano ligands,[60] hydrogen bonding ligands,[61] and thiophene ligands[62] that create, or have the potential to create, networks of clusters (Figure 1.4d). However, resulting networks have proven difficult to fully characterize due to solubility or stability problems. There is an ongoing effort to achieve covalently linked cluster networks.

Molecular clusters are redox active and possess discrete energy levels, atomic-level structural characterization, solubility and structural diversity and tunability. While an extensive library of molecular clusters has been built up, there has been little work to apply these molecular clusters as materials in electrical devices. This thesis is mostly concerned with ligand chemistry and its effect on cluster formation and intermolecular communication in the context of electrical transport. In chapter 5, the impact of phosphine structure on nickel telluride cluster formation is explored. In chapter 3, a set of novel aromatic phosphine ligands are installed on Co_6Se_8 clusters as pathways for communication through normally insulating ligands, with single molecule conductance used to evaluate the efficacy of these pathways. In chapter 4, this intermolecular communication demonstrated with single molecule conductance is shown to translate into cluster thin films.

1.2 Electronic Measurements

Design and synthesis of small molecules for electronic applications is only part of the challenge of molecular electronics. These small molecules must then be tested within electrical devices to determine their performance. While our understanding of how small molecule structure influences performance in electrical devices has grown significantly, theoretically predicting the

performance of a small molecule within a device is still difficult. In this section, an overview of electrical measurements on small molecule devices will be given. First, single molecule conductance measurements will be discussed. Next, small molecule thin films and modes of transport through small molecule thin films will be discussed. Finally, an introduction to solar cells will be given.

1.2.1 Single Molecule Conductance Measurements

In principle, the simplest electrical device is composed of a single molecule wired to two electrodes. However, constructing such a device is far from simple, demonstrated by the fact that single molecule devices are being developed long after the discovery of bulk film devices. Some of this complexity lies in the fact that single molecules are physically difficult to manipulate. Constructing a connection between the single molecule and the necessary electrical contacts and understanding how this interface affects the measured conductance presents significant hurdles.[63] Another significant complexity lies in the lack of fundamental understanding of charge transport on the molecular level, which is presumably much different than that of the micro and even nanoscale.[63] Much recent work has been done to develop the theoretical and experimental tools to begin to understand this rich area of research.[63-70] Because of the expansive amount of work being done in this area, this section will only introduce the necessary background and recent work that is relevant to the research performed in this thesis.

Scanning tunneling microscopy was developed in 1981 as a technique for atomic imaging.[71,72] During an STM measurement, a probe tip is brought very close to the surface of a sample. The probe tip is extremely small, with the tip being comprised of a single atom. A voltage bias is applied between the tip and the sample to induce quantum tunneling. Because quantum tunneling is very sensitive to distance, a piezoelectric is necessary to precisely control the location of the tip with respect to the sample in three dimensions. In addition, the quantum tunneling current observed is dependent on the density of states of the sample. As the tip is scanned across the sample, the changes in tunneling current as a result of both distance of the tip from the sample and the density of states of the sample are mapped to produce an image.[73]

STM was modified to create a break junction technique (STM-BJ) utilized for single molecule conductance measurements.[74] An illustration of this technique is shown in Figure 1.5. In this technique, the probe tip, typically made of gold, is brought into direct contact with a substrate

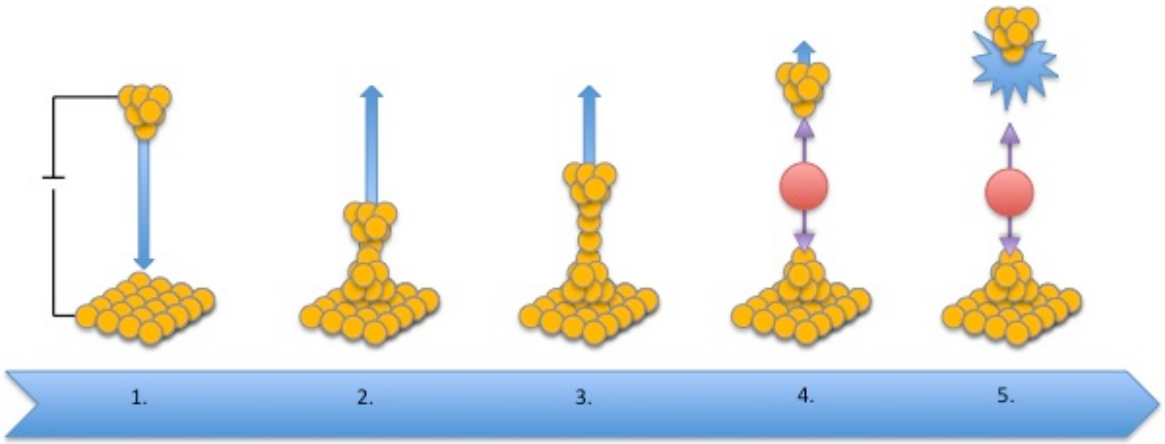

Figure 1.5. Cartoon depiction of STM single molecule junction measurements. 1) Tip is smashed into substrate. 2) Tip is pulled away from substrate 3) As tip is pulled away, a single gold atom bridges the junction. 4) If there is no solution, the gold junction breaks and conductance drops significantly. If there is a solution of molecules, one may be trapped between the gold electrodes to give a plateau on the conductance trace. In this cartoon, a molecule is represented as a red circles with functional groups to bind electrodes depicted as purple arrows. 5) When the gold tip is pulled away farther, the single molecule junction is broken and conductance drops significantly. This process is repeated many times.

electrode, also gold, to form a complete circuit. The tip is then pulled away from the substrate until the contact is broken, with current measured throughout the process. This break in the junction can be observed as a significant decrease in current as a function of distance of the tip from the substrate. An example of the conductance trace as a function of tip displacement is shown in Figure 1.6 (left). When a solution of molecules that can bind to the gold electrodes is introduced, a molecule is occasionally trapped in the broken junction. This event can be observed as a plateau on the conductance trace (Figure 1.6, middle). The whole process of forming and then breaking the junction is on the order of milliseconds, allowing for thousands of conductance traces to be observed and then statistically analyzed to account for variations in the junctions being formed, caused by variability in molecule-electrode binding and molecule geometry. The conductance traces are compiled into a histogram from which the most probable conductance

value is determined (Figure 1.6, right). The conductance of the single molecule is measured in units of quantum conductance, G_0. G_0 can be defined by

$$G_0 = 2e^2/h$$

where *e* is the electron charge and *h* is Planck's constant and represents the conductance of a single atom bridging two electrons, where the composition of the two electrons is the same as that of the bridging atom.

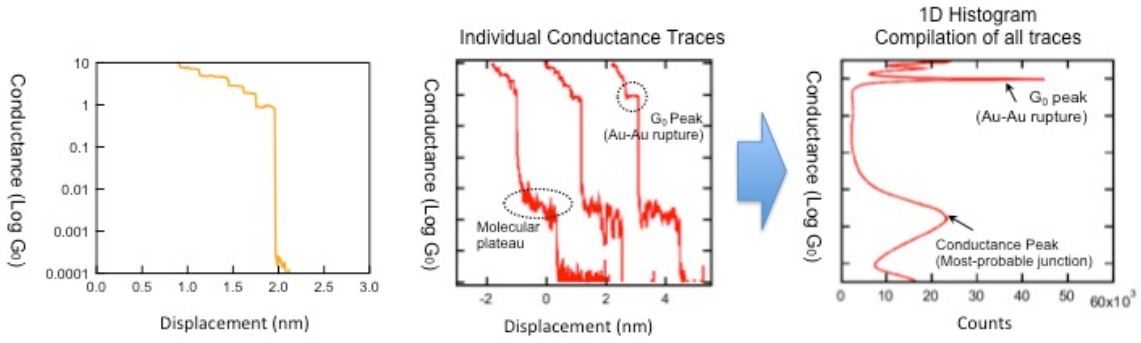

Figure 1.6. Examples of STM-BJ data. Left) Conductance trace of gold tip and substrate without a solution of molecules. As displacement is increased, the conductance decreases slightly. At the break of the junction, conductance decreases dramatically. Middle) When a solution of molecules is placed on the substrate, a molecular plateau is observed when a single molecule is trapped between the tip and substrate. This plateau is observed after gold-gold rupture, but before complete junction disconnection. Right) Compiling many conductance traces into a 1D histogram gives the a conductance peak from which the most probable conductance can be observed.

The SMT-BJ technique requires that the molecule contain functional groups that can bind to gold. Linker groups such as primanry amines, thiomethyls, and dimethylphosphine show sharp and consistent single molecule conductance traces.[75] Other linker groups include carboxylic acids, pyridines, and cyano groups.[76-79] Experiments have been performed to demonstrate that the point of contact between electrode and sample molecule is in fact through these linker groups on the sample molecule. For example, absence of a linker group shows no conductance and sterically bulky alkyl chains on linker groups turn off conductance by inhibiting binding of the linker to gold.[78]

Several studies have confirmed the importance of linker group placement on phenyl terminated conjugated molecules.[80-81] A set of stilbene molecules in which thiomethyl linker

groups are placed at the *meta* or *para* position is shown in Figure 1.7. When two thiomethyl linker groups are placed in the *para* position, a sharp conductance peak is observed at high conductance (10^{-3} G_0) (Figure 1.7a). When one *para* linker is installed and there is no linker group on the other end of the molecule, conductance broadens and decreases significantly, indicating a weak interaction between the half of the molecule lacking a thiomethyl group (Figure 1.7d). When the linker groups are placed with one in the *meta* position and one in the *para* position (Figure 1.7b), conductance increases from that of the single *para* linker molecule, however it remains less than that of the molecule with two *para* linkers. This decrease in conductance is presumed to be because the *meta* linker, while providing an anchor for the electrode, is

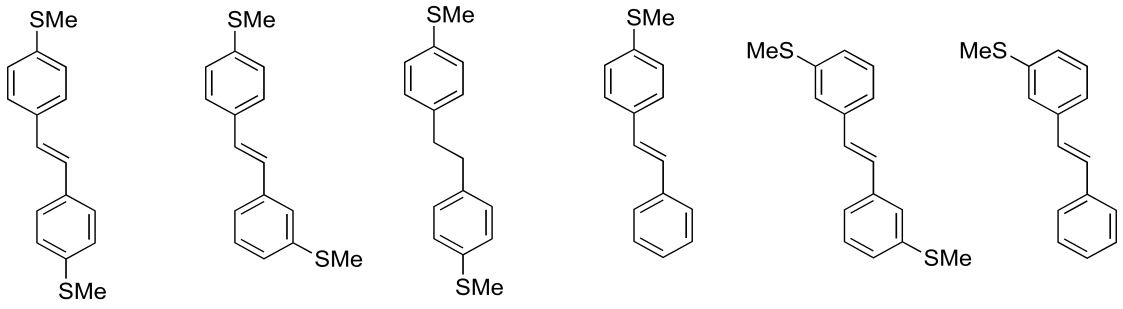

A	B	C	D	E	F
1.2×10^{-3} G_0	2.9×10^{-4} G_0	3.2×10^{-5} G_0	2.1×10^{-5} G_0	N/A	N/A

Figure 1.7. A series of stillbene molecules that have been measured by the STM-BJ technique. Above) Molecular structures of stillbenes with various thiomethyl substitutions. Below) Single molecule conductance values obtained from STM-BJ technique.

not in resonance with the *π*- system. This is further confirmed by the fact that a stilbene molecule with either a single *meta* placed linker group and no opposing linker group or two *meta* placed linker groups show no detectible conductance (Figure 1.7f, e). The importance of the *π*- system was demonstrated by a stilbene derivative with two para placed linker groups in which the conjugation is broken by a saturated ethyl bridge (Figure 1.7c). This molecule showed lower

conductance than its fully conjugated relative. The lessons learned through these experiments will be applied to more complex metal-organic molecular clusters in chapter 3 and 4.

While there has been a significant amount of research on the single molecule conductance of a variety of organic molecules, there are only a few examples of single molecule conductance measurements of organic-inorganic hybrid materials.[82,83] In chapter 3, the single molecule conductance of a variety of metal chalcogenide molecular clusters with organic ligand shells is measured. Tuning of the conductance is demonstrated by changing the ligand structure. In chapter 4, thin films are constructed from two of the clusters whose single molecule conductance was measured in chapter 3. These thin films show the same trend of conductance as in chapter 3. This provides an interesting case study because single molecule conductance is often not correlated to the thin film conductance of the same molecule, due to the significant increase in system complexity.

1.2.2 Small Molecule Thin Film Conductance Measurements

Moving from single molecule electronic devices to small molecule thin film devices adds many modes of complexity. Successful movement of charge through the films requires effective molecule-molecule interactions and molecule-electrode interactions, both of which depend on many variables including molecular orientation, presence of impurities and defects, and molecular interaction with the substrate, to name a few. Despite the significant amount of complexity involved, there are many examples of conductive small molecule thin films.[17, 84-90] This section overviews some of the theory of conductivity as well as measurement and fabrication techniques used to study conductive small molecule thin films.[91,92]

Conductivity (σ) is a property of a material that describes how well electrical current passes through the material. It is related to the conductance (G), or the ease with which electrical current flows through a sample of a particular length (*l*) and area (A), by the following equation:

$$G = \sigma \frac{A}{L}$$

A similar relationship exists between resistance (R) and resistivity (ρ), where only resistance is dependent on the length and area of the sample:

$$R = \rho \frac{l}{A}$$

The conductivity and resistivity of a material are therefore reciprocals such that:

$$\rho = 1 / \sigma$$

There are two main ways in which resistivity and conductivity of a given material are experimentally determined: a four-probe method and a two-probe length dependence method (Figure 1.8). Both of these methods aim to minimize or remove parasitic resistance, which can stem from the contact resistance (R_c) at the interface between the material and electrodes.[93]

Four-point probe measurements separate the area of applied current and measured voltage to minimize the parasitic resistance. Four electrodes, generally evenly spaced, are placed on the thin film to be measured and current is applied between two of the probes while voltage between the other two probes is measured. There are several methods of spacing the probes, including the Four-In-Line, Montgomery, and the Van der Pauw techniques, although an overview of these are beyond the scope of this thesis. The resistivity from four-point probe measurements can be calculated from the inverse slope of the experimental current (I) - voltage (V) plot, with an additional correction factor determined by selection of four-point probe technique, film thickness, length, and area.

In contrast, the length dependence technique utilizes only two-probes and varies the length between electrodes to remove parasitic resistance. In this technique, several electrodes are placed with increasing distance between pairs of electrodes, essentially creating many two-electrode devices on the film with varying device lengths. An I-V plot is generated for each two-probe device and a plot of the resistance of each device, calculated from the inverse of the I-V plot slope, versus the length to width ratio for that device gives a linear relationship. The slope of this line is the desired sheet resistance of the material, while the contact resistance is the y-

intercept. In this way, parasitic resistance can be excluded. The resistivity is then determined by multiplying the sheet resistance by the film thickness.

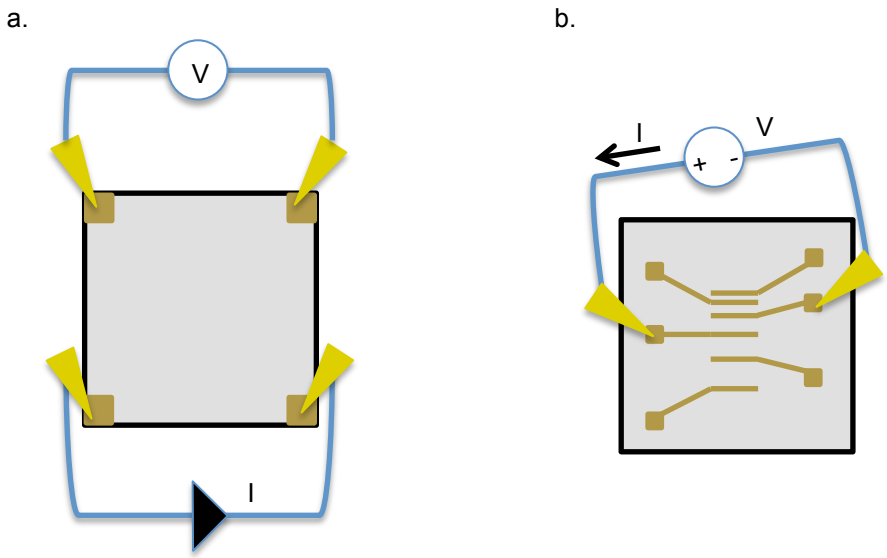

Figure 1.8. Two methods of measuring conductivity and resistivity. Where gold squares represent electrodes, gray represents a thin film, yellow represent probes, V is voltage, and I is current. a) four-point probe technique b) two-point length dependence technique.

Electronic materials are classified according to band structure and the type of carrier (electron or hole) that is transported (Figure 1.9).[94] In films of conductor materials, there is no band gap (E_g) so electrons occupy the conduction band (CB). These electrons in the CB are the carriers. In semiconducting materials, there is a small E_g such that vacancies in the valence band (VB) or electrons that have been thermally excited to the CB act as carriers. When holes are the carriers, the material is a p-type semiconductor and when electrons are the carriers, the material is an n-type semiconductor. Small molecule conducting materials are generally semiconducting in nature. Distinguishing between conducting and semiconducting materials requires temperature-dependence measurements.[95] Conducting materials generally have quite low resistivity ($<10^{-4}$ Ω•cm) at room temperature because they have large numbers of carriers already in the conduction band. Increasing the temperature of the device increases the resistivity of the material due to phonon scattering. In contrast, semiconducting materials have moderate resistivity values

(10^{-3} Ω•cm to $<10^{11}$ Ω•cm) that decrease with increasing temperature. This is due to an increase in the thermally populated conduction band of the material at higher temperatures causing an increase in charge carriers.

Determining whether a semiconductor primarily carries holes (p-type) or electrons (n-type) requires the construction and measurement of a field effect transistor (FET). In an FET, current is measured across a device through source and drain electrodes while an electric field is applied through a third gate electrode. The applied electric field is used to build up charge, either

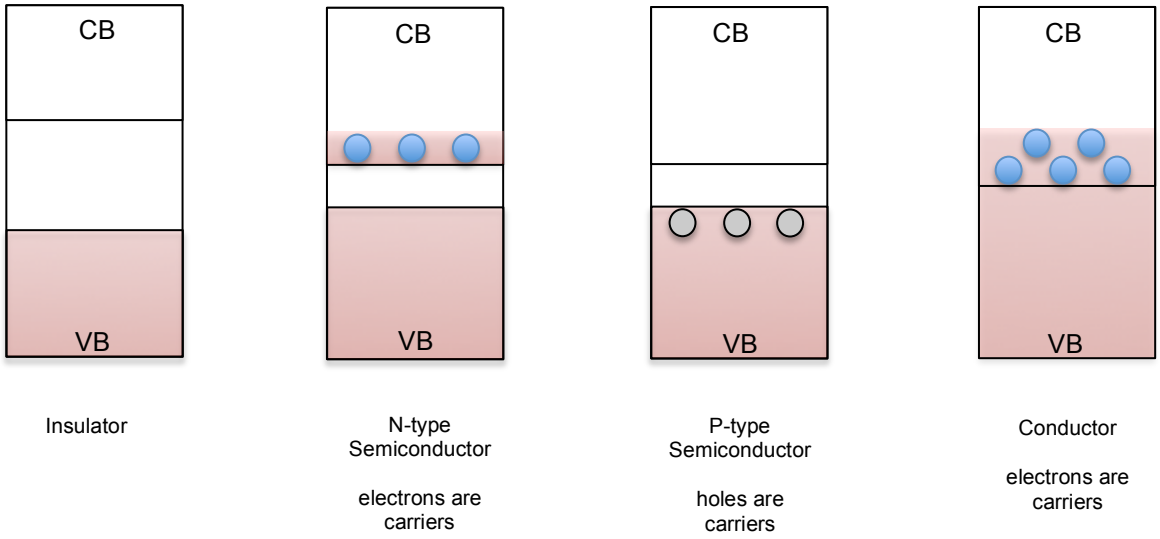

Figure 1.9. Band structure and charge carriers associated with insulators, n-type semiconductors, p-type semiconductors, and conductors. Blue represents electrons as carriers, grey represents holes as conductors, and red represents filled energy states.

holes or electrons, in the thin film depending on the direction of gate voltage.

In addition to the type and number of carriers, conductivity of a small molecule thin film depends on the ability for these carriers to move through the film. This means that the morphology of the film is extremely important in determining how well the individual molecules interact with each other, and in turn how well the charge can move from one molecule to the next through the film. Mobility, or the ability for charges to move through a film in response to an electric field, can be calculated using an FET.[91] In addition, mobility can be used in conjunction with conductivity to calculate the number of charge carriers in a film.[91]

In chapter 4 of this thesis, the conductivity and resistivity of thin films made of atomically precise molecular clusters is determined. While molecular clusters have been investigated for their interesting magnetic and structural properties, there have been few reports of their utilization in electrical devices. The understanding of charge transport through the single molecule gained in chapter 3 is used to design conductive thin films in chapter 4. Also, a discussion of the link between single molecule conductance and thin film conductivity is discussed.

1.2.3 Solar Cells

In 1839, Edmond Becquerel discovered the photoelectric effect when he noticed an increase in the current of an electrolytic cell upon illumination.[96] This experiment fueled a number of experiments throughout the 1800s, culminating in Albert Einstein's seminal paper on the photoelectric effect.[97] This work laid the foundation for solar energy as a largely abundant and clean source of electrical power, although solar cells only became widely commercially available after the development of the silicon solar cell in 1954 at Bell Laboratories.[98]

Silicon solar cells are made of a layer of p-doped silicon and n-doped silicon that form a p-n junction.[99] When illuminated, semiconducting silicon absorbs photons with the appropriate energy and produces electron-hole pairs. The electric field intrinsic to the p-n-junction drives the movement of these newly produced charge carriers through the conduction band, resulting in the collection of current with device efficiencies of up to 27.6%.[100] High performance silicon solar cell devices require extremely high quality single-crystal silicon because any imperfections in the crystal can act as traps for the charge carriers, ultimately negatively impacting the efficiency of the device. Only 7% of the U.S. energy comes from renewable energy sources, including wind, solar, and hydropower.[101]

Although there have been significant improvements in the cost of silicon solar cell manufacturing, the development of other solar cell materials is an extremely active area of research. Organic solar materials have provided an attractive alternative to silicon solar cells due to their potential to produce flexible solar cells with less expensive manufacturing techniques, such as printing. Organic photovoltaic (OPV) devices work in a fundamentally different way than

the silicon solar cell because they are made of molecular materials rather than bulk materials.[102] An OPV is comprised of an electron donor material and an electron acceptor material, with each attached to an electrode (Figure 1.10). The HOMO and LUMO level of the donor must be higher in energy than the acceptor, but the HOMO level of the donor cannot exceed the LUMO energy of the acceptor.

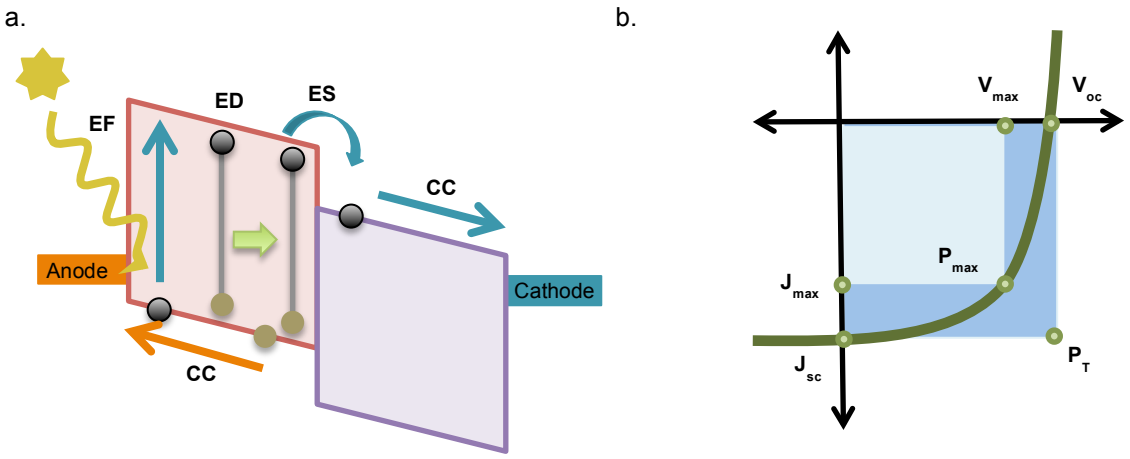

Figure 1.10. Cartoon of organic photovoltaic mechanism and representative data. a). Proposed mechanism for OPVs. Red box is electron donor, purple box is electron acceptor (top of box is LUMO, bottom of box is HOMO), EF is exciton formation, ED is exciton dissociation, ES is exciton separation, CC is charge collection, black circles indicate electrons, tan circles indicate holes, blue arrows indicate path of electron to cathode, orange arrow indicates path of holes, and green arrow indicates movement of exciton. b) J-V curve of an organic photovoltaic device with illumination is shown in green. Dark blue box indicates the theoretical power maximum, calculated from the open circuit voltage (V_{oc}) and short circuit current (J_{sc}). The maximum power of the observed curve is indicated by the light blue box, from which the maximum voltage (V_{max}) and maximum current (J_{max}) are calculated.

Upon illumination, photons are absorbed by the donor material to create an exciton (Figure 1.10a, EF). The exciton differs from the electron-hole pair generated in the silicon solar cell because, while the electrons and holes are free to move in the conduction band of silicon, the electron and hole in the exciton must diffuse together towards the donor-acceptor interface (Figure 1.10a, ED). Once at the interface, the higher energy electron in the LUMO of the donor moves to the lower energy LUMO of the acceptor (Figure 1.10a, ES). At this time, the exciton has separated and the electrons proceed through the acceptor layer towards the electrode for collection while the holes proceed through the donor layer to be collected at the other electrode,

thus creating current (Figure 1.10a, CC). A a typical current-voltage (J-V) curve is shown in Figure 1.10b. Efficiency (η_p) of the OPV can be calculated using the equation:

$$\eta_p = \frac{J_{sc} \times V_{oc} \times FF}{P_{in}}$$

where J_{sc} is the short circuit current, V_{oc} is the open circuit voltage, FF is the fill factor, and P_{in} is the input power. The J_{sc} is the maximum generated current density upon illumination when no voltage bias is applied. The V_{oc} is the maximum voltage allowed when no current is flowing. In a simplified model, the V_{oc} is determined by the energy gap between the HOMO of the electron donor and the LUMO of the electron acceptor, with a larger gap resulting in a higher open circuit voltage. The fill factor is defined by the following equation:

$$FF = \frac{J_{max} \times V_{max}}{J_{sc} \times V_{oc}}$$

The efficiencies of OPVs are significantly lower than silicon solar cell efficiencies, with a highest recorded efficiency of 12.0%.[100,103] This is partially due to the fact that OPVs are not made of bulk crystalline materials but are instead molecular in nature, resulting in traps and grain boundaries that inhibit exciton movement and ultimately charge collection.[103] Another reason why they are typically less efficient is because of charge recombination.[103] Since the electron-hole pair must move as an exciton through the donor material in an OPV rather than as an electron and hole that can diffuse away as in the silicon solar cell, there is more time for the excited electron to relax to the ground state. In addition, charge collection is dependent on the separation of the exciton at the interface. Studies have shown that the molecular design has a high impact on the interaction of donor and acceptor at the interface, which is crucial to higher efficiency OPVs.[104] Shape-complementary donor-acceptor interactions will be studied in solution in chapter 2, with the hope of gaining insight into how molecular design impacts solar cell interfaces.

It should be noted that, while this thesis does not directly investigate molecular clusters in solar cells, it does lay some foundation for utilizing this interesting class of materials in thin film

devices such as photovoltaics. Atomically defined quantum dots act both as small molecules in terms of possessing discrete energy levels, solubility, and a lack of long range crystallinity, while also representing the bulk material with a crystalline, metal-rich core. This makes them an extremely complex system that is largely underexplored in electronic devices. The author hopes that the fundamental understanding of cluster-cluster interactions gained in this thesis will lead to advances towards molecular cluster-based solar cells.

1.3 References

[1] G. E. Moore, *Electronics Magazine*. **1965**, *38*.

[2] R. P. Feynman, *J. Microelectromech. Syst.* **1992**, *1*, 60-66.

[3] J. Ramsden. *Nanotechnology: An Introduction,* Elsevier Inc, **2011**.

[4] S. A. Campbell. *Fabrication Engineering at the Micro- and Nanoscale*, 3rd Edition, Oxford University Press, **2008**.

[5] H. R. Allcock, *Introduction to Materials Chemistry*, John Wiley & Sons, Inc., **2008**.

[6] Y.-J. Cheng, S.-H. Yang, C.-S. Hsu, *Chem. Rev.* **2009**, *109*, 5868-5923.

[7] A. Mishra, P. Bäuerle, *Angew. Chem. Int. Ed.* **2012**, *51*, 2020-2067.

[8] C. M. Drain, A. Varotto, I. Radivojevic, *Chem. Rev.* **2009**, *109*, 1630-1658.

[9] D. Astruc, E. Boisselier, C. Ornelas, *Chem. Rev.* **2010**, *110*, 1857-1959.

[10] S. A. Claridge, A. W. Castleman, Jr., S. N. Khanna, C. B. Murray, A. Sen, P. S. Weiss, *ACS Nano,* **2009**, *3*, 244-255.

[11] C. B. Murray, C. R. Kagan, M. G. Bawendi, *Annu. Rev. Mater. Sci.* **2000**, *30*, 545-610.

[12] C. A. Hunder, J. K. M. Sanders, *J. Am. Chem. Soc.* **1990**, *112*, 5525-5534.

[13] W. Wu, Y. Liu, D. Zhu, *Chem. Soc. Rev.* **2010**, *39*, 1489-1502.

[14] F. Dötz, J. D. Branch, S. Ito, L. Gherghel, K. Müllen, *J. Am. Chem. Soc.* **2000**, *122*, 7707-7717.

[15] X. Feng, W. Pisula, K. Müllen, *Pure Appl. Chem.* **2009**, *81*, 2203-2224.

[16] L. Chen. Y. Hernandez, X. Feng, K. Müllen, *Angew. Chem. Int. Ed.* **2012**, *51*, 7640-7654.

[17] J. E. Anthony, *Chem. Rev.* **2006**, *106*, 5028-5048.

[18] I. Kaur, M. Jazdzyk, N. N. Stein, P. Prusevich, G. P. Miller, *J. Am. Chem. Soc.* **2010**, *132*, 1261-1263.

[19] S. F. L. Nelson, Y.-Y. Lin, D. J. Gundlach, T. N. Jackson, *Appl. Phys. Lett.* **1998**, *72*, 1854-1856.

[20] J. Takeya, M. Yamagishi, Y. Tominari, R. Hirahara, Y. Nakazawa, *Appl. Phys. Lett.* **2007**, *90*, 1021201-1021203.

[21] S. Xiao, S. J. Kang, Y. Wu, S. Ahn, J. B. Kim, Y.-L. Loo, T. Siegrist, M. L. Steigerwald, H. Li, C. Nuckolls, *Chem. Sci.* **2013**, *4*, 2018-2023.

[22] Y.-F. Lim, Y. Shu, S. R. Parkin, J. E. Anthony, G. G. Malliaras, *J. Mater. Chem.* **2009**, *19*, 3049-3056.

[23] Y. Shu, Y.-F. Lim, Z. Li, B. Purushothaman, R. Hallani, J. E. Kim, S. R. Parkin, G. G. Malliaras, J. E. Anthony. *Chem. Sci,* **2011**, *2*, 363-368.

[24] C.-Y. Chiu, B. Kim, A. A. Gorodetsky, W. Sattler, S. Wei, A. Sattler, M. Steigerwald, C. Nuckolls, *Chem. Sci.* **2011**, *2*, 1480-1486.

[25] R. Martin, S. L. Buchwald, *Acc. Chem. Res.,* **2008**, *41*, 1461-1473.

[26] H. A. Wegner, L. T. Scott, A. Meijere, *J. Org. Chem.* **2003**, *68*, 883-887.

[27] L. Liu, B. Yang, T. J. Katz, M. K. Poindexter, *J. Org. Chem.* **1991**, *56*, 3769-3775.

[28] R. Scholl, C. Seer, *Justus Liebigs Annalen der Chemie.* **1912**, *394*, 111-177.

[29] Z. Bao, *Adv. Mater.* **2000**, *12*, 227-230.

[30] H. W. Kroto, J. R. Health, S. C. O'Brien, R. F. Curl, R. E. Smalley, *Nature*, **1985**, *318*, 162-163.

[31] J. C. Hummelen, B. W. Knight, F. LePeq, F. Wudl, *J. Org. Chem.* **1995**, *60*, 532-538.

[32] M. S. Dresselhaus, G. Dresselhaus, *Annu. Rev. Mater. Sci.* **1995**, *25*, 487-523.

[33] C. A. Reed, R. D. Bolskar, *Chem. Rev.* **2000**, *100*, 1075-1120.

[34] V. Coropceanu, J. Cornil, D. A. da Silva Filho, Y. Olivier, R. Silbey, J.-L. Brédas, *Chem. Rev.* **2007**, *107*, 926-952.

[35] J. Ferraris, D. O. Cowan, V. Walatka, Jr., J. H. Peristein, *J. Am. Chem. Soc.* **1973**, *95*, 948-949.

[36] D. D. Eley, H. Inokuchi, M. R. Willis, *Discuss. Faraday Soc.* **1959**, *28*, 54-63.

[37] D. V. Konarev, R. N. Lyubovskaya, *Russ. Chem. Rev.* **1999**, *68*, 19-38.

[38] P. W. Stephens, D. Cox, J. W. Lauher, L. Mihaly, J. B. Wiley, P.-M. Allemand, A. Hirsch, K. Holczer, Q. Li, J. D. Thompson, F. Wudl, *Nature*. **1992**, *255*, 331-332.

[39] T. Kawase, H. Kurata, *Chem. Rev.* **2006**, *106*, 5250-5273.

[40] S. C. Lee, R. H. Holm, *Angew. Chem. Int. Ed.* **1990**, *29*, 840-856.

[41] T. Saito, *Adv. Inorg. Chem.* **1997**, *44*, 45-91.

[42] C. B. Murray, C. R. Kagan, M. G. Bawendi, *Annu. Rev. Mater. Sci.* **2000**, *30*, 545-610.

[43] R. G. Chaudhuri, S. Paria, *Chem. Rev.* **2012**, *112*, 2373-2433.

[44] A. J. Nozik, M. C. Beard, J. M. Luther, M. Law, R. J. Ellingson, J. C. Johnson, *Chem. Rev.* **2010**, *110*, 6873-6890.

[45] M. W. Degroot, J. F. Corrigan, *Compr. Coord. Chem. II.* **2004**, *7*, 57-123.

[46] J. Darkwa, J. R. Lockemeyer, P. D. W. Boyd, T. B. Rauchfuss, A. L. Rheingold, *J. Am. Chem. Soc.* **1988**, *10*, 141-149.

[47] L. F. Nelson, F. Y.-K. Lo, A. D. Rae, L. F. Dahl, *J. Organomet. Chem.* **1982**, *255*, 309.

[48] L. Deng, E. Bill, K. Wieghardt, R. H. Holm, *J. Am. Chem. Soc.* **2009**, *131*, 11213-11221.

[49] M. Hidai, S. Kuwata, Y. Mizobe, *Acc. Chem. Res.* **2000**, *33*, 46-52.

[50] S. M. Stuczynski, Y.-U. Kwon, M. L. Steigerwald, *J. Organomet. Chem.* **1993**, *449*, 167-172.

[51] D. Fenske, J.-C. Steck, *Angew. Chem. Int. Ed.* **1993**, *32*, 238-242.

[52] S. Dehnen, A. Schafer, D. Fensek, R. Ahlrichs, *Angew. Chem. Int. Ed.* **1994**, *33*, 746-749.

[53] J. F. Corrigan, O. Fuhr, D. Fenske, *Adv. Mater.* **2009**, *21*, 1867-1871.

[54] H. Krautscheid, D. Fenske, G. Baum, M. Semmelmann, *Angew. Chem. Int. Ed.* **1993**, *32*, 1303-1305.

[55] M. L. Steigerwald, S. M. Stuczynski, Y.-U. Kwon, D. A. Vennos, J. G. Brennan, *Inorg. Chim. Acta,* **1993**, *212*, 219-224.

[56] M. L. Steigerwald, T. Siegrist, E. M. Gyorgy, B. Hessen, Y.-U. Kwon, S. M. Tanzler, *Inorg. Chem.* **1994**, *33*, 3389-3395.

[57] B. Krebs, D. Voelker, K.-O. Stiller, *Inorg. Chim. Acta*. **1982**, *65*, L101-L102.

[58] D. Coucouvanis, *Acc. Chem. Res.* **1981**, *14*, 201-209.

[59] G. Christou, B. Ridge, H. N. Rydon, *J. Chem. Soc., Dalton Trans.* **1978**, 1423-1425.

[60] S. Jin, F. J. DiSalvo, *Chem. Mater.* **2002**, *14*, 3448-3457.

[61] C. M. Oertel, R. D. Sweeder, S. Patel, C. M. Downie, F. J. DiSalvo, *Inorg Chem.* **2005**, *44*, 2287-2296.

[62] S. Perruchas, S. Flores, B. Jousselme, E. Lobkovsky, H. Abruña, F. J. DiSalvo, *Inorg. Chem.* **2007**, *46*, 8976-8987.

[63] F. Chen, J. Hihath, Z. Huang, X. Li, J. J. Tao, *Annu. Rev. Phys. Chem.* **2007**, *58*, 535-564.

[64] Y. Selzer, D. L. Allara, *Annu. Rev. Phys. Chem.* **2006**, *57*, 593-623.

[65] Y. Xue, M. A. Ratner, *J. Quant. Chem.* **2005**, *102*, 911-924.

[66] R. L. McCreery, *Chem. Mater.* **2004**, *16*, 4477-4496.

[67] A. Nitzan, M. A. Ratner, *Science*, **2003**, *300*, 1384-1389.

[68] C. Joachim, J. K. Gimzewski, A. Aviram, *Nature*, **2000**, *408*, 541-548.

[69] A. Nitzan, *Annu. Rev. Phys. Chem.* **2001**, *52*, 681-750.

[70] S. V. Aradhya, L. Venkataraman, *Nature Nano.* **2013**, *8*, 399-410.

[71] G. Binnig, H. Roher, Ch. Gerber, E. Weibel, *Appl. Phys. Lett.* **1982**, *40*, 178-180.

[72] G. Binnig, H. Roher, Ch. Gerber, E. Weibel, *Phys. Rev. Lett,* **1982**, *49*, 57-61.

[73] c. J. Chen. *Introduction to Scanning Tunneling Microscopy,* 2nd Edition, Oxford University Press, **2008.**

[74] B. Xu, N. J. Tao, *Science*, **2003**, *301*, 1221.

[75] Y. S. Park, A. C. Whalley, M. Kamenetska, M. L. Steigerwald, M. S. Hybertsen, C. Nuckolls, L. Venkataraman, *J. Am. Chem. Soc.* **2007**, *129*, 15768-15769.

[76] F. Chen, X. Li, J. Hihath, Z. Huang, N. Tao, *J. Am. Chem. Soc.* **2006**, *128*, 15874-15881.

[77] W. Hong, D. Z. Manrique, P. Moreno-García, M. Gulcar, A. Mishchenko, C. J. Lambert, M. R. Bryce, T. Wandlowski, *J. Am. Chem. Soc.* **2012**, *134*, 2292-2304.

[78] L. Venkataraman, J. E. Klare, I. W. Tam, C. Nuckolls, M. S. Hybertsten, M. L. Steigerwald, *Nano Lett.* **2006**, *6*, 458-462.

[79] M. Kamenetska, S. Y. Quek, A. C. Whalley, M. L. Steigerwald, H. J. Choi, S. G. Louie, C. Nuckolls, M. S. Hybersten, J. B. Neaton, L. Venkataraman, *J. Am. Chem. Soc.* **2010**, *132*, 6817-6821.

[80] S. V. Aradhya, J. S. Meisner, M. Krikorian, S. Ahn, R. Parameswaran, M. L. Steigerwald, C. Nuckolls, L. Venkataraman, *Nano Lett.* **2012**, *12*, 1643-1647.

[81] J. S. Meisner, S. Ahn, S. V. Aradhya, M. Krikorian, R. Parameswaran, M. L. Steigerwald, L. Venkataraman, C. Nuckolls, *J. Am. Chem. Soc.* **2012**, *134*, 20440-20445.

[82] K. Seo, A. V. Konchenko, J. Lee, G. S. Bang, H. Lee, *J. Am. Chem. Soc.* **2008**, *130*, 2553-2559.

[83] I. P.-C. Liu, M. Bénard, H. Hasanov, I.-W. P. Chen, W.-H. Tseng, M.-D. Fu, M. M. Rohmer, C. Chen, G.-H. Lee, S.-M. Peng, *Chem. Eur. J.* **2007**, *13*, 8667-8677.

[84] H. E. Katz, Z. Bao, S. L. Gilat, *Acc. Chem. Res.* **2011**, *34*, 359-69.

[85] Z. Bao, A. J. Lovinger, A. Dodabalapur, *Appl. Phys. Lett.* **1996**, *69*, 3066-3068.

[86] A. K. K. Kyaw, D. H. Wang, H.-R. Tseng, J. Zhang, G. C. Bazan, **2013**, *102*, 1633081-16330814.

[87] Y. Wen, Y. Liu, Y. Guo, G. Yu, W. Hu, *Chem. Rev.* **2011**, *111*, 3358-3406.

[88] A. R. Murphy, J. M. J. Fréchet, *Chem. Rev.* **2007**, *107*, 1066-1096.

[89] K. Walzer, B. Maennig, M. Pfeiffer, K. Leo, *Chem. Rev.* **2007**, *107*, 1233-1271.

[90] D. Yu, B. L. Wehrenberg, P. Jha, J. Ma, P. Guyot-Sionnest, *J. Appl. Phys.* **2006**, *99*, 1043151-1043157

[91] B. G. Streetman, S. Banerjee, *Solid State Electronic Devices*, 5th Editiion, Prentice Hall International, Inc. **2000**.

[92] D. K. Schroder, *Semiconductor Material and Device Characterization*, 3rd Edition, John Wiley & Sons, Inc. **2006**.

[93] P. Zhang, Y. Y. Lau, R. S. Timsit, *IEEE Trans. On Elect. Dev.* **2012**, *59*, 1936-1940.

[94] B. G. Yacobi, *Semiconductor Materials, An Introduction to Basic Principles.* Kluwer Academic Publishers, **2004**.

[95] R. A. Butera, D. H. Waldeck, *J. Chem. Ed.* **1997**, *74*, 1090-1094.

[96] E. Becquerel, *Comptes Rendus,* **1839**, *9*, 561-567.

[97] A. Einstein, *Ann. der Phys.* **1905**, *17*, 132-148.

[98] D. M. Chapin, C. S. Fuller, G. L. Pearson, *J. Appl. Phys.* **1954**, *25*, 676-677.

[99] D. Trivich, *Ohio J. Sci.* **1953**, *53*, 300-314.

[100] NREL, National Center for Photovoltaics, http://www.nrel.gov/ncpv/, accessed June 30, 2013.

[101] *Our Energy Sources,* National Academy of Sciences, http://needtoknow.nas.edu/energy/energy-sources/, accessed June 30, 2013.

[102] B. A. Gregg, M. C. Hanna, *J. Appl. Phys.* **2003**, *93*, 3605-3614.

[103] J.-L. Brédas, J. E. Norton, J. Cornil, V. Coropceanu, *Acc. Chem. Res.* **2009**,*42*, 1691-1699.

[104] T. Schiros, G. Kladnik, D. Prezzi, A. Ferretti, G. Olivieri, A. Cossaro, L. Floreano, A. Verdini, C. L. Schenck, M. Cox, A. A. Gorodetsky, K. Plunkett, D. Delongchamp, C. Nuckolls, A. Morgante, D. Cvetko, I. Kymissis, *Adv. Energy Mater.* **2013**, Early View DOI: 10.1002/aenm.201201125.

Chapter 2. Tuning the Properties of Contorted Hexabenzocoronene for Organic Photovoltaic Performance

Part of this chapter was reproduced from a paper published in *Chemical Science* by © Royal Society of Chemistry: "Bending Contorted Hexabenocoronene into a Bowl" by Adam C. Whalley, Kyle N. Plunkett, Alon A. Gorodetsky, Christine L. Schenck, Chien-Yang Chiu, Michael L. Steigerwald, and Colin Nuckolls. *Chemical Science* 2011, **2**, 132-135. **DOI:** 10.1039/C0SC00470G.

2.1 Introduction

Organic photovoltaics (OPVs) are being heavily pursued as a virtually inexhaustible source of clean energy to address mankind's ever-increasing energy demands. Hexabenzocoronene (HBC) derivatives have been explored as a family of polycyclic aromatic hydrocarbons (PAHs) with interesting optical, electronic, and structural properties for organic photovoltaics. The HBC structures contain a coronene core with six benzene rings fused on the outer edges of the core. These six additional benzene rings can result from either three-carbon annulated rings (blue, Figure 2.1) or four-carbon annulated rings

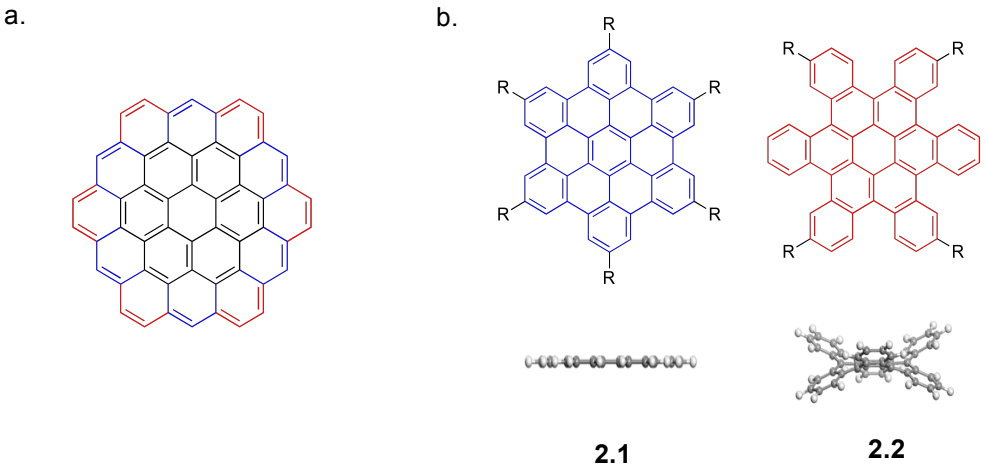

Figure 2.1. Hexabenzocoronene structures. a) Schematic of the various substitution patterns of fused benzene rings around a coronene core. Blue phenyl rings represent the outer ring placement that results in flat HBC **2.1**. Red phenyl rings represent outer ring placement that results in contorted HBC **2.2**. b) Structures of the two hexabenzocoronene derivatives, flat HBC **2.1** and contorted HBC **2.2**, where R = H or solubilizing alkyl chains.

(red, Figure 2.1) around the outer edge of coronene. The former placement results in hexa-*peri*-hexabenzocoronene (flat HBC **2.1**, Figure 2.1b), a completely planar structure, while the latter results in hexa-*cata*-hexabenzocoronene (contorted HBC **2.2**, Figure 2.1b), which is a contorted structure due to the steric interaction between the hydrogens in the bay positions.[1,2] Despite the markedly different three-dimensional structure of these HBC relatives, these molecules share very similar electronic and optical properties. Both are p-type semiconductors with a maximum UV-visible (UV-vis) absorption near 380 nm and a HOMO-LUMO gap of approximately 2.7 eV.[1,3]

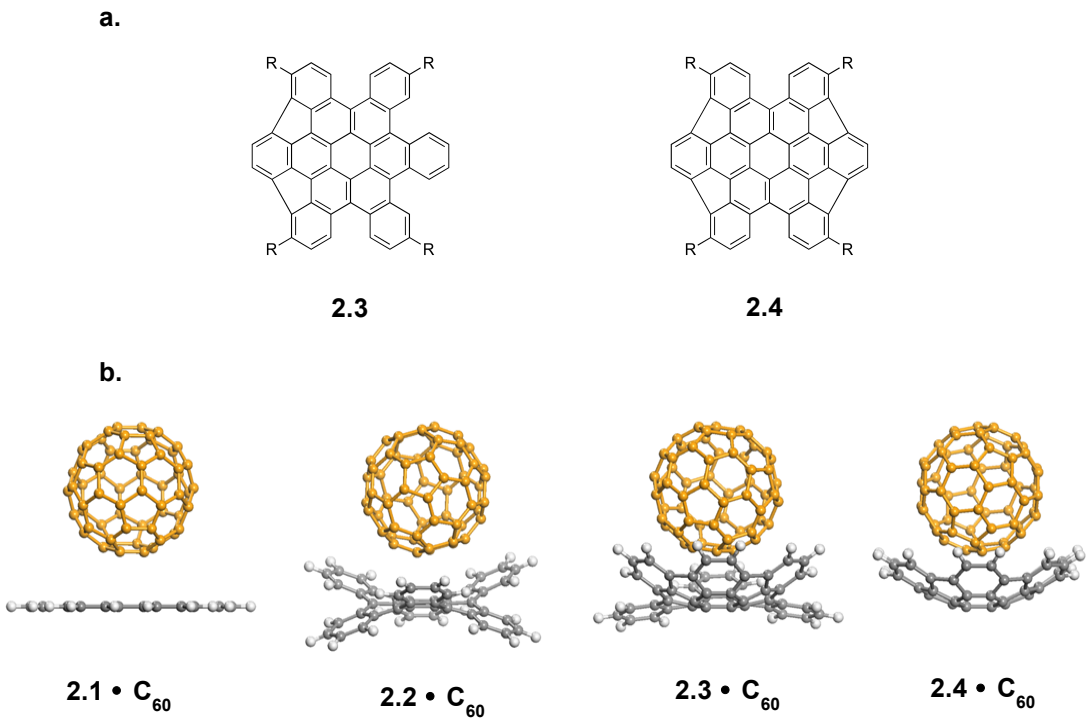

Figure 2.2. Hexabenzocoronene derivatives of increasing contortion. a) Structures of 2-closed contorted HBC **2.3** and 4-closed contorted HBC **2.4** where R = $OC_{12}H_{25}$. b) Cartoon of the interaction between **2.1** - **2.4** and C_{60} fullerene. This cartoon is not meant to imply that the solution complex is 1:1.

When investigated in a solar cell, the shape-complementarity between HBC derivatives and the chosen acceptor molecule was shown to be vital to device efficiency. An OPV device was made with flat-HBC **2.1** as the donor material and N,N'-bis(1-ethylpropyl)-3,4,9,10-perylenebis (dicarboximide) (perylene) as the acceptor material to give a power conversion efficiency (PCE)

of 1.95% (490 nm illumination).[4] However, when **2.1** is used as a donor material with C_{60} fullerene, the PCE was dramatically lower (0.03% at 422 nm illumination).[3] When contorted HBC **2.2** was used as a donor material with C_{60} fullerene, the PCE was 3.36% (422 nm illumination).[3] These studies demonstrate that **2.1** interacts more favorably within an OPV device with a flat acceptor molecule (perylene diimide) while **2.2** may interact more favorably with a curved acceptor molecule (C_{60} fullerene). In addition, **2.2** and C_{60} fullerene form co-crystals under a number of growth conditions in which the concave faces of contorted HBC contain a fullerene molecule, much like a ball-and-socket.[3]

There are several examples of the unique guest-host interaction involving concave-convex π-π faces of curved PAHs and fullerenes.[5-9] Association of the guest and host are generally studied through fluorescence and NMR spectroscopy to give association constants as high as 10^5.[9] Bowl-shaped HBC derivatives **2.3** and **2.4** were synthesized in order to gain a deeper understanding of how the donor-acceptor electronic interactions are impacted by shape-complementarity (Figure 2.2). Section 2.2 describes the interaction of contorted HBC derivatives **2.2** – **2.4** with fullerenes in solution through fluorescence quenching and NMR spectroscopy titration experiments.

Another important consideration for improving efficiency of contorted HBC OPV devices is the range of UV-vis absorption of the device. Most HBC derivatives absorb primarily UV light, with absorption extending out to near 450 nm (Figure 2.3a).[2,10,11] In contrast, the solar spectrum emits primarily in the lower energy visible and infrared regions (Figure 2.3a). The consequence of this poor overlap with the solar spectrum is that the PCE of the contorted HBC **2.2** and C_{60} fullerene OPV increases significantly when illumination is changed from a solar simulator to a light source at 422 nm.[3] The contorted octabenzocircumbiphenyl **2.5** has been recently synthesized and explored as a much larger HBC derivative with red-shifted absorption (Figure 2.3b).[12] This structure, which contains eight aromatic rings fused to a circumbiphenyl core, extends absorption out to approximately 500 nm.[12] However, further extension of contorted HBC in this fashion is limited by solubility, which presumably gets worse as the π-face of the contorted HBC grows

larger. In addition, size-matching between donor and acceptor molecules is known to be an important aspect of their interaction, so extension of contorted HBC may inhibit the donor-

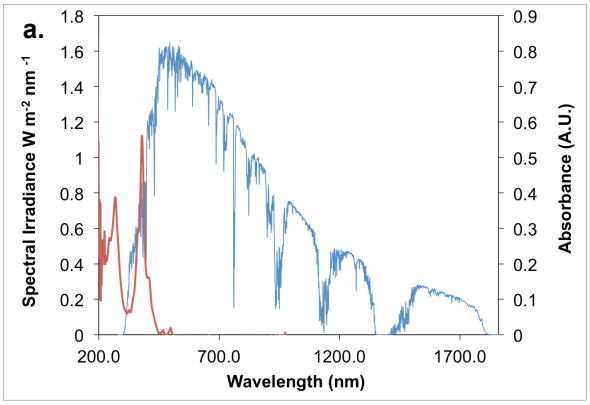

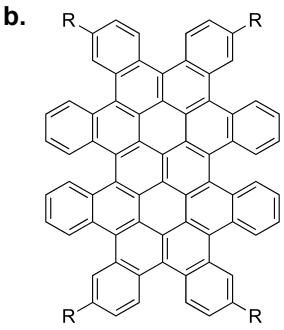

2.5

Figure 2.3. Addressing the poor overlap between HBC light absorption and the solar spectrum. a) UV-vis spectrum of **2.2** overlaid with the spectral irradiance of the sun (obtained from NREL at http://rredc.nrel.gov/solar/spectra/am1.5/) b) Structure of octabenzocircumbiphenyl **2.5**, where R = $OC_{12}H_{25}$.

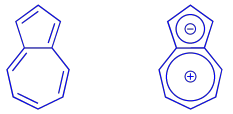

2.6

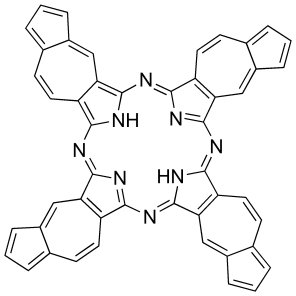

2.7

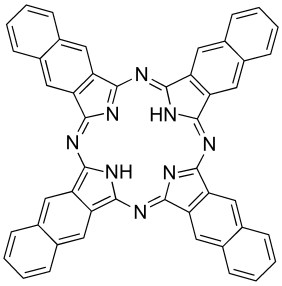

2.8

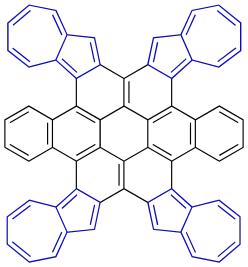

2.9

Figure 2.4. Azulene and azulene PAHs. From left to right: Structure of azulene (**2.6**) represented as a fused aromatic structure as well as a fused tropylium cation and cyclopentadiene anion, structure of azulenocyanine (**2.7**), structure of napthalocyanine (**2.8**), and structure of target molecule azulene HBC (**2.9**). Azulene segments of **2.9** are highlighted in blue.

acceptor interaction due to a size mismatch.[13] An alternate method for expanding the UV-vis absorption is to tune the electronics of contorted HBC by functionalization of the outer aromatic rings. This strategy is potentially very powerful, as it would allow for continued shape- and size-matching between HBC and fullerene due to the preservation of the effective three-dimensional structure of **2.1**.

Azulene (**2.6**) is a nonalternate PAH that has a large dipole moment and is most notably a royal blue color.[14] It is often represented as a fused tropylium cation and cyclopentadiene anion (Figure 2.4).[14] Incorporation of azulene into PAHs has been shown to have a dramatic impact on the electronics of the system.[15-18] A notable example of this is azulenocyanine **2.7**.[18] While **2.7** is a structural isomer of naphthalocyanine **2.8**, it has a lowest-energy absorption band that is red-shifted by more than 300 nm and a significantly lower LUMO energy level due to the azulene subunit. Additionally, the azulene moiety provides a means for further tuning of the electronics by protonation of the electron rich five-membered ring to yield a stable tropylium cation. The effects of this reversible process on the optoelecronics of the system include a dramatic color change and a lowering of the band gap.[18-20] Although the azulene unit induces interesting properties within larger structures, there are relatively few examples of azulene PAHs in the literature. Section 2.3 describes efforts towards the synthesis and study of an azulene HBC derivative.

2.2 Interaction of Fullerenes and Shape-Matched Contorted Hexabenzocoronenes

In this section, the interaction between contorted HBC derivatives **2.2** - **2.4**, which have increasing degrees of curvature, and fullerenes will be explored. Fluorescence quenching experiments with fullerenes C_{70}, C_{60}, and phenyl-C61-butyric acid methyl ester (PCBM) demonstrated a strong association to only the more severely bowl-shaped HBC derivatives. NMR titration experiments confirmed this strong association. Both experiments suggested that a 2:1 complex of **2.4** and C_{70} in solution and a 1:1 complex between **2.4** and C_{60} or PCBM.

2.2.1 Results and Discussion

The synthesis of **2.2** – **2.4** was accomplished using previously developed synthetic routes.[21-23] Structures **2.2** – **2.4** were derived from pentacenequinone HBC precursors **2.10a** - **c** (Scheme 2.1). Formation of **2.2** – **2.4** was determined by the number of halogens installed on this pentacenequinone HBC precursor (zero, two, and four, respectively), which determines how many five-membered rings are formed in the final step. The pentacenequinone HBC precursors **2.10a** - **c** were transformed into the corresponding bisolefin intermediates through a Ramirez-

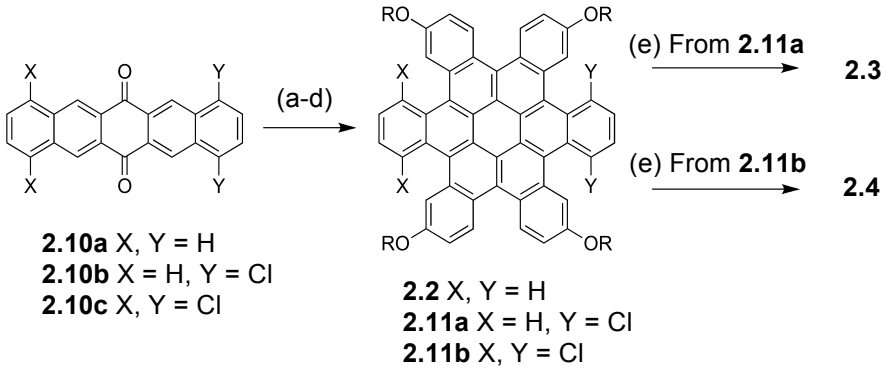

Scheme 2.1. Synthesis of HBC derivatives **2.2** - **2.4**. Key: (a) CBr_4, PPh_3, toluene, 80°C, 16 h. (b) $[Pd(PPh_3)_4]$, 2-(4-(dodecyloxy)phenyl)-4,4,5,5-tetramethyl-1,3,2-dioxaborolane, THF, 2 M K_2CO_3 (aq), 100°C, 16 h. (c) hν, I_2, propylene oxide, benzene, rt, 3h. (d) $FeCl_3$, CH_3NO_2, CH_2Cl_2, rt, 3 h. (e) $[Pd(PCy_3)_2Cl_2]$, DBU, DMA, μwave, 150°C, 3 h. In all cases, R = $C_{12}H_{25}$.

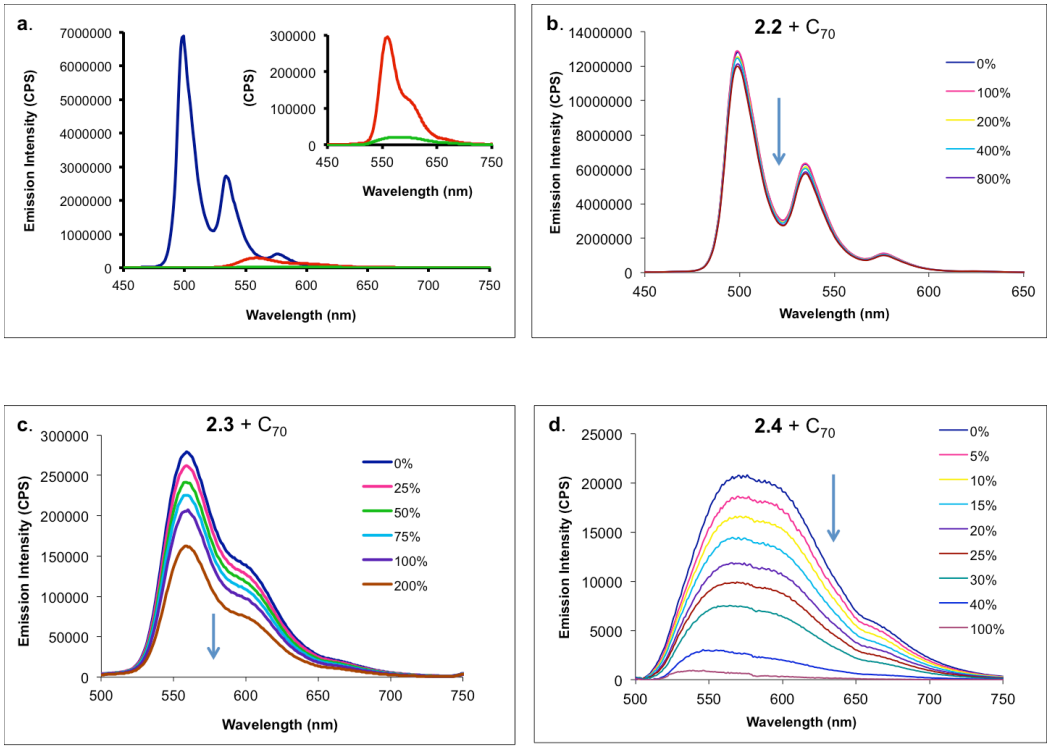

$K_a = 4.7 \times 10^5$ $K_a = 3.2 \times 10^6$

Figure 2.5. Fluorescence quenching experiment for **2.2** - **2.4** with fullerenes and calculated association constants. a) Fluorescence emission spectra of **2.2** - **2.4** in CH_2Cl_2 (Concentration = 1.00 x 10^{-6} M). Inset shows the zoomed in region of **2.3** (red) and **2.4** (green). Blue curve represents **2.2**. b) Fluorescence emission spectra of **2.2** with addition of 0%-800% C_{70} excited at 392 nm (1.0 x 10^{-7} M in CH_2Cl_2). c) Fluorescence emission spectra of **2.3** with addition of 0-200% C_{70} excited at 392 nm (1.0 x 10^{-6} M in CH_2Cl_2). d) Fluorescence emission spectra of **2.4** with addition of 0-100% C_{70} excited at 392 nm (1.0 x 10^{-6} M in CH_2Cl_2). Note: For all spectra, blue arrows indicate decrease in fluorescence upon quenching.

Corey-Fuchs reaction, followed by coupling of four 2-(4-(dodecyloxy)phenyl)-4,4,5,5-tetramethyl-1,3,2-dioxaborolanes using Suzuki cross-coupling. With the carbon framework in place, a sequence of photocyclization and subsequent oxidative ring closure gave the HBC core **2.2** and **2.11a** - **b**. To complete the synthesis of **2.3** and **2.4**, a final microwave-assisted Heck coupling with $[Pd(PCy_3)_2Cl_2]$ as the catalyst and 1,8-diazabicycloundec-7-ene (DBU) as the base was required to form the five-membered rings around the periphery.[24-26]

The fluorescence emission spectra of compounds **2.2** – **2.4** showed a dramatic reduction in light emission as well as a general red-shift when the number of five-membered rings increased (Figure 2.5a). While **2.2** was highly fluorescent with a quantum yield of 0.14 (CH_2Cl_2), the quantum yields of **2.3** and **2.4** were 0.034 and 0.0085 (CH_2Cl_2), respectively. The apparent fluorescence dampening is reminiscent of fullerenes, which have quantum yields on the order of 1 x 10^{-4}, as well as other cyclopenta-fused polycyclic aromatic hydrocarbons (CP-PAHs) that display no detectable fluorescence.[27]

Several fluorescence quenching experiments were performed to determine binding of different fullerenes to **2.2** – **2.4** in solution. No measurable decrease in emission intensity was found for C_{70} and **2.2** at equimolar concentrations in CH_2Cl_2 (Figure 2.5b) suggesting that the association between **2.2** and C_{70} was minimal in solution. HBC **2.3** emission was quenched by about 50% when it was mixed with equimolar amounts of C_{70} (Figure 2.5c). HBC **2.4** shows completely quenched fluorescence when ~0.5 equivalents of C_{70} is added (Fig. 2.6a). The complete quenching of **2.4** with only 50% C_{70} may suggest that a 2:1 complex was formed in solution. Using a simple Stern–Volmer analysis, association constants were calculated to be 4.7 x 10^5 M^{-1} for **2.3** and C_{70} and 3.2 x 10^6 M^{-1} for **2.4** and C_{70}.[28] These values are among the highest reported for concave-convex π-π host-guest complexes.[5-9]

Fluorescence quenching experiments were also performed with C_{60} and PCBM as quenchers (See Figures A.1-A.8). Similar to the case of C_{70}, almost no fluorescence quenching was observed with **2.2**, while **2.3** and **2.4** showed significant quenching. Fluorescence of **2.4** was most significantly quenched in all cases, and a summary of the fluorescence emission intensity of **2.4** versus equivalents of fullerene is shown in Figure 2.6a - c. While fluorescence is almost

completely quenched with ~0.5 equivalents of C_{70}, fluorescence is only quenched completely after one equivalent of C_{60} is added. This result may imply that while a 2:1 complex is formed

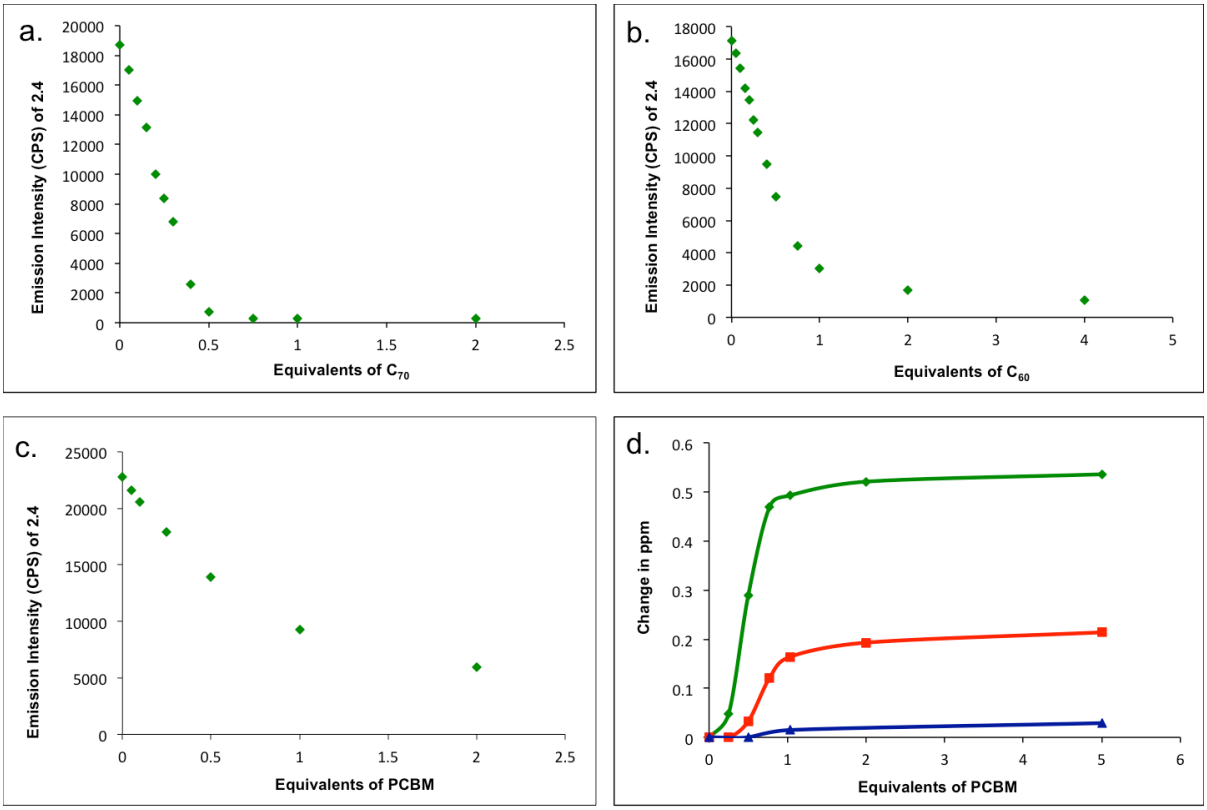

Figure 2.6. Fluorescence quenching and NMR titration experiments for **2.2** - **2.4** with fullerenes. a) Fluorescence emission intensity of **2.4** versus C_{70} equivalents (excited at 600 nm, 1.0 x 10^{-6} M in CH_2Cl_2). b) Fluorescence emission intensity of **2.4** versus C_{60} equivalents (excited at 600 nm, 1.0 x 10^{-6} M in CH_2Cl_2). c) Fluorescence emission intensity of **2.4** versus PCBM-C_{60} equivalents (excited at 600 nm, 1.0 x 10^{-6} M in CH_2Cl_2). d) Change in ppm of protons H_h (**2.2**), H_c (**2.3**, **2.4**) versus equivalents of PCBM. See Figure 2.7 for proton assignments.

between **2.4** and C_{70}, respectively, there is a 1:1 complex formed between **2.4** and C_{60}. This distinction may be accounted for by the capsule shape of the C_{70} fullerene, which provides more surface area for π-π interactions on both ends of the capsule. The spherical shape of C_{60} may not be large enough to accommodate two molecules of **2.4** simultaneously. By this logic, $PC_{60}BM$ should only be able to interact with one molecule of HBC at a time because of the steric bulk of the phenyl butyric acid methyl ester group. The plot of emission intensity versus PCBM-C_{60} shows a steady decrease in fluorescence intensity beyond 0.5 equivalents of PCBM and a tapering off of fluorescence quenching after one equivalent of PCBM.

NMR titration experiments were performed to monitor shifts in ^{1}H NMR peaks of **2.2** - **2.4** with addition of PCBM (Figure 2.6d, A.9-A.17). The most dramatic change in proton shifts were observed with **2.4**, while very little change was observed for **2.2**. This correlates well with the results from the fluorescence quenching experiment. The change in proton shifts for **2.2** - **2.4** occurred between the addition of zero and one equivalents of PCBM. Beyond one equivalent of PCBM, the proton shifts remained constant. This suggests that a 1:1 complex is being formed between HBC derivative and PCBM.

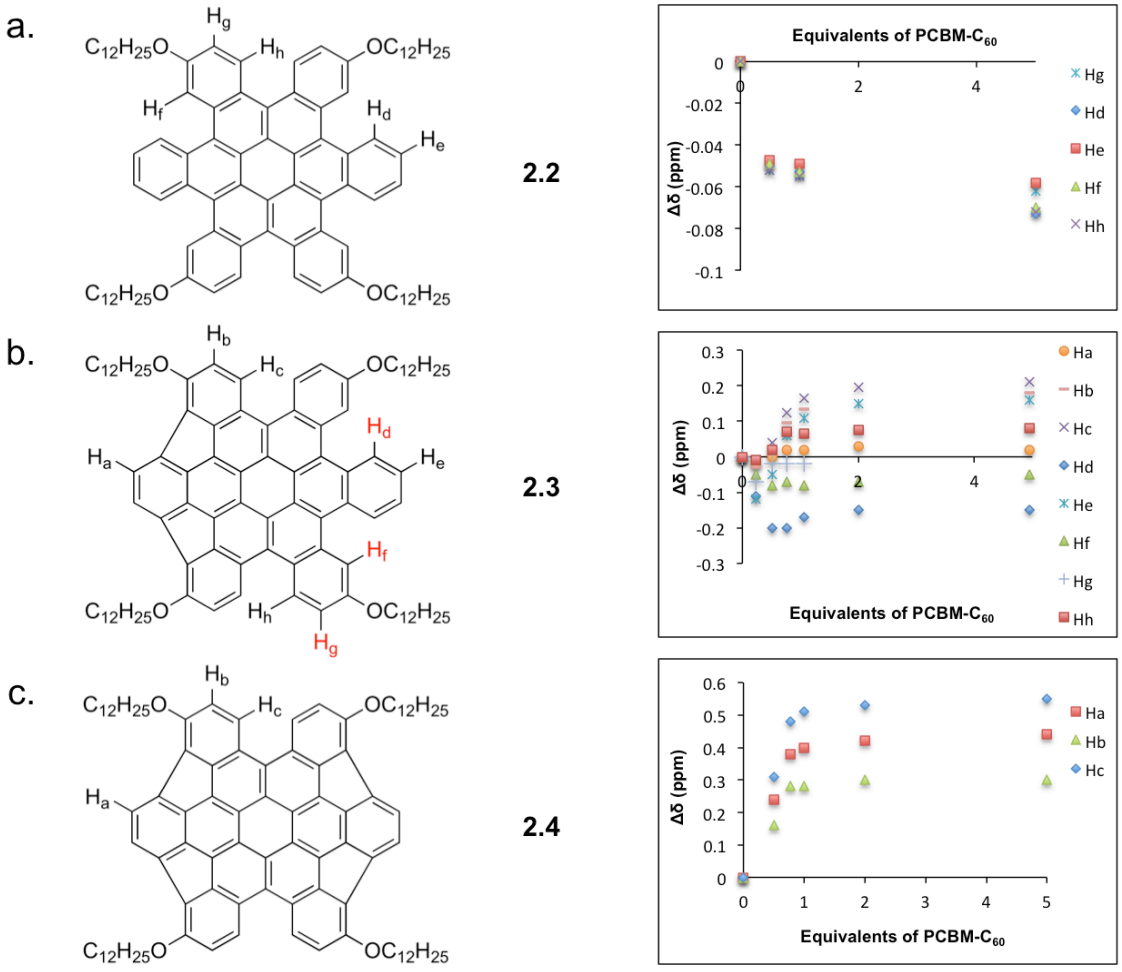

Figure 2.7. NMR titration experiments for **2.2** - **2.4** with fullerenes. a) Δδ (ppm) of **2.2** versus equivalents of PCBM (right). Corresponding protons are shown on the structure (left). b) Δδ (ppm) of **2.3** versus equivalents of PCBM (right). Corresponding protons are shown on the structure, with red protons indicating those that are shielded (left). c) Δδ (ppm) of **2.4** versus equivalents of PCBM (right). Corresponding protons are shown on the structure (left).

A summary of the proton shifts for all proton signals in structures **2.2** - **2.4** upon incremental addition of PCBM are shown in Figure 2.7. Protons of **2.2** were slightly shielded when introduced to PCBM, indicating a very weak association of the complex. Protons of **2.4** were shifted a full order of magnitude more than those of **2.2** upon addition of PCBM, with all protons shifting downfield. The large change in proton shift indicates that a complex is being formed with stronger association. The fact that these protons were being deshielded suggests that the strongest binding is occurring at the coronene center of the structure rather than on the outer rings, as protons directly attached to the binding site are generally shielded while those farther away are deshielded.[7,8] HBC **2.3** demonstrated an extremely interesting phenomenon. Initially, all protons show minor shielding effects, indicated by an upfield shift. However, as more equivalents of PCBM were added, protons H_d, H_f, and H_g were the only protons whose shifts remained upfield. All other protons reversed their shift, and moved downfield from their original position. The downfield shift of protons H_a, H_b, and H_c directly mimic the shifts of **2.4**, indicating that binding is occurring away from these protons and more towards the center of the molecule. Protons H_d, H_f, and H_g are located on the half of the molecule that remains similar in structure to that of HBC **2.2**, with a minimum energy conformation calculated to be down-up-down relative to the bowl on the other half of the molecule (Figure 2.2b). The fact that these protons shift upfield implies not only that PCBM is binding directly to the these outer rings, but also suggests that these flexible three "arms" flip up to form a bowl structure similar to that of **2.4**. As these arms flip, it would be expected that they would also twist somewhat due to steric congestion from proximal carbons. This may explain why H_h and H_e show an upfield shift (far from binding) while H_g, H_f, and H_d show downfield shifts (direct participation in binding).

2.2.2 Experimental

2.2.2.1 General Information

Synthesis of **2.2** – **2.4** was performed according to reported procedures.[22] ^{1}H NMR (400 MHz) and ^{13}C NMR (100 MHz) spectra were recorded on Bruker DRX-300 and Bruker DRX-400 spectrometers at room temperature unless otherwise noted. Fluorescence spectroscopy was

performed with a Jobin Yvon Fluorolog-3 Spectrofluorometer (Model FL-TAU3). C_{60} and C_{70} fullerene were purchased from BuckyUSA. PCBM-C_{60} was purchased from Nano-c. Solvents were purchased from Aldrich and used as received. NMR solvents were purchased from Cambridge Isotope Laboratories and used as received.

2.2.2.2 Fluorescence Quenching and Quantum Yield Determination Experimental Details

To perform this experiment, stock solutions of **2.2** - **2.4** and C_{60}, C_{70}, and PCBM were made in CH_2Cl_2. The concentration of HBC derivatives (**2.2** - **2.4**) was constant for all measured solutions within a quenching experiment and the amount of fullerene used in that experiment (C_{60}, C_{70}, or PCBM) was varied. Each solution being measured was brought up to a constant volume of 3 mL. Association constants were calculated using Stern-Volmer techniques.[28] Quantum yields were determined at an excitation of 425 nm with 9,10-bis(phenylethynyl)anthracene as a standard. Quantum yields were calculated using standard methods.[29]

2.2.2.3 NMR Titration Experimental Details

NMR titration experiments were run on a single sample of **2.2** - **2.4**, where the amount of PCBM was increased incrementally and NMR spectra were obtained after each addition of PCBM. The amount of solvent was kept constant throughout the experiment. All spectra were referenced to CD_2Cl_2.

2.2.3 Conclusions

The solution association of fullerene and contorted HBC is increased as bowl-shaped character is increased. Using fluorescence quenching and NMR titration spectroscopy, it was observed that **2.2** shows almost no association with C_{70} fullerene in solution while **2.3** and **2.4** have some of the highest association constants observed in ball-and-socket systems. Experiments indicate that a 2:1 complex of **2.4** and C_{70} are being formed in solution, while a 1:1 complex is being formed between **2.4** and C_{60} or PCBM-C_{60}. These results suggest that shape-

matching donor materials, such as contorted HBCs, to fullerenes results in strong electronic interactions.

2.3 Towards the Synthesis and Study of Azulene Hexabenzocoronene

In this section, progress towards the synthesis of azulene HBC **2.9** will be described. A preliminary study of the properties of azulene HBC will be presented. Calculated structures of the azulene HBC and the precursor bisolefin will be discussed. Finally, the bisolefin intermediate is explored as an azulene PAH with electronic tunability through acid exposure.

2.3.1 Results and Discussion

The synthetic route to **2.9** was inspired by previous syntheses of contorted HBC derivatives (Scheme 2.2).[21] Azulene is readily borylated at the 2-position via iridium-catalyzed C-H activation to give intermediate **2.12**.[30] Suzuki cross-coupling of four units of **2.12** to tetrabromo pentacenequinone **2.13** gave the forest green bisolefin product **2.14** in 64% yield. Upon photocyclization of **2.14**, a dark red solid was obtained. The ^{1}H NMR spectrum in d_8-THF showed a highly unsymmetrical product with many overlapping peaks and was therefore inconclusive as to the structure of the product. However, the NMR did not indicate any starting material. The highly asymmetric nature of the NMR and the appearance of peaks dramatically downfield from the original bisoelfin **2.14** suggested a partially cyclized product. To fully cyclize the product, the intermediate was subjected to Scholl conditions without any purification of the intermediate to give a black-red solid in high yield. This final material is insoluble in many common solvents and is only sparingly soluble in THF. Its ^{1}H NMR spectrum in d_8-THF was obtained, but poor resolution due to the poor solubility did not allow for full structure determination. The decrease in the number of peaks in the spectrum indicated a much more symmetric structure, and further downfield shifting of the aromatic protons suggested a further cyclized product.

A UV-vis spectrum of **2.14**, **2.9**, and the partially cyclized intermediate was obtained (Figure 2.9a). As expected, the UV-vis spectrum shows that absorption was red-shifted as the structure increased in cyclization and therefore in conjugation. The lowest energy absorption of

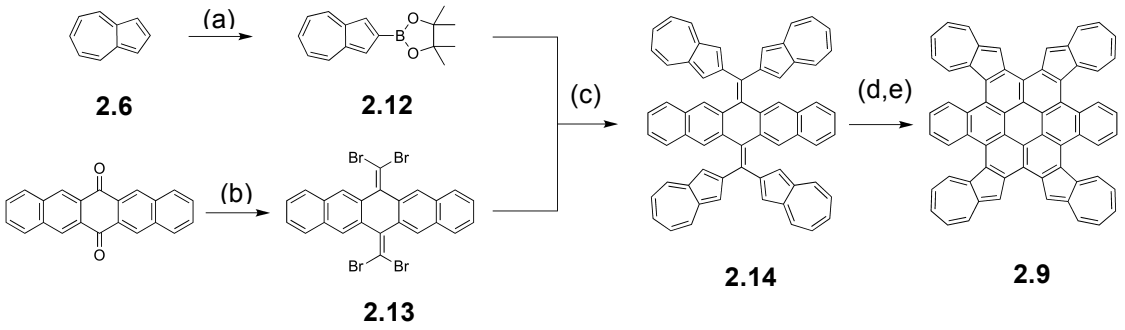

Scheme 2.2. Synthesis of azulene HBC **2.9**. Key: (a) $[IrCl(COD)]_2$, 4,4'-di-*tert*-butyl-2,2'-dipyridyl, bis (pinacolato)diboron, cyclohexane, 97°C, 14 h, 34%. (b) CBr_4, PPh_3, pentacene-6,13-dione, toluene, 80°C, 20 h, 75%. (c) $Pd(Cl)_2(PPh_3)_2$, K_2CO_3, THF, H_2O, 70°C, 24 h, 64%. (d) h*v*, I_2, propylene oxide, benzene, 3h. (e) $FeCl_3$, CH_3NO_2, CH_2Cl_2, rt, 30 min, 95% (impure).

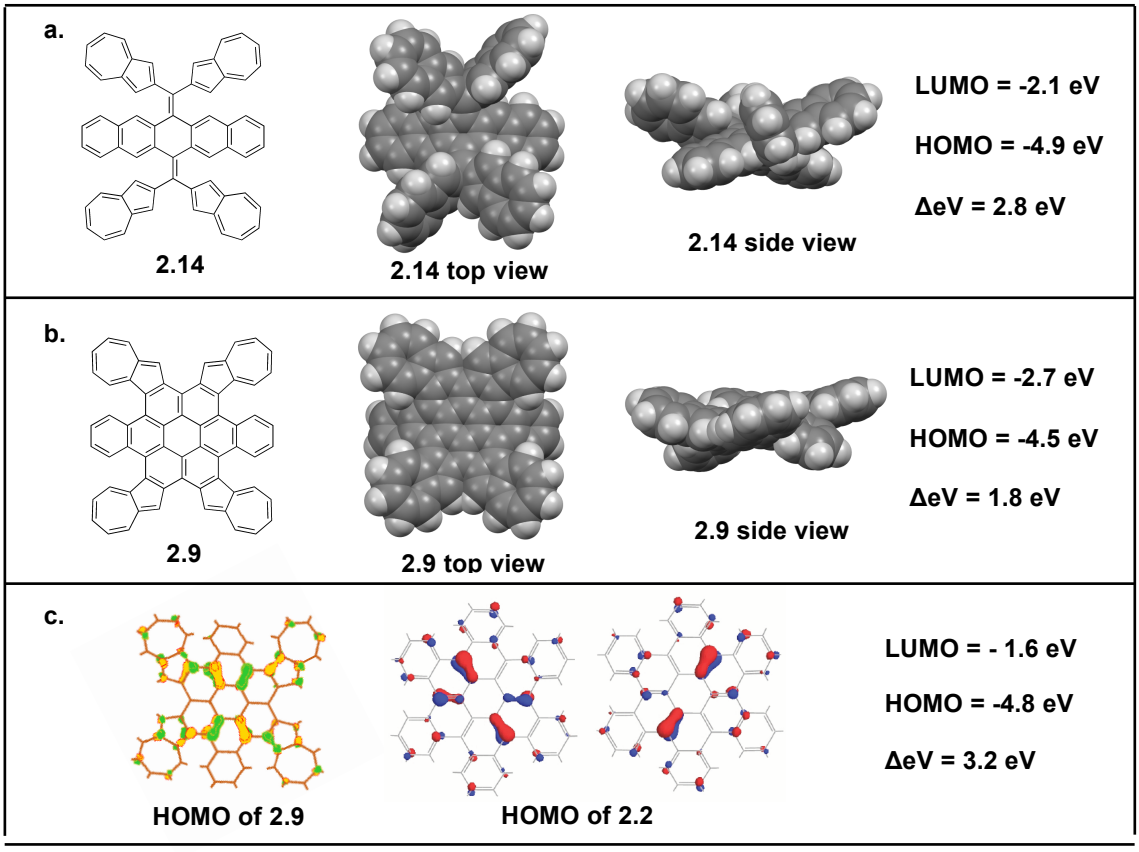

Figure 2.8. DFT Calculations for **2.14** and **2.9**. a) Top and side view of calculated structure of **2.14**. and calculated HOMO, LUMO, and band gap. b) Top and side view of calculated structure of **2.9** and calculated HOMO, LUMO, and band gap. c) Comparison of the frontier orbitals for **2.9** (left) and **2.2** (right). The calculated HOMO, LUMO, and band gap of **2.2** is shown on the right.

2.9 was red-shifted nearly 100 nm relative to **2.2**. This indicates that the electronics of the HBC core are significantly impacted by the incorporation of azulene subunits.

Calculations confirm that incorporation of azulene into the HBC core changes the electronics of HBC dramatically while maintaining a contorted structure. Contorted HBC structures typically adopt either an “up-down-up” or “butterfly” conformation, with the electronically favored structure of **2.2** being the up-down-up conformation.[2] However, in the case of **2.9**, the butterfly conformation is favored by approximately 7 kcal/mol (Figure 2.8b). The HOMO of **2.9** is also calculated to be significantly higher in energy than that of **2.2** (Figure 2.8b,c).[31] Similar to the HOMO of **2.2**, the HOMO of **2.9** has significant radialene character around the coronene core (Figure 2.8c).[31] However, while the pendant phenyl rings in **2.2** have little involvement in the HOMO, the electron density extends onto the cyclopentadiene rings in **2.9** (Figure 2.8c).[31] Finally, excited state calculations predict low energy absorptions out to near 750 nm. This is in good agreement with the observed UV-vis spectrum, which shows low absorption beyond 750 nm.

We became interested in **2.14** because, while the comparable tetraphenyl bisolefin intermediate in the synthesis of **2.2** is white, **2.14** exhibited a forest green color, suggesting that incorporation of azulene has a significant impact on the bisolefin electronics.[21] The calculated structure of **2.14** shows the pentacene is bent at the olefin attachment, and the azulene subunits are twisted to minimize steric interactions. Surprisingly, the HOMO level of **2.14** is the same energy as the HOMO of **2.2** and the LUMO of **2.14** is lower than that of **2.2**. This results in a lower band gap for **2.14** than **2.2**. This is supported by the UV-vis spectrum of **2.14**, which shows two strong transitions with λ_{max} at 288 nm and 422 nm (Figure 2.9a). Absorption of bisolefin **2.14** continues to almost 500 nm, which is a slightly larger window of absorption compared with **2.2**.

It is well known that azulenes can be protonated at the electron-rich five-membered ring, forming an aromatic cation in the seven-membered ring.[17,19,20] The formation of this relatively stable tropylium cation significantly alters the electronics of the system, allowing for tuning of the band gap that can be observed by UV-vis spectroscopy.[17,19,20] Treatment of **2.14** in chloroform with incremental addition of trifluoroacetic acid (TFA) led to a dramatic color change of the

solution from dark green to black-red (Figure 2.9b). While the transitions at λ_{max} 288 nm and 422 nm remained strong, two new peaks grew in at much longer wavelengths with addition of TFA.

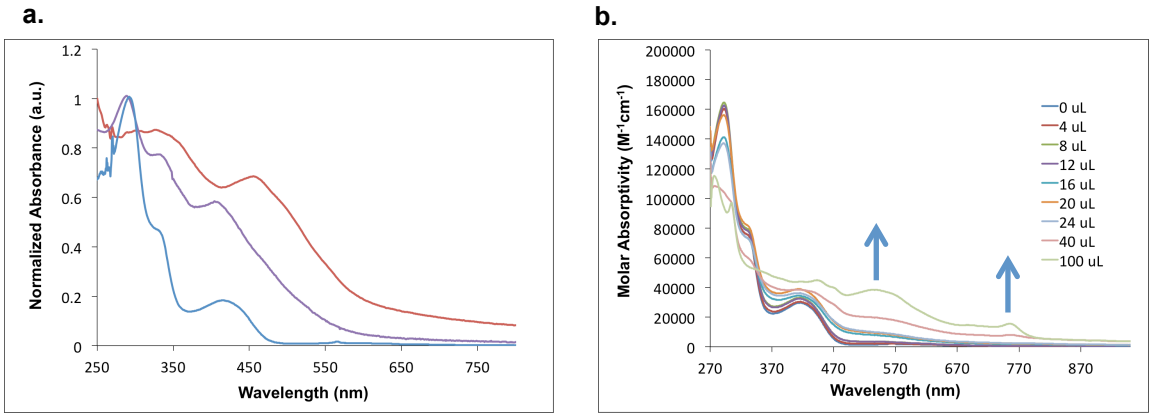

Figure 2.9. UV-vis spectroscopy. Key: a) Normalized UV-vis spectra of **2.14** (blue), the photocyclization product of **2.14** (purple), and impure **2.9** (red) in THF. b) UV-vis spectroscopy titration experiment in chloroform. Concentration of **2.14** remained constant at 4.2 x 10^{-6} M and TFA was added in volumes from 0 µL – 100 µL. Blue arrows depict growth of two new peaks with addition of a large excess of TFA.

These new peaks at λ_{max} 535 nm and 751 nm account for a large red shift in the absorption ($\Delta\lambda_{max}$ of ~300nm) and indicate a much smaller band gap material. While small molecules that have only one azulene unit incorporated generally display a red-shift of approximately 100 nm, polyazulene has been shown to red-shift nearly 300 nm.[17,19,20] The fact that **2.14** demonstrates a shift similar to that of polyazulene suggests that more than one of the four azulene units on **2.14** is being protonated, resulting in a system with more than one tropylium cation. This dramatic change in optoelectronic properties makes this system interesting as a potential sensor, and certainly indicates the value of adding multiple azulene subunits into PAH systems for tuning of electronics.

2.3.2 Experimental

2.3.2.1 General Information

Pentacene-6,13-dione was purchased from TCI. $PdCl_2(PPh_3)_2$ was purchased from STREM. All other reagents and solvents were purchased from Sigma Aldrich. Dry and

deoxygenated solvents were used in all syntheses unless otherwise stated and were prepared by elution through a dual column solvent system (Glass Contour Solvent Systems). All reactions were carried out in oven-dried glassware and under nitrogen using standard Schlenk techniques or in an argon-filled glovebox unless noted otherwise. Column chromatography was performed using a CombiFlash® SG100c system using RediSepTM normal phase silica columns (ISCO, Inc., Lincoln, NE). ^{1}H NMR (400 MHz) and ^{13}C NMR (100 MHz) spectra were recorded on Bruker DRX-300 and Bruker DRX-400 spectrometers at room temperature and can be found in Appendix A.3. Synthesis of 2-(azulen-2-yl)-4,4,5,5-tetramethyl-1,3,2-dioxaborolane (**2.12**) and 6,13-bis(dibromomethylene)-6,13-dihydropentacene (**2.13**) were performed according to reported procedures.[30,21]

Synthesis of 6,13-bis(diazulen-2-ylmethylene)-6,13-dihydropentacene (2.14)

To a 50-mL two-neck round bottom flask, 2-(azulen-2-yl)-4,4,5,5-tetramethyl-1,3,2-dioxaborolane (**2.12**) (0.564 g, 2.2 mmol), 6,13-bis(dibromomethylene)-6,13-dihydropentacene (**2.13**) (0.275 g, 0.44 mmol), K_2CO_3 (0.920 g, 6.7 mmol), THF (130 mL), and H_2O (30 mL) were added with a stirbar. A reflux condenser was placed on one neck of the flask and the solution was bubbled for 15 minutes through a rubber septum in the other neck. To the flask, $PdCl_2(PPh_3)_2$ (0.016g, 0.022 mmol) was added and the reaction was bubbled again for 5 minutes. The reaction was heated to 70^{o}C for 24 hours. After cooling the reaction, water (5 mL) was added. The THF was removed under vacuum and the reaction mixture was extracted with dichloromethane. The organic layer was washed with saturated NaCl, dried with Na_2SO_4, and concentrated to give a dark green residue. The crude product was purified by column chromatography (35% dichloromethane in hexanes) to give a dark green solid in 64% yield. ^{1}H NMR (400 MHz, Methylene Chloride-d_2) δ (ppm): 8.25-8.22 (m, 8H), 7.71 (s, 4H), 7.55-7.48 (m, 12H), 7.28-7.25 (m, 4H), 7.17-7.11 (m, 12 H). ^{13}C NMR (100 MHz, Chloroform-d_1) δ (ppm): 140.26, 138.77, 138.19, 136.38, 136.23, 135.99, 127.81, 127.13, 125.43, 125.09, 123.21, 122.74, 119.61.
Molecular Mass (Ion mode:FAB): calculated for $C_{64}H_{40}$ 808.3, found 808.3.

Synthesis of tetraazuleno[1,2-*d*:2',1'-*g*:1'',2''-*m*:2''',1'''-*p*]dibenzo[*a*,*j*]coronene (2.9)

Part I: The photolysis setup has been previously described. A mixture of compound **2.14** (0.083 g, 0.11 mmol), iodine (0.133 g, 0.52 mmol), and propylene oxide (20 mL) in 300 mL of anhydrous benzene was irradiated with UV light (Hanovia 450 W high-pressure quartz Hg-vapor lamp) in an immersion well. Nitrogen was bubbled through the reaction vessel during the reaction. The apparatus was submerged in a large bath of water to maintain a constant temperature. After irradiating for 5 hours, the solvent was removed under vacuum and methanol was added to the resulting residue. The solution was filtered through a Millipore to give a red solid (0.049 g) in 58 % yield. Product was only slightly soluble in methylene chloride. ^{1}H NMR (400 MHz, Methylene Chloride-d_2) δ (ppm): see supplemental figure A.20.

Product from Part I was used in Part II without further purification.

Part II: The product from Part I (0.024 g, 0.030 mmol) was dissolved in dichloromethane (100 mL) in a 250 mL round bottom flask with a stirbar. The reaction was bubbled with nitrogen for 10 minutes before dropwise addition of $FeCl_3$ (0.040 g, 0.24 mmol) dissolved in CH_3NO_2 (0.25 mL). The reaction was stirred under nitrogen for 15 hours. To the reaction mixture, 75 mL of methanol was added and dichloromethane was removed under vacuum. The precipitate was collected using a Millipore filtration system to give a black-red solid in 95% yield. This product was only sparingly soluble in THF. ^{1}H NMR (400 MHz, tetrahydrofuran-d_8) δ (ppm): see supplemental figure A.21.

2.3.2.2 UV-vis Titration Experiment

To perform this experiment, a stock solution of **2.14** was prepared. The concentration of **2.14** was kept constant and the amount of concentrated TFA added was varied. The total volume of all solutions was brought up to 2 mL. All solutions were allowed to equilibrate for 5 minutes before the measurement was taken.

2.3.2.3 Calculations

All density functional theory calculations were performed using Jaguar.[32] Geometries were optimized, orbitals were calculated, and energies were determined all at the B3LYP/6-31G** level. We report final energies, orbital energies, and final geometries.

2.3.3 Conclusions

While characterization of azulene HBC **2.9** proved to be difficult due to solubility issues, preliminary results demonstrate that incorporation of azulene units into an HBC structure dramatically impacts the electronics of the system. Calculations suggest that **2.9** is a much lower band gap material than previously reported HBC derivatives, with a significant red-shift in absorption supporting these calculations. Intermediate azulene bisolefin **2.14** has very different properties from its HBC bisolefin relative, with calculations and UV-vis absorption supporting a lower band gap than even HBC **2.2**. UV-vis titration experiments show that the band gap is tunable with addition of acid.

2.4 Acknowledgements

The author would like to thank Professor Kyle Plunkett for his assistance on the synthesis and study of **2.2** - **2.4**. Professor Felix Fisher and Dr. Kumar Bharat are recognized for their intellectual contribution to the azulene HBC project. The author would like to acknowledge Dr. Michael Steigerwald and Ying Wu for the calculations. The author would like to thank Dr. Louis Brus for the use of his fluorometer.

2.5 References

[1] H. Seyler, M. Purushothaman, D. J. Jones, A. B. Holmes, W. W. H. Wong, *Pure Appl. Chem.* **2012**, *84*, 1047-1067.

[2] S. Xiao, M. Myers, Q. Miao, S. Sanaur, K. Pang, M. L. Steigerwald, C. Nuckolls, *Angew. Chem. Int. Ed.* **2005**, *44*, 7390-7394.

[3] N. J. Tremblay, A. A. Gorodetsky, M. P. Cox, T. Schiros, B. Kim, R. Steiner, Z. Bullard, A. Sattler, W.-Y. So, Y. Itoh, M. F. Toney, H. Ogasawara, A. P. Ramirez, I. Kymissis, M. L. Steigerwald, C. Nuckolls, *ChemPhysChem* **2010**, *11*, 799-803.

[4] L. Schmidt-Mende, A. Fechtenkötter, K. Müllen, E. Moons, R. H. Friend, J. D. MacKenzie, *Science* **2001**, *293*, 1119-1122.

[5] T. Kawase, H. Kurata, *Chem. Rev.* **2006**, *106*, 5250-5273.

[6] A. Sygula, F. R. Fronczek, R. Sygula, P. W. Rabideau, M. M. Olmstead, *J. Am. Chem. Soc.* **2007**, *129*, 3842-3843.

[7] P. E. Georghiou, L. N. Dawe, H.-A. Tran, J. Strübe, B. Neumann, H.-G. Stammler, D. Kuck, *J. Org. Chem.* **2008**, *73*, 9040-9047.

[8] S. Mizyed, P. E. Georghiou, M. Bancu, B. Cuadro, A. K. Rai, P. Cheng, L. T. Scott, *J. Am. Chem. Soc.* **2001**, *123*, 12770-12774.

[9] I. Sánchez-Molina, C. G. Claessens, B. Grimm, D. M. Guldi, T. Torres, *Chem. Sci.* **2013**, *4*, 1338-1344.

[10] Y. S. Cohen, S. Xiao, M. L. Steigerwald, C. Nuckolls, C. R. Kagen, *Nano Lett.* **2006**, *6*, 2838-2841.

[11] A. A. Gorodetsky, C.-Y. Chiu, T. Schiros, M. Palma, M. Cox, Z. Jia, W. Sattler, I. Kymissis, M. Steigerwald, C. Nuckolls, *Angew. Chem. Int. Ed.* **2010**, *49*, 1-5.

[12] S. Xiao, S. J. Kang, Y. Wu, S. Ahn, J. B. Kim, Y.-L. Loo, T. Siegrist, M. L. Steigerwald, H. Li, and C. Nuckolls, *Chem. Sci.* **2013**, *4*, 2018-2023.

[13] size-matching

[14] D. M. Lemal, G. D. Goldman, *J. Chem. Ed.* **1988**, *65*, 923-925.

[15] N. Sprutta, M. Siczek, L. Latos-Grażyński, M. Pawlicki, L. Szterenberg, T. Lis, *J. Org. Chem.* **2007**, *72*, 9501-9509.

[16] S. Ito, M. Ando, A. Nomura, N. Morita, C. Kabuto, H. Mukai, K. Ohta, J. Kawakami, A. Yoshizawa, A. Tajiri, *J. Org. Chem.* **2005**, *70*, 3939-3949.

[17] E. Amir, R. J. Amir, L. M. Campos, C. J. Hawker, *J. Am. Chem. Soc.* ***2011***, *13*, 10046-10049.

[18] A. Muranaka, M. Yonehara, M. Uchiyama, *J. Am. Chem. Soc.* **2010**, *132*, 7844-7845.

[19] F. Wang, Y.-H. Lai, N. M. Kocherginsky, Y. Y. Kosteski, *Org. Lett.* **2003**, *5*, 995-998.

[20] M. Koch, O. Blacque, K. Venkatesan, *Org. Lett.* **2012**, *14*, 1580-1583.

[21] C.-Y. Chiu, B. Kim, A. A. Gorodetsky, W. Sattler, S. Wei, A. Sattler, M. Steigerwald, C. Nuckolls, *Chem. Sci.* **2011**, *2*, 1480-1486.

[22] A. C. Whalley, K. N. Plunkett, A. A. Gorodetsky, C. L. Schenck, C.-Y. Chiu, M. L. Steigerwald, C. Nuckolls, *Chem. Sci.* **2011**, *2*, 132-135.

[23] A. C. Whalley, *Carbon nanotubes: Single-molecule electronics and progress towards end cap synthesis,* PhD Thesis*,* Columbia University, **2009.**

[24] L. Wang, P. B. Shevlin, *Org. Lett.*, **2000**, *2*, 3703-3705.

[25] H. A. Reisch, M. S. Bratcher, L. T. Scott, *Org. Lett.*, **2000**, *2*, 1427-1430.

[26] L. Wang, P. B. Shevlin, *Tet. Lett.,* **2000**, *41*, 285-288.

[27] H. Dang, M. Levitus, M. A. Garcia-Caribay, *J. Am. Chem. Soc.,* **2002**, *124*, 136-143.

[28] V. O. Stern and M. Volmer, *Physik. Zeitschr.,* **1919**, *20*, 183-188.

[29] A. M. Brouwer, *Pure Appl. Chem.* **2011**, *83*, 2213-2228.

[30] M. Fujinaga, T. Murafuji, K. Kurotobi, Y. Sugihara, *Tetrahedron,* **2009**, *65*, 7115-7121.

[31] Y. S. Cohen, S. Xiao, M. L. Steigerwald, C. Nuckolls, C. R. Kagan, *Nano Lett.,* **2006**, *6*, 2838-2841.

[32] Schrodinger, *Jaguar*. Version 7.8. Schrodinger LLC. New York, NY, USA **2010**.

Chapter 3. Understanding Single Molecule Conductance of Cobalt Chalcogenide Clusters

Part of this chapter was reproduced from a paper published in *Angewandte Chemie International Edition* by © Wiley-VCH Verlag GmbH & Co.: "Quantum Soldering of Individual Quantum Dots" by Dr. Xavier Roy, Christine L. Schenck, Seokhoon Ahn, Prof. Roger A. Lalancette, Prof. Latha Venkataraman, Prof. Colin Nuckolls, and Dr. Michael L. Steigerwald. *Angewandte Chemie International Edition* 2012, **51**, 12473-12476. **DOI:** 10.1002/anie.201206301.

3.1 Introduction

Here we describe a precise method to make electrical contact to an individual quantum dot (QD). This supramolecular construction connects the QD to its macroscopic environment, yet it does not disturb the nanoscopic quantum mechanical confinement of the excitons in these small solids. Quantum mechanical confinement has given rise to the hallmark optical properties of QDs,[1-3] but it has been of only limited use in electronic and opto-electronic applications[3] of QDs because of three interrelated problems: (i) the lack of knowledge of how to make innocent electrical contact to QDs; (ii) the challenge of synthesizing atomically precise QDs; and (iii) not having the methods to efficiently wire individual QDs in electrical devices. Robust electrical contact to the core of QDs is essential in the development of QD-based electronic devices[3-8] and for the extraction of hot electrons[9] and the separation of charges from multiple exciton states[10,11] in QDs solar cells, yet it has only been thoroughly explored in the context of thin films and bulk samples of QDs[12-17] where performance cannot be related to the poorly characterized structure and quantum confinement is compromised at best.

Previously, a scanning tunneling microscope based break-junction (STM-BJ) technique was used to study the single molecule conductance of cobalt chalcogenide clusters with alkyl phosphine ligands.[8] The single molecule conductance pathway was determined to be from gold electrode directly to the chalcogenide in the cluster core, with bulkier phosphine ligands shutting off the conductance. The alkyl phosphine ligands do not participate in the conductance pathway

and the bulkier alkyl phosphine ligands act as an insulating shell around the cluster core. This led to the question of whether ligands could be designed to actively participate in the conductance pathway.

Here we synthesize, for the first time, a molecularly-discrete, crystallographically defined, electron-rich, metal chalcogenide cluster, Co_6Se_8,[18] that is capped with conjugated, molecular connectors that can couple electronically to nanoscale electrodes. We show that these connectors provide a well-defined electronic pathway for the transport of charge carriers through a single QD. We measure the conductance of individual QDs using STM-BJ techniques[19-21] and compare our results with density functional theory. Finally, we show that we can control the electronic coupling between the core of the QD and the conducting backbone of the connector by varying the connector structure allowing us to differentiate between conductive molecular connectors and insulating ones. These results establish quantum mechanical design rules for controlling the electronic coupling to a QD for the creation of QD-based electrical circuits.

3.2 Results and Discussion

The solid-state compound CoSe is an infrared bandgap semiconductor.[22] We synthesized a series of atomically precise cobalt selenide quantum dots[18,23,24] decorated with different molecular connectors (**L3.2**–**L3.5**). Connectors **L3.2**–**L3.4** have a phosphine end that coordinates to the cobalt atom in the cluster and a thiomethyl end that is aurophilic. Connector **L3.5** lacks a thiomethyl group and serves as a control. We selected this family of compounds based on the parent QD $Co_6Se_8(PEt_3)_6$ (**3.1**) (Figure 3.1b) because its electron-rich core is a reservoir of carriers, and its synthesis is amenable to a broad range of phosphines. Single crystal X-ray diffraction (SCXRD) shows that the Co_6Se_8 core of the clusters, **3.1**–**3.5**, are isostructural (Figure 3.2), forming an octahedron of Co atoms concentric with a cube of Se atoms. Cluster **3.4** packs with its six molecular connectors grouped into two diametrically opposed groups of three, resulting in an ideal conformation for bridging a linear gap between two electrodes, as illustrated in Figure 3.1a.

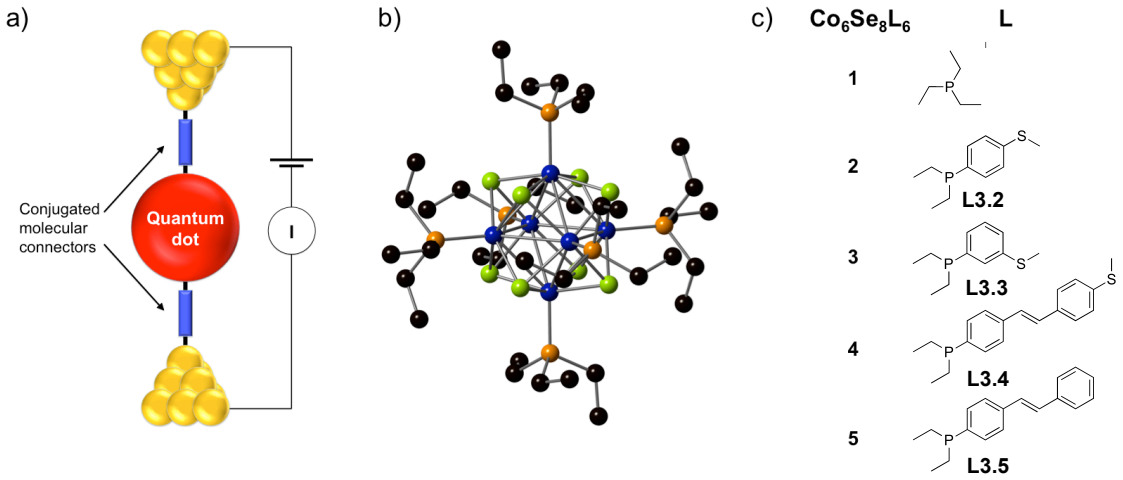

Figure 3.1. Making electrical contact to an atomically precise QD. a) Schematic of a single-cluster junction formed between nanoscale electrodes and molecular connectors. b) Molecular structure of the parent cluster $Co_6Se_8(PEt_3)_6$ (**3.1**). Carbon, black; cobalt, blue; phosphorus, orange; selenium, green. c) Chemical structures of the different clusters investigated in this study.

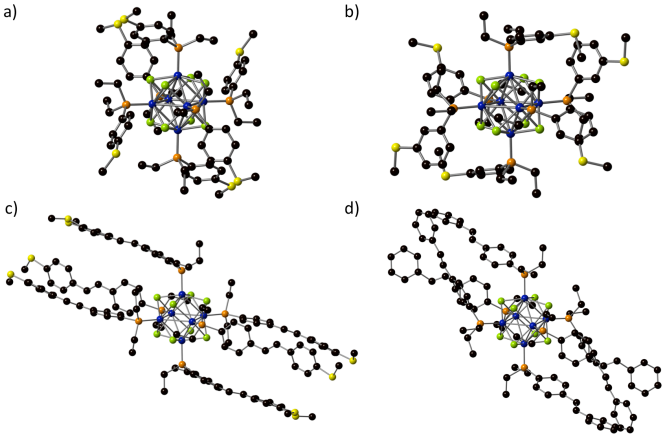

Figure 3.2. SCXRD characterization of the clusters. a–d) show the molecular structures of clusters **3.2**–**3.5**, respectively. The hydrogen atoms and solvent molecules of crystallization have been omitted. Carbon, black; cobalt, blue; phosphorus, orange; sulfur, yellow; selenium, green. The Co-P, Co-Se and Co-Co bond lengths for clusters **3.1**–**3.5** are in the range 2.12-2.14 Å, 2.32-2.36 Å and 2.88-2.97 Å, respectively. These distances change little in a given cluster and throughout the cluster series. The methyl group on one of the sulfur atoms in cluster **3.4** is disordered between two orientations (the site-occupancy-factor is 0.75:0.25).

We measured the conductance of both the individual QD **3.2**–**3.5**, and the free connectors, **L3.2**–**L3.5** using a STM-BJ technique.[19] STM-BJ measurements use a gold tip and

gold substrate to repeatedly form and break gold point contacts in solutions of the target compounds in 1,2,4-trichlorobenzene as solvent. Clusters **3.2**–**3.4** can bind to the Au electrodes *via* thiomethyl groups[25] while **3.5**, which lacks thiomethyl groups, cannot. The conductance across the Au gap is measured versus the tip/substrate separation at an applied voltage of 500 mV and 750 mV for **L3.2**–**L3.5** and **3.2**–**3.5**, respectively. In the inset of Figure 3.3a and 3.3b, we show sample traces measured for **3.2**, **3.4**, **L3.2**, and **L3.4**. These conductance traces show plateaus with lengths and conductance that characterize each compound, indicating that each forms junctions.

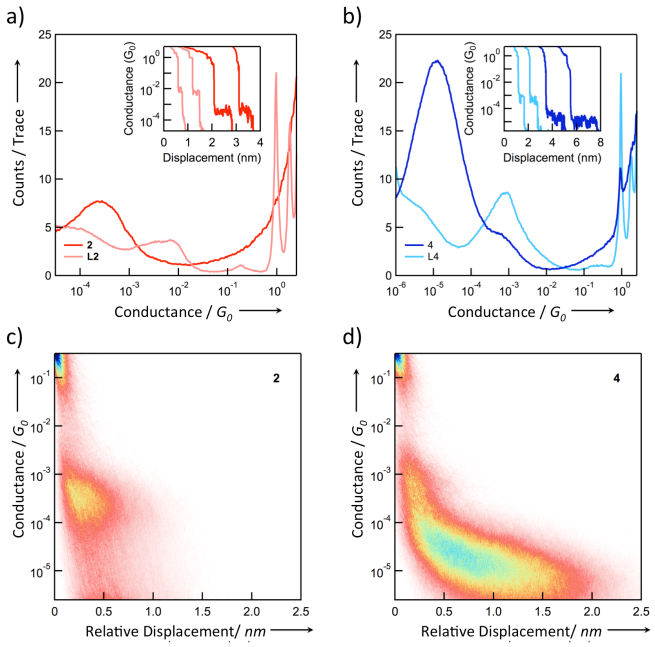

Figure 3.3. Single-cluster junctions. Logarithm-binned conductance histograms constructed using over 5000 traces for (a) connector **L3.2** (pink) and cluster **3.2** (red) and (b) connector **L3.4** (light blue) and cluster **3.4** (blue). Bin size is 100/decade. The insets show individual conductance traces. (c) and (d) show 2D conductance histograms for clusters **3.2** and **3.4**, respectively. The conductance peaks extend over a distance of 0.7 nm for **3.2** and 1.8 nm for **3.4** relative to the break of the G_0 contact.

We created one-dimensional (1D) conductance and two dimensional (2D) conductance-displacement histograms from the conductance traces.[21] Figures 3.3a and 3.3b show 1D conductance histograms generated using logarithm bins for **3.2**, **3.4**, **L3.2** and **L3.4**. The histograms for the clusters do not overlap those of the corresponding connectors confirming that

stable cluster junctions indeed form with **3.2** and **3.4**. The lower conductance of **3.2** and **3.4**, when compared with that of **L3.2** and **L3.4** is consistent with longer molecules spanning the junctions. The heights of the conductance peak for the clusters decrease after measurement of several thousand traces, possibly due to degradation under ambient conditions.

The 2D conductance-displacement histograms for **3.2** and **3.4**, shown in Figure 3.3c and 3.3d, extend to ~0.7 nm and ~1.8 nm, respectively. These are significantly longer than for the corresponding connectors (2D histograms for **L3.2** and **L3.4** are shown in Figure B.1) and agree with previous measurements showing that longer molecules can bind further away from the apex of the Au electrodes and change their binding site on the electrode as the junctions are elongated.[21,26]

Cluster **3.5** lacks aurophilic thiomethyl functionality. Neither the 1D nor 2D conductance histograms for **3.5** (Figures B.2 and B.3) show peaks as those of **3.4**. This suggests that cluster **3.4** forms molecular junctions by bonding its terminal thiomethyl groups to the Au electrodes, while **3.5** does not.

Comparison of **3.2** and **3.3** demonstrates the effect of the connector substitution pattern on the conductance of the cluster. Although the meta-substituted connector **L3.3** shows a clear conductance peak that we ascribe to σ-conduction,[27-29] cluster **3.3** shows no peak (Figure B.2). This indicates that no end-to-end electronic pathway exists in **3.3**. There is also no stepwise pathway by which a carrier can travel from one electrode to the cluster core and then to the second electrode. Thus when **L3.3** binds to the cluster its 3-thiomethylphenyl substituent does not rotate around the P-C bond to enable conduction through a σ-pathway between the sulfur and the cluster core. These results show that we can effectively modulate the conductivity of a QD device by tuning the chemistry of the connectors by varying the substitution pattern or removing of the aurophilic group.

Electronic absorption spectroscopy, cyclic voltammetry, ^{1}H- and ^{31}P-NMR spectroscopies, and electronic structure calculations further characterize these molecular circuit elements. The absorption spectra (Figures B.4-B.8) show that modifying the connectors changes the Co_6Se_8 core very little. The three longer-wavelength absorptions that characterize **3.1** remain

essentially unchanged in **3.2**–**3.5**. The connectors **L3.2**–**L3.5** absorb in the near-UV and **3.2**–**3.5** show similar absorptions. The spectra of the clusters are simply the sum of the spectra of the isolated constituent parts. This conclusion is supported by voltammetry of **3.2**–**3.5** (Figures B.9-B.12). Each cyclic voltammogram shows one reversible reduction and two reversible oxidations - identical behavior (and at essentially identical potentials) to **3.1**. We see no redox processes for the connectors on their own (**L3.2**–**L3.5**)**.** Thus multiple charged states are reversibly accessible in **3.2**–**3.5**: the cluster core contains a number of stored charge carriers that can be transferred onto a macroscopic electrode. This voltammetry is complementary to the STM-BJ experiments that show the transport of charge carriers through conductive molecular connectors. The ^{1}H-NMR spectra of **3.2**–**3.5** are essentially the same as for **L3.2**–**L3.5**. The single ^{31}P-NMR resonances for **3.2**–**3.5** are significantly broader than and and shifted downfield from those of **L3.2**–**L3.5**, respectively, by ~75 ppm.

These data show that in most ways the clusters **3.1**–**3.5** are essentially identical; the differences in electronic absorption, chemical structure (determined both in the solid by SCXRD and in solution by NMR), and electronic structure (determined by cyclic voltammetry) are minor. In only two aspects do these clusters differ: **3.2** and **3.4** are electrically conductive, and they are much more sensitive to air than are the others. For example, we can record sharp, well-defined ^{1}H-NMR spectra for all of the clusters, but the spectra of **3.2** and **3.4** broaden rapidly after the

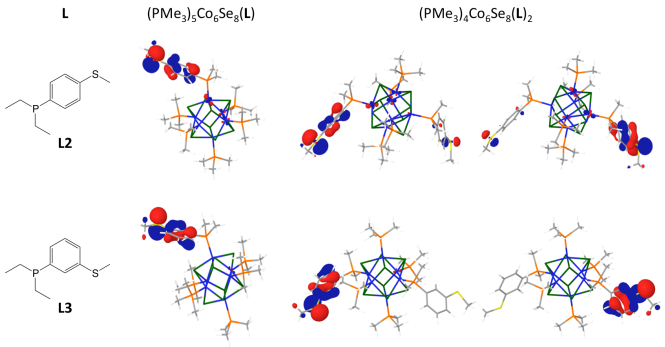

Figure 3.4. Model computational studies of clusters **3.2** and **3.3** using density functional theory. The orbitals associated with the sulfur pπ lone pairs for the models $(PMe_3)_5Co_6Se_8$(**L3.2**), $(PMe_3)_5Co_6Se_8$(**L3.3**) $(PMe_3)_4Co_6Se_8$(**L3.2**)$_2$ and $(PMe_3)_4Co_6Se_8$(**L3.3**)$_2$ are shown.

samples are exposed to air while those of the other three clusters remain sharp. We suggest that these two features, molecular conductance and chemical reactivity, are two facets of the same fundamental property: access to the Co_6Se_8 core that is granted by **L3.2** and **L3.4** but forbidden by PEt_3, **L3.3**, and **L3.5**.

We and others have shown that 1,4-disubstitution on phenyl rings can give conductive, conjugated systems while compositionally similar 1,3-disubstitution gives insulating, cross-conjugated systems.[27-29] The present results extend this to include substituted phenyl phosphine ligands in metal-containing systems, and we use density functional theory to study this. We modeled **3.2, 3.3** (Figure 3.4), and **3.4** (Figure B.13) with the simpler clusters, $(PMe_3)_5Co_6Se_8$(**L3.2**) and $(PMe_3)_5Co_6Se_8$(**L3.3**), and $(PMe_3)_5Co_6Se_8$(**L3.4**), respectively. The electronic structures of the three model clusters are very similar; the salient difference is in the orbitals that are most nearly identified with the pπ lone pairs on the sulfur atoms. Comparison of these orbitals in the model clusters indicates that the thiomethyl substituents are coupled more strongly to the cluster core in **3.2** and **3.4** than in **3.3**. We believe that the corresponding orbitals in **3.2** and **3.4** provide conduits through which electrons may move from the cluster to its ambient surroundings - either to effect electrical conduction in the break-junction or to mediate reaction with oxygen.

We supplemented these calculations with studies in which the Co_6Se_8 core was protected with four spectator PMe_3 ligands and two of the thiomethyl-containing ligands ($(PMe_3)_4Co_6Se_8$(**L**)$_2$) to characterize the electronic communication between antipodal aurophilic sites. We observe that the essential electronic structure of the cluster is unchanged; the significant differences again appear in the orbitals most readily associated with the sulfur pπ lone pairs (and also the C=C bond in the case of **L3.4**). We find that there is a clear, single-orbital pathway between the two antipodal points in $(PMe_3)_4Co_6Se_8$(**L3.2**)$_2$ and $(PMe_3)_4Co_6Se_8$(**L3.4**)$_2$ that is absent in $(PMe_3)_4Co_6Se_8$(**L3.3**)$_2$. These results are consistent with our experimental observations that **3.2** and **3.4** are electrically conductive and air-sensitive.

3.3 Experimental

3.3.1. Synthetic Details

3.3.1.1 General Information

Chlorodiethylphosphine was purchased from Acros Organics. Selenium powder and dicobalt octacarbonyl were obtained from STREM Chemicals. Diethyl benzylphosphonate, 4-bromobenzaldehyde, potassium tert-butoxide, 4-bromothioanisole, 3-bromothioanisole, 4-(methylthio)benzylbromide, trimethylphosphite, 1,2,4-trichlorobenzene, and all other reagents and solvents were purchased from Aldrich. Dry and deoxygenated solvents were prepared by elution through a dual column solvent system (Glass Contour Solvent Systems). Unless otherwise noted, all reactions were carried out under nitrogen using standard schlenk techniques or in an argon-filled glovebox. Only the IR peaks in the range 4000-1500 cm^{-1} are reported.

3.3.1.2 Stilbene Synthesis

General Horner-Wadsworth-Emmons reaction:

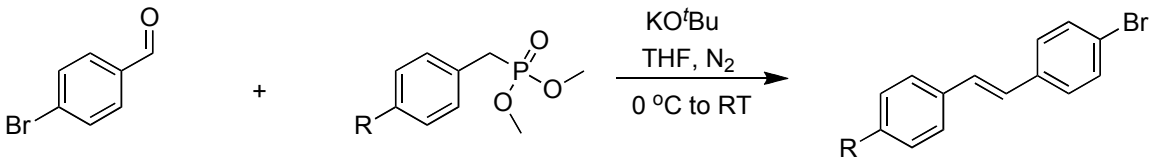

4-Bromo-4′-thiomethylstilbene: 4-Bromobenzaldehyde (0.89 g, 4.8 mmol) was dissolved in 40 mL of THF and cooled to 0 °C. Dimethyl-4-thiomethylbenzyl phosphonate[30] (1.18 g, 4.8 mmol) was added and the solution was stirred for 30 min. A solution of potassium *tert*-butoxide (0.62 g, 5.5 mmol) in 10 mL of THF was added dropwise to the cold reaction over 15 min. The reaction was stirred and warmed to RT overnight. In air, 50 mL of water was added and the mixture was poured into 50 mL of dichloromethane. The organic phase was extracted and the aqueous phase was washed twice with 10 mL of dichloromethane. The combined organic phase was washed

with water and brine, dried with $MgSO_4$ and evaporated to dryness. The white solid was recrystallized at -30 °C from a mixture of toluene and hexanes. Yield: 1.35 g (92 %).

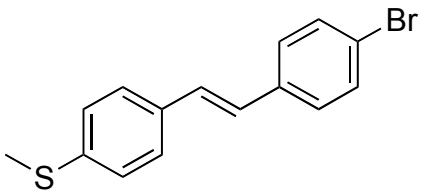

^{1}H NMR (300 MHz, [d_2-dichloromethane], 298 K): δ = 2.50 (3H, s), 7.00 (2H, m), 7.21-7.25 (2H, m), 7.32-7.48 (6H, m). IR (ATR) = 3079, 3015, 2917, 1903, 1834, 1628, 1590, 1551 cm^{-1}.

4-Bromostilbene: 4-Bromobenzaldehyde (2.10 g, 11.4 mmol) was dissolved in 50 mL of THF and cooled to 0 °C. Diethyl benzylphosphonate (2.61 g, 11.4 mmol) was added and the solution was stirred for 30 min. A solution of potassium tert-butoxide (1.40 g, 12.5 mmol) in 10 mL of THF was added dropwise to the cold reaction over 15 min. The reaction was stirred and warmed to RT overnight. In air, 50 mL of water was added and the mixture was poured into 50 mL of dichloromethane. The organic phase was extracted and the aqueous phase was washed twice with 10 mL of dichloromethane. The combined organic phase was washed with water and brine, dried with $MgSO_4$ and evaporated to dryness. The white solid was recrystallized at -30 °C from a mixture of toluene and hexanes. Yield: 2.44 g (83 %).

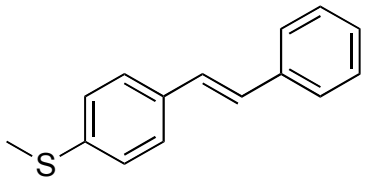

^{1}H NMR (300 MHz, [d_2-dichloromethane], 298 K): δ = 7.10 (2H, m), 7.26-7.31 (1H, m), 7.35-7.54 (8H, m). IR (ATR) = 3081, 3060, 3026, 2922, 1970, 1953, 1904, 1831, 1785, 1732, 1667, 1645, 1583 cm^{-1}.

3.3.1.3 General Synthesis of the Phosphine Ligands

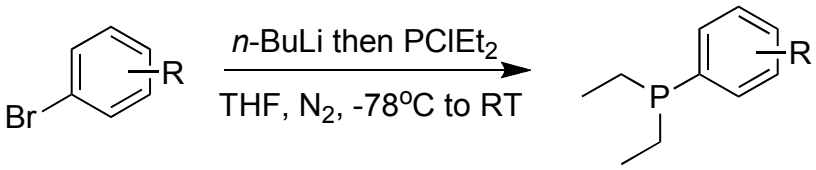

Diethyl-4-thiomethylphenylphosphine (L3.2): 4-Bromothioanisole (1.51g, 7.4 mmol) was dissolved in 50 mL of THF and cooled to -78 °C. n-Butyllithium (1.6 M in hexanes, 5.1 mL, 8.1 mmol) was added dropwise and the reaction was stirred for 45 min. Chlorodiethylphosphine (1.10 g, 8.8 mmol) in 10 mL of THF was added dropwise to the solution and the reaction was warmed 2 gradually to RT overnight. The solvent was removed under vacuum and 20 mL of toluene was added to the crude product. The mixture was filtered through a fine frit to remove LiCl and the solvent was once again removed under vacuum. The pale yellow oil obtained was distilled under vacuum at 110 °C to give a colorless oil. Yield: 1.32 g (84 %).

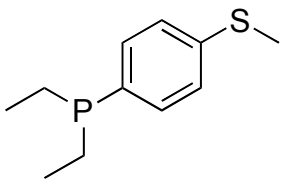

^{1}H NMR (400 MHz, [d_2-dichloromethane], 298 K): δ = 0.99 (6H, m), 1.66 (4H, m), 2.48 (3H, s), 7.23 (2H, m), 7.40 (2H, m). ^{31}P NMR (162 MHz, [d_2-dichloromethane], 298 K): δ = -16. IR (ATR) = 2957, 2927, 2871, 1885, 1634, 1579 cm^{-1}.

Diethyl-3-thiomethylphenylphosphine (L3.3): 3-Bromothioanisole (1.06 g, 5.2 mmol) was dissolved in 40 mL of THF and cooled to -78 °C. n-Butyllithium (1.6 M in hexanes, 3.6 mL, 5.7 mmol) was added dropwise and the reaction was stirred for 45 min. Chlorodiethylphosphine (0.78 g, 6.2 mmol) in 10 mL of THF was added dropwise to the solution and the reaction was warmed gradually to RT overnight. The solvent was removed under vacuum and 20 mL of toluene was added to the crude product. The mixture was filtered through a fine frit to remove LiCl and the solvent was once again removed under vacuum. The pale yellow oil obtained was distilled under vacuum at 110 °C to give a colorless oil. Yield: 0.78 g (71 %).

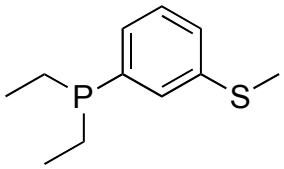

^{1}H NMR (500 MHz, [d_2-dichloromethane], 298 K): δ = 1.00 (6H, m), 1.68 (4H, m), 2.49 (3H, s), 7.20-7.29 (3H, m), 7.36-7.37 (1H, m). ^{31}P NMR (236 MHz, [d_2-dichloromethane], 298 K): δ = -14. IR (ATR) = 2959, 2931, 2876, 1635, 1574, 1562 cm^{-1}.

Diethyl-4'-thiomethyl-4-stilbenylphosphine (L3.4): 4-Bromo-4′ -thiomethylstilbene (1.16 g, 3.8 mmol) was dissolved in 50 mL of THF and cooled to -78 °C. n-Butyllithium (1.6 M in hexanes, 2.6 mL, 4.2 mmol) was added dropwise and the reaction was stirred for 45 min. Chlorodiethylphosphine (0.57 g, 4.6 mmol) in 10 mL of THF was added dropwise to the solution and the reaction was warmed gradually to RT overnight. The solvent was removed under vacuum and 20 mL of toluene was added to the crude product. The mixture was filtered through a fine frit to remove LiCl and the solvent was once again removed under vacuum. The white solid was recrystallized at -30 °C from a mixture of toluene and n-hexane. Yield: 1.00 g (84 %).

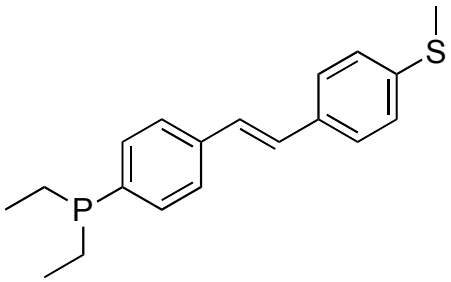

^{1}H NMR (400 MHz, [d_2-dichloromethane], 298 K): δ = 1.02 (6H, m), 1.70 (4H, m), 2.50 (3H, s), 7.10-7.11 (2H, m), 7.25 (2H, m), 7.45-7.51 (6H, m). ^{31}P NMR (162 MHz, [d_2-dichloromethane], 298 K): δ = -15. IR (ATR) = 3066, 3018, 2950, 2924, 2901, 2866, 2821, 1899, 1833, 1630, 1588, 1547 cm^{-1}.

Diethyl-4-stilbenylphosphine (L3.5): 4-Bromostilbene (0.49 g, 1.9 mmol) was dissolved in 40 mL of THF and cooled to -78 °C. n-Butyllithium (1.6 M in hexanes, 1.3 mL, 2.1 mmol) was added

dropwise and the reaction was stirred for 45 min. Chlorodiethylphosphine (0.28 g, 2.3 mmol) in 10 mL of THF was added dropwise to the solution and the reaction was warmed gradually to RT overnight. The solvent was removed under vacuum and 20 mL of toluene was added to the crude product. The mixture was filtered through a fine frit to remove LiCl and the solvent was once again removed under vacuum. The white solid was recrystallized at -30 °C from n-hexane. Yield: 0.38 g (75 %).

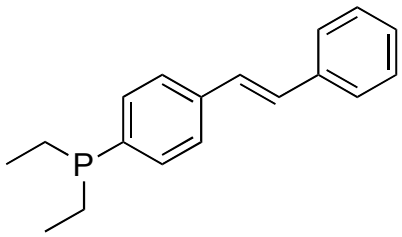

^{1}H NMR (400 MHz, [d_2-dichloromethane], 298 K): δ = 1.01 (6H, m), 1.70 (4H, m), 7.15 (2H, m), 7.27 (1H, m), 7.37 (2H, m), 7.46-7.55 (6H, m). ^{31}P NMR (162 MHz, [d_2-dichloromethane], 298 K): δ = -15. IR (ATR) = 3064, 3020, 2955, 2927, 2912, 2869, 1950, 1915, 1828, 1597, 1576, 1548 cm^{-1}.

3.3.1.4 General Synthesis of the $Co_6Se_8L_6$ Clusters:

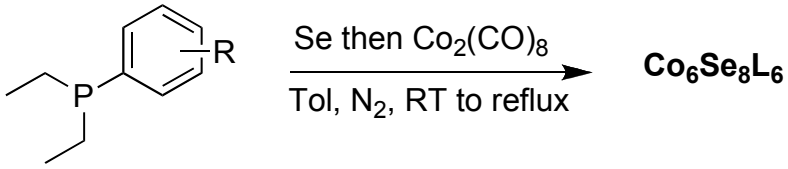

Cluster 3.1: Cluster **3.1** was synthesized according to a published procedure (9).

^{1}H NMR (400 MHz, [d_6-benzene], 298 K): δ = 1.10 (36H, m), 1.96 (24H, m). ^{31}P NMR (162 MHz, [d6-benzene], 298 K): δ = 61 (broad peak). The ^{31}P peak for compound **3.1** is very broad and we believe that it was wrongly assigned in ref. 2. We report the corrected shift here. IR (ATR) = 2966, 2925, 2877 cm^{-1}.

Cluster 3.2: Diethyl-4-thiomethylphenylphosphine (**L3.2**) (0.38 g, 1.8 mmol) was dissolved in 25 mL of toluene. Selenium powder (0.14 g, 1.8 mmol) was added and the suspension was stirred until the solid completely dissolved. Dicobalt octacarbonyl (0.14 g, 0.4 mmol), dissolved in 10 mL of toluene, was added to the solution and the reaction was heated to reflux overnight. The mixture was cooled down to room temperature and filtered through a fine frit. The dark brown solution was concentrated under vacuum and the product was precipitated with diethyl ether. Yield: 0.12 g (37 %). Single crystals were grown by slow diffusion of n-hexane in a toluene solution of **3.2**.

^{1}H NMR (400 MHz, [d_8-tetrahydrofuran], 298 K): δ = 0.86 (36H, m), 1.97 (24H, m), 2.50 (18H, s), 7.15 (12H, m), 7.28 (12H, m). ^{31}P NMR (162 MHz, [d_8-tetrahydrofuran], 298 K): δ = 58 (broad peak). IR (ATR) = 3066, 2961, 2922, 2868, 1966, 1879, 1579, 1542 cm^{-1}.

Cluster 3.3: Diethyl-3-thiomethylphenylphosphine (**L3.3**) (0.6 g, 2.8 mmol) was dissolved in 40 mL of toluene. Selenium powder (0.22 g, 2.8 mmol) was added and the suspension was stirred until the solid completely dissolved. Dicobalt octacarbonyl (0.22 g, 0.6 mmol), dissolved in 10 mL of toluene, was added to the solution and the reaction was heated to reflux overnight. The mixture was cooled down to room temperature and filtered through a fine frit. The solvent was removed under vacuum to give a dark brown oil. Large black single crystals of **3.3** were grown from a mixture of diethyl ether and n-hexane. Yield: 0.23 g (46 %).

^{1}H NMR (400 MHz, [d_8-tetrahydrofuran], 298 K): δ = 0.88 (36H, m), 1.95 (24H, m), 2.48 (18H, s), 7.09-7.13 (12H, m), 7.16-7.20 (6H, m), 7.34 (6H, m). ^{31}P NMR (162 MHz, [d_8-tetrahydrofuran], 298 K): δ = 58 (broad peak). IR (ATR) = 3038, 2964, 2926, 2870, 2727, 1954, 1859, 1740, 1669, 1570, 1561 cm^{-1}.

Cluster 3.4: Diethyl-4'-thiomethyl-4-stilbenylphosphine (**L3.4**) (223 mg, 0.71 mmol) was dissolved in 40 mL of toluene. Selenium powder (56 mg, 0.71 mmol) was added and the suspension was stirred until the solid completely dissolved. Dicobalt octacarbonyl (56 mg, 0.16 mmol), dissolved in 5 mL of toluene, was added to the solution and the reaction was heated to reflux overnight. The hot mixture was filtered through a fine frit. The dark brown solution was concentrated under

vacuum and the product was precipitated with diethyl ether. Yield: 102 mg (65 %). Single crystals were grown by slow evaporation of a toluene solution of **3.4**.

^{1}H NMR (400 MHz, [d_8-tetrahydrofuran], 298 K): δ = 0.89 (36H, m), 2.06 (24H, m), 2.48 (18H, s), 7.13 (12H, s), 7.20 (12H, m), 7.32-7.43 (36H, m). ^{31}P NMR (162 MHz, [d_8-tetrahydrofuran], 298 K): δ = 58 (broad peak). IR (ATR) = 3018, 2963, 2921, 2872, 1629, 1586, 1545 cm^{-1}.

Cluster 3.5: Diethyl-4-stilbenylphosphine (**L3.5**) (300 mg, 1.12 mmol) was dissolved in 40 mL of toluene. Selenium powder (88 mg, 0.71 mmol) was added and the suspension was stirred until the solid completely dissolved. Dicobalt octacarbonyl (88 mg, 0.26 mmol), dissolved in 10 mL of toluene, was added to the solution and the reaction was heated to reflux overnight. The mixture was cooled down to room temperature and filtered through a fine frit. The dark brown solution was concentrated under vacuum and black single crystals of **3.5** were grown by slow evaporation of the solution. Yield: 125 mg (56 %).

^{1}H NMR (400 MHz, [d_8-tetrahydrofuran], 298 K): δ = 0.90 (36H, m), 2.06 (24H, m), 7.19-7.22 (18H, m), 7.28-7.31 (12H, m), 7.35-7.39 (12H, m), 7.44-7.49 (24H, m). ^{31}P NMR (162 MHz, [d_8-tetrahydrofuran], 298 K): δ = 56 (broad peak). IR (ATR) = 3075, 3056, 3025, 2962, 2931, 2907, 2874, 1942, 1875, 1823, 1633, 1597, 1575, 1551 cm^{-1}.

3.3.2 Instrumentation Details

All ^{1}H and ^{31}P NMR were recorded on a Bruker DRX300 (300 MHz), Bruker DRX400 (400 MHz), or Bruker DMX500 (500 MHz) spectrometer. Infrared (IR) spectra were obtained using a Perkin Elmer Spectrum 400 FTIR spectrometer using a PIKE ATR attachment. Absorption spectra were taken on a Shimadzu UV-1800 spectrophotometer. Electrochemistry was performed using a CHI600c potentiostat and analyzed using the CHI600c electrochemical analyzer software package. Single crystal X-ray diffraction data were collected on a Bruker SMART CCD APEX II diffractometer using a fine-focus sealed-tube graphite monochromator Cu K_α source (λ = 1.54178 Å). The conductance measurements were performed using a home-built modified scanning tunneling microscope (STM) that has been previously described.[31] Sub-

angstrom level control of the tip-substrate distance was achieved using a commercially available single-axis piezoelectric positioner (Nano-P15, Mad City Labs). The STM was controlled using a custom program using IgorPro (Wavemetrics, Inc.).

3.3.3 Conductance Measurements

The conductance of each molecule was measured using the STM-based break-junction technique, where an Au tip (Alfa Aesar, 99.999%) cut to be sharp is brought in and out of contact with a substrate of ~100 nm of gold (Alfa Aesar, 99.999%) evaporated onto cleaved mica disks. The substrate is mounted on a piezoelectric positioner (Mad City Labs), so that sub-angstrom resolution in position is achieved. During the entire break junction procedure, a bias (500 mV for the molecular connector and 750 mV for the complex) is applied between the tip and the substrate while the current is measured (Keithley 428-Prog). Piezo control and data collection were performed using a National Instruments PXI Chassis System (with PXI-4461, PXI-6289) at 40 kHz, and driven and managed with a custom-program using Igor Pro (Wavemetrics, Inc.).

The experimental set-up is kept under ambient. For each experiment, the substrate is cleaned under UV/Ozone for 15 minutes prior to use. For every conductance trace measurement, the STM tip is first brought into hard contact with the substrate to achieve a conductance greater than ~ 10 G_0. At this point, the junction electrodes are pulled apart at a speed of 15 nm/s for 0.25 seconds. Conductance is measured as a function of tip-sample displacement to generate conductance traces. For each tip/substrate pair, at least one set of 1,000 traces of clean gold breaks is collected to ensure the system is clean. Then, the target molecule, dissolved in 1,2,4-trichlorobenzene (1 mM) is deposited and over 5,000 conductance traces are collected for each of the molecules reported here. One-dimensional conductance histograms are created using every measured trace.

3.3.4 UV-vis Absorption Spectroscopy

All spectra were taken under nitrogen in a 1-cm quartz cuvette following a recording of the background spectrum.

3.3.5 Cyclic Voltammetry

A solution of clusters **3.2**-**3.5** in degassed, anhydrous dichloromethane containing 0.1 M of supporting electrolyte, tetrabutylammonium hexafluorophosphate ($TBAPF_6$) was used in a single cell. The measurements were carried out under nitrogen in a cell with a glassy carbon working electrode, a platinum wire counter electrode and a Ag^+/AgCl reference electrode with a scan rate of 0.1 V/s. The potentials are reported against a Ag^+/AgCl reference.

3.3.6 Crystallography

Crystals of **3.1** suitable for X-ray diffraction were grown by slow diffusion of *n*-hexane in a toluene solution of the compound. All measurements were made on a Bruker SMART CCD APEX II diffractometer[32] using a fine-focus sealed-tube graphite monochromator Cu K_α source (λ = 1.54178 Å). Of the 12,986 reflections that were collected, 1,958 were unique (R_{int} = 0.039); equivalent reflections were merged. Data were collected and integrated using the Bruker SAINT software package.[33] Data were corrected for absorption effects using a multi-scan technique (SADABS)[34] and numerical face-indexing with max and min transmission coefficients of 0.2095 and 0.1663, respectively. The structure was solved using SHELXTL.[35] All non-hydrogen atoms were refined anisotropically. All hydrogen atoms were found in electron-density difference maps, but placed in idealized positions and allowed to ride on their respective C atoms. The final cycle of full-matrix least-squares refinement on F^2 was based on 1,962 reflections and 88 variable parameters and converged. Cambridge Crystallographic Data Centre deposition number: 894787

Crystals of **3.2** suitable for X-ray diffraction were grown by slow diffusion of *n*-hexane in a toluene solution of the compound. All measurements were made on a Bruker SMART CCD APEX II diffractometer[32] using a fine-focus sealed-tube graphite monochromator Cu K_α source (λ = 1.54178 Å). Of the 40,988 reflections that were collected, 7,134 were unique (R_{int} = 0.049); equivalent reflections were merged. Data were collected and integrated using the Bruker SAINT software package.[33] Data were corrected for absorption effects using a multi-scan technique

(SADABS)[34] and numerical face-indexing with max and min transmission coefficients of 0.228 and 0.141, respectively. The structure was solved using SHELXTL.[35] All non-hydrogen atoms were refined anisotropically. All hydrogen atoms were found in electron-density difference maps, but placed in idealized positions and allowed to ride on their respective C atoms. The final cycle of full-matrix least-squares refinement on F^2 was based on 7,134 reflections and 425 variable parameters and converged. Cambridge Crystallographic Data Centre deposition number: 894788

Crystals of **3.3** suitable for X-ray diffraction were grown from a mixture of diethyl ether and *n*-hexane. All measurements were made on a Bruker SMART CCD APEX II diffractometer[32] using a fine-focus sealed-tube graphite monochromator Cu K_α source (λ = 1.54178 Å). Of the 21,117 reflections that were collected, 7,059 were unique (R_{int} = 0.049); equivalent reflections were merged. Data were collected and integrated using the Bruker SAINT software package.[33] Data were corrected for absorption effects using a multi-scan technique (SADABS)[34] and numerical face-indexing with max and min transmission coefficients of 0.158 and 0.054, respectively. The structure was solved using SHELXTL.[35] All non-hydrogen atoms were refined anisotropically. All hydrogen atoms were found in electron-density difference maps, but placed in idealized positions and allowed to ride on their respective C atoms. The final cycle of full-matrix least-squares refinement on F^2 was based on 7,059 reflections and 424 variable parameters and converged. Cambridge Crystallographic Data Centre deposition number: 894789

Crystals of **3.4** suitable for X-ray diffraction were grown by slow evaporation of a toluene solution of the compound. All measurements were made on a Bruker SMART CCD APEX II diffractometer[32] using a fine-focus sealed-tube graphite monochromator Cu K_α source (λ = 1.54178 Å). Of the 56,108 reflections that were collected, 11,178 were unique (R_{int} = 0.043); equivalent reflections were merged. Data were collected and integrated using the Bruker SAINT software package.[33] Data were corrected for absorption effects using a multi-scan technique (SADABS)[34] and numerical face-indexing with max and min transmission coefficients of 0.450 and 0.116, respectively. The structure was solved using SHELXTL.[35] All non-hydrogen atoms were refined anisotropically. All hydrogen atoms were found in electron-density difference maps, but placed in idealized positions and allowed to ride on their respective C atoms. The final cycle

of full-matrix least-squares refinement on F^2 was based on 11,178 reflections and 724 variable parameters and converged. Cambridge Crystallographic Data Centre deposition number: 894790

Crystals of **3.5** suitable for X-ray diffraction were grown by slow evaporation of a toluene solution of the compound. All measurements were made on a Bruker SMART CCD APEX II diffractometer[32] using a fine-focus sealed-tube graphite monochromator Cu K_α source (λ = 1.54178 Å). Of the 24,900 reflections that were collected, 3,251 were unique (R_{int} = 0.046); equivalent reflections were merged. Data were collected and integrated using the Bruker SAINT software package.[33] Data were corrected for absorption effects using a multi-scan technique (SADABS)[34] and numerical face-indexing with max and min transmission coefficients of 0.393 and 0.160, respectively. The structure was solved using SHELXTL.[35] All non-hydrogen atoms were refined anisotropically. All hydrogen atoms were found in electron-density difference maps, but placed in idealized positions and allowed to ride on their respective C atoms. The final cycle of full-matrix least-squares refinement on F^2 was based on 3,251 reflections and 195 variable parameters and converged. Cambridge Crystallographic Data Centre deposition number: 894791

3.3.7 DFT Calculations

All density functional calculations were performed using Jaguar.[36] Geometries were optimized, orbitals were calculated, and energies were determined all at the B3LYP/6-31G** level. We report final energies, orbital energies, and final geometries for $Co_6Se_8(PMe_3)_5L$ and $Co_6Se_8(PMe_3)_4\mathbf{L}_2$ for **L** = dimethyl-4-thiomethylphenylphosphine (**L3.2**), dimethyl-3-thiomethylphenylphosphine (**L3.3**), and diethyl-4'-thiomethyl-4-stilbenylphosphine (**L3.4**) (Figure B.13).

3.4 Conclusions

Quantum dots can act as reservoirs of electrical carriers or electronic excitations but this is valuable only to the extent that the charge or excitation can be removed from the cluster. In this study, we demonstrate a method to make contact and extract charge from one simple prototype. These results thus provide design rules for the preparation of structurally and electronically

discrete molecule scale quantum dots that reliably connect to nanoscale electrodes in a selective, well understood, and controllable fashion. Our work paves the way to incorporating these molecular-electronic elements into circuits. We anticipate that this approach will be widely applicable to other quantum dot systems, thereby enabling a multitude of studies including the extraction of charges from multiple exciton states and extraction of hot carriers.

3.5 References

[1] M. G. Bawendi, M. L. Steigerwald, L. E. Brus, *Annu. Rev. Phys. Chem.* **1990**, *41*, 477-496.

[2] P. A. Alivisatos, *Science* **1996**, *271* 933-937.

[3] D. V. Talapin, J.-S. Lee, M. V. Kovalenko, E. V. Shevchenko, *Chem. Rev.* **2010**, *110,* 389-458.

[4] M. Yuan, B. Ülgüt, M. McGuire, K. Takada, F. J. DiSalvo, S. Lee, H. Abruña, *Chem. Mater.* **2006**, *18*, 4296-4306.

[5] D. L. Klein, R. Roth, A. K. L Lim, P. A. Alivisatos, P. L. McEuen, *Nature* **1997**, *389*, 699-701.

[6] M.-H. Jo, *Nano Lett.* **2006**, *6,* 2014-2020.

[7] D. I. Gittins, D. Bethell, D. J. Schiffrin, R. J. Nichols, *Nature,* **2000**, *408*, 67-69.

[8] B. M. Boardman, J. R. Widawsky, Y. S. Park, C. L. Schenck, L. Venkataraman, M. L. Steigerwald, C. Nuckolls, *J. Am. Chem. Soc*. **2011***, 133*, 8455-8457.

[9] W. A. Tisdale, *Science* **2010**, *328*, 1543-1547.

[10] J. B. Sambur, T. Novet, B. A. Parkinson, *Science* **2010**, *330*, 63-66.

[11] A. J. Nozik, *Inorg. Chem.* **2005**, *44*, 6893-6899.

[12] D. V. Talapin, C. B. Murray, *Science* **2005**, *310*, 86-89.

[13] I. Robel, V. Subramanian, M. Kuno, P. V. Kamat, *J. Am. Chem. Soc.* **2006**, *128*, 2385-2393.

[14] Geyer, S. V. Porter, J. E. Halpert, T. S. Mentzel, M. A. Kastner, M. G. Bawendi, *Phys. Rev. B* **2010**, *82*, 155201.

[15] Y. Liu, M. Gibbs, J. Puthussery, S. Gaik, R. Ihly, H. W. Hillhouse, M. Law, *Nano Lett.* **2010**, *10*, 1960-1969.

[16] A. T. Fafarman, W.-k. Koh, B. T. Diroll, D. K. Kim, D.-K. Ko, S. J. Oh, X. Ye, V. Doan-Nguyen, M. R. Crump, D. C. Reifsnyder, C. B. Murray, C. R. Kagan, *J. Am. Chem. Soc.* **2011**, *133*, 15753-15761.

[17] T. P. Osedach, N. Zhao, T. L. Andrew, P. R. Brown, D. D. Wanger, D. B. Strasfeld, L.-Y. Change, M. G. Bawendi, V. Bulovic, *ACS Nano* **2012**, *6*, 3121-3127.

[18] S. M. Stuczynski, Y. U. Kwon, M. L. Steigerwald, *J. Organomet. Chem.* **1993**, *449*, 167-172

[19] B. Q. Xu, N. J. J. Tao, *Science* **2003**, *301*, 1221-1223.

[20] A. Nitzan, M. A. Ratner, *Science* **2003**, *300*, 1384-1389

[21] M. Kamenetska. M. Koentopp, A. C. Whalley, Y. S. Pakr, M. L. Steigerwald, C. Nuckolls, M. S. Hybertsen, L. Venkataraman, *Phys. Rev. Lett.* **2009**, *102*, 126803.

[22] W. Maneeprakorn, M. A. Malik, P. O'Brien, *J. Mater. Chem.* **2010**, *20*, 2329-2335.

[23] M. L. Steigerwald, *Polyhedron* **1994**, *13*, 1245-1252.

[24] M. L. Steigerwald, T. Siegrist, S. M. Stuczynski, *Inorg. Chem.* **1991**, *30,* 4940-4945.

[25] Y. S. Park, A. C. Whalley, M. Kamenetska, M. L. Steigerwald, M.S. Hybertsen, C. Nuckolls, L. Venkataraman, *J. Am. Chem. Soc.* **2007**, *129*, 15768-15769

[26] J. S. Meisner, M. Kamenetska, M. Krikorian, M. L. Steigerwald, L. Venkataraman, C. Nuckolls, *Nano Lett.* **2011,** *11*, 1575-1579.

[27] S.-H. Ke, W. Yang, H. U. Baranger, *Nano Lett.* **2008**, *8,* 3257-3261.

[28] D. M. Cardamone, C. A. Stafford, S. Mazumdar, *Nano Lett.* **2006**, *6*, 2422-2426.

[29] S. V. Aradhya, J. S. Meisner, M. Krikorian, S. Ahn, R. Parameswaran, M. L. Steigerwald, C. Nuckolls, L. Venkataraman, *Nano Lett.* **2012**, *12,* 1643-1647.

[30] C. Xue, F.-T. Luo, *J. Org. Chem.* **2003**, *68*, 4417–4421.

[31] L. Venkataraman, J. E. Klare, I.W. Tam, C. Nuckolls, M.S. Hybertsen, M.L. Steigerwald, *Nano Lett.* **2008**, *6*, 458-462.

[32] Bruker. *APEX2*. Version 2.0-2. Bruker AXS Inc., Madison, Wisconsin, USA **2006**.

[33] Bruker. *SAINT*. Version 7.23 A. Bruker AXS Inc., Madison, Wisconsin, USA **2005**.

[34] G. M. Sheldrick, *SADABS*. Version 2. University of Göttingen, Germany **2001**.

[35] G. M. Sheldrick, A short history of SHELX. *Acta Cryst.* **2008**, *A64*, 112–122.

[36] Schrodinger, *Jaguar*. Version 7.8. Schrodinger LLC. New York, NY, USA **2010**.

Chapter 4. Investigating the Relationship Between Single Molecule Conductance and Thin Film Conductance of Atomically Defined Quantum Dots

4.1 Introduction

QDs are promising electronic materials due to their quantum confinement, solubility, and interesting magnetic, electronic, and chromophoric properties.[1-5] In particular, we have been interested in atomically defined QDs that offer additional advantages of monodispersity, structural control, and x-ray crystallographic structural characterization.[6-7] These atomically defined QDs are composed of a metal chalcogenide core surrounded by an organic ligand shell that serves to prevent formation of bulk metal chalcogenide solids and by the same mechanism creates an environment for quantum confinement within the core. However, by nature these organic ligand shells are often insulating and inhibit communication between metal centers, thus hindering the application of these atomically defined QDs as electronic materials.

We recently investigated whether conductance could occur through the organic shell and whether we could design ligands that, while preserving QD properties of quantum confinement, could also provide a conduction pathway.[8,9] Using a scanning tunneling microscope based break-junction (STM-BJ) technique, we measured the single molecule conductance of atomically defined QDs. These results show that with insulating alkyl phosphine ligands, the conductance pathway occurs from gold electrodes to chalcogenide atoms in the metal core and do not involve the phosphine ligands. Increasing the bulk of the alkyl phosphine prevents electrode-QD core interactions, thus shutting down the conductance pathway. However, aromatic phosphine ligands decorated with aurophilic thiomethyl groups in the *para* position (Figure 4.1, **L4.1**) provide a pathway through the phosphine ligand to the cluster core (Figure 4.1, **4.1**). When the thiomethyl groups are installed in the *meta* position (Figure 4.1, **L4.2**), the conductance pathway through the cluster (Figure 4.1, **4.2**) is shut down. Calculations show that the thiomethyl groups in the *para* position electronically couple to the cluster core, while those in the *meta* position do not. This electronic coupling provides a pathway for delocalization of electrons from one ligand through the cluster core to other ligands. Even more exciting, these aromatic phosphine ligands do not impact the electronics of the cluster core. Thus, conductance can be switched on or off by ligand design,

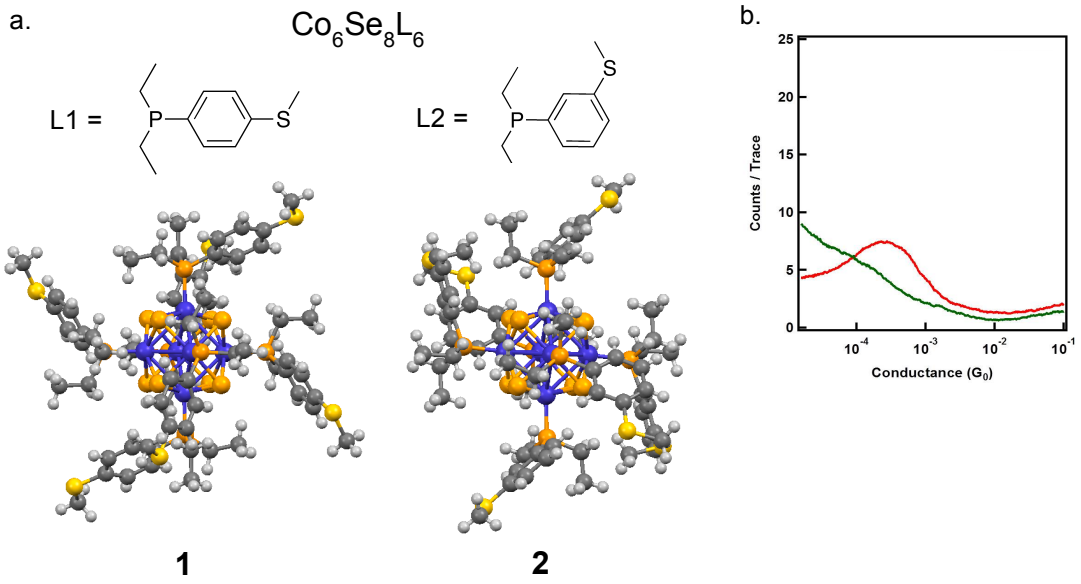

Figure 4.1 a) Molecular structure of **4.1**, **4.2**, **L4.1**, and **L4.2**. Carbon, gray; cobalt, blue; hydrogen, light gray; phosphorus, orange; selenium, green; sulfur, yellow. b) Logarithm-binned conductance histograms constructed using over 5000 traces for cluster **4.1** (red curve) and **4.2** (green curve).

with the position of the thiomethyl group playing an important role in determining if a conductance pathway is present.

While single molecule conductance measurements provide previously inaccessible insight into molecular conductance and conductance design rules,[10-15] it is often difficult to determine how much of this insight is transferrable to thin film devices. Single molecule conductance depends solely on the chemical structure and orientation of the molecule within the junction. Considering conductance through molecules within a thin film device adds many degrees of complexity. Thin film conductance is controlled by variables such as morphology and interaction of the thin film molecules with other molecules, with the substrate, and with the electrodes. In this chapter, we explore the thin film conductance of clusters **4.1** and **4.2** and try to understand the mechanism of conductance through insight gained from single molecule conductance measurements. In addition, while monodisperse quantum dots have been recently been investigated as thin film conducting materials,[16-19] thin films of atomically defined quantum dots have been largely unexplored. To the author's knowledge, this is the first report of an atomically defined quantum dot conductive thin film.

4.2 Results and Discussion

Due to the extreme air sensitivity of **4.1**, all device fabrication and experiments were performed inside of a glove box, or in an inert atmosphere. Thin films of clusters **4.1** and **4.2** were generated on silicon dioxide (SiO_2) substrates with pre-patterned gold electrodes. Electrodes were patterned such that several devices were made on a single substrate with a fixed width of 50 μm and channel lengths varying from 3 μm to 30 μm (Figure 4.2a,b). First, a series of spin-cast films were made from a 10 mg/mL solution of **4.1** or **4.2** in toluene. Thin film devices were measured at room temperature, where conductance was observed in thin films of **4.1** but not for thin films of **4.2** (Figure 4.2c). It was remarkable to us that the thin film conductance trend matched observations from STM-BJ single molecule conductance data.

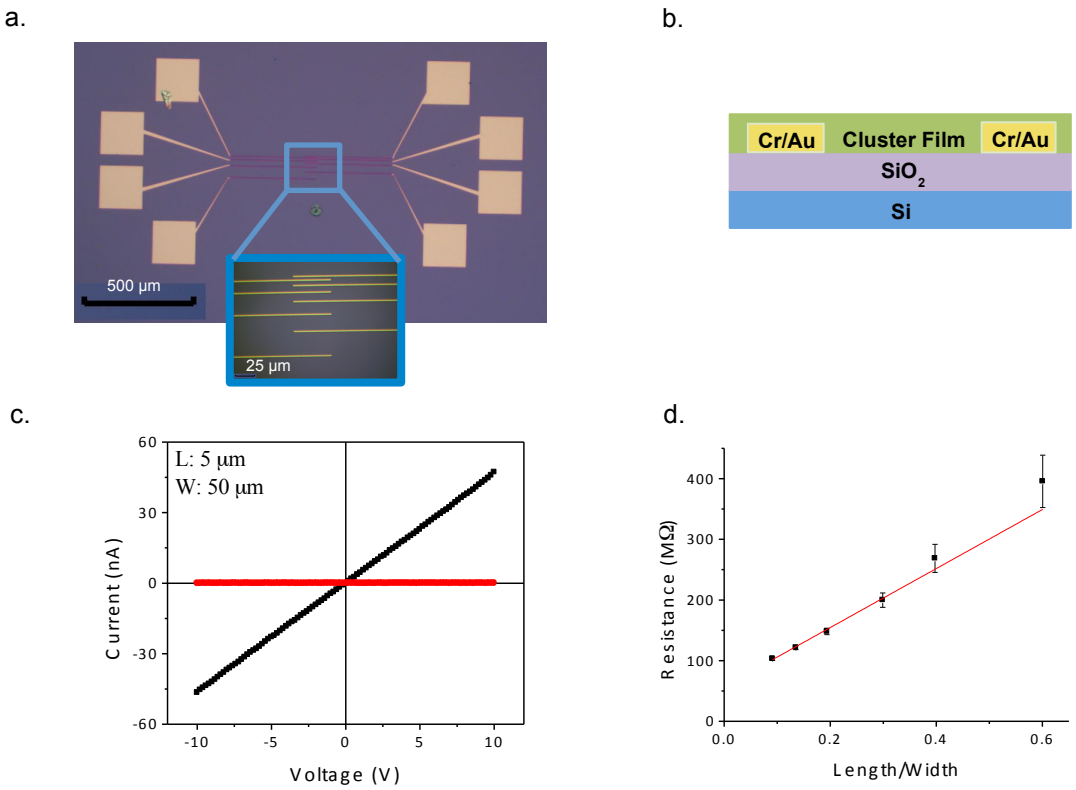

Figure 4.2. a) Optical microscope image of pre-patterned gold electrodes on SiO_2. Electrodes are enlarged in the center to show lengths of devices from 3 μm to 30 μm. b) Device architecture. c) I-V curves for thin film devices of **4.1** (black) and **4.2** (red) b) Plot of resistance of **4.1** versus length/width.

Films of **4.1** gave sheet resistance proportional to channel length (Figure 4.2d). Contact and sheet resistance were determined from the slope of a plot of the sheet resistance of the film versus the ratio of channel length to width. Average sheet resistance was 470 MΩ (Table C.1). Film thickness, determined by Atomic Force microscopy (AFM) to be ~20 nm, was used to calculate an average resistivity of 1 kΩ·cm and conductivity of 0.7 mS/cm, over five devices (Table C.1). These values are well within the range of other semiconducting materials, including CdSe nanocrystal thin films.[18] In contrast, the sheet resistance for thin films of cluster **4.2** was out of the range of measurement, with a value greater than 100 GΩ/□.

Absorbance of the spin coated thin films of **4.1** and **4.2** on glass slides was measured using UV-vis spectroscopy (Figure C.12). Both spectra showed three transitions at the same wavelengths as the clusters in solution. This indicates that the clusters remain intact within the film. However, there is significant broadening observed for the **4.1** films relative to those of **4.2**. Broadening of the absorption spectrum indicates charge delocalization throughout the film. This data matches well with the fact that **4.1** thin films are conducting while **4.2** thin films are insulating.

During our investigation of the single molecule conductance of **4.1** and **4.2**, a significant difference in air sensitivity between **4.1**, which is extremely sensitive to even small amounts of oxygen, and **4.2**, which is air stable, was observed. Calculations suggested that the difference in air sensitivity is due to the fact that the external thiomethyl groups in the *para* position can act as a conduit for cluster core electrons to be accessed. Based on this knowledge, we hypothesize that at very low concentrations, oxygen acts as a dopant in thin films of **4.1**, but cannot access the core electrons of **4.2**. We believe that residual oxygen within the glovebox, at a level below 1 ppm, is enough to dope the cluster film.

In order to probe the similarities between the single molecule conductance characteristics and the thin film conductance we observed, an investigation of the film morphology was necessary. Optical microscopy of cluster **4.1** and **4.2** showed smooth films (Figure C.1, C.2) that were also observed by AFM measured surface topography (Figure 4.3a, b). The surface of cluster **4.1** films was extremely smooth with a roughness of only 0.3 nm, in contrast to the value of 1.6 nm for cluster **3** film.

For a better understanding of film crystallinity and packing, we used grazing incidence x-ray diffraction (GIXD) to study the spin cast thin films of **4.1** and **4.2**. Figure 4.3 shows the 2-D reciprocal (Q-space) diffraction patterns for cluster **4.1** (Fig. 4.3c) and cluster **4.2** (Fig. 4.3d,e). Cluster **4.1** is amorphous. In contrast, cluster **4.2** forms oriented, crystalline films on the SiO_2/Si substrate. In particular, we observe a weak ring at Q=0.52Å^{-1} with high intensity concentrated along the Q_z (Q_r=0, out-of-plane) direction. We also observe three peaks at Q_r=0.52Å^{-1} with Q_z values of 0.18, 0.36, and 0.71 Å^{-1}, respectively. We index the measured diffraction peaks and determine the crystallographic orientation(s) of the cluster **4.2** film based on reciprocal space diffraction patterns computed using the lattice parameters obtained from single crystal diffraction data. Figure 4.3d and 4.3e compares for different crystallographic orientations of the cluster **4.2** unit cell and compared to thin film data; best fits are obtained for the (100) (Figure 4.3d) and (010) directions (Figure 4.3e) oriented along the surface normal. The lowering of the thin film Q-

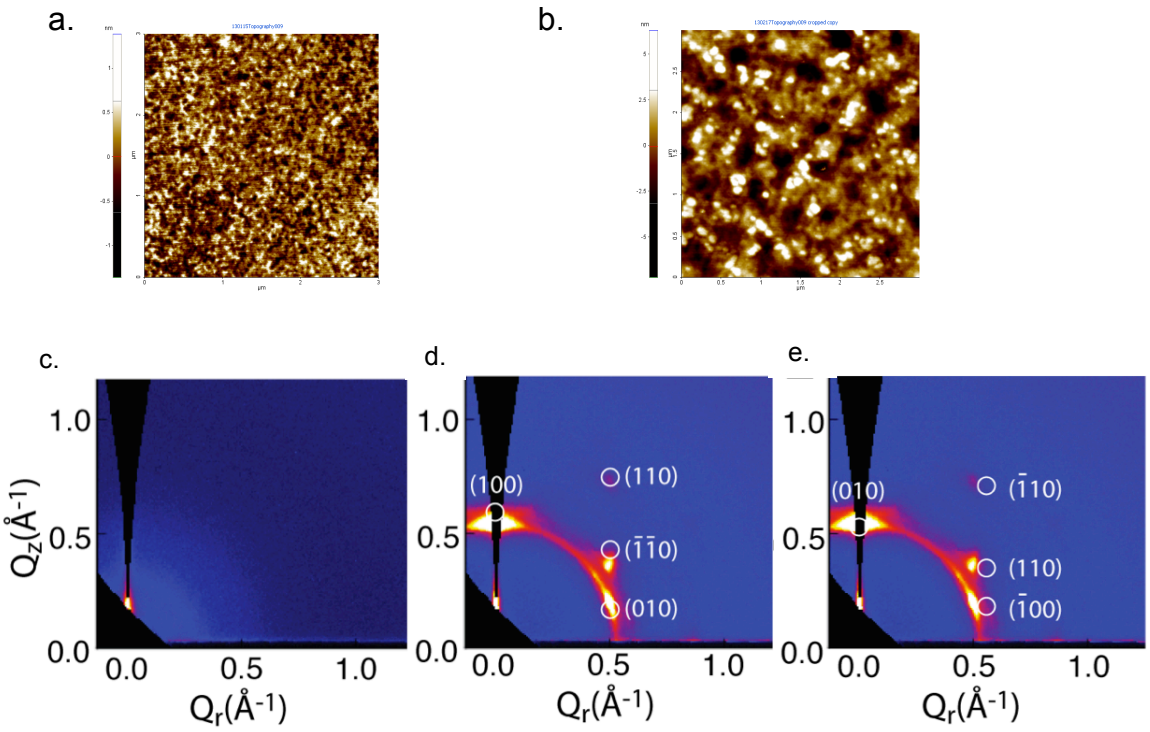

Figure 4.3. a) Atomic Force microscopy image of a thin film of **4.1.** b) Atomic Force microscopy image of a thin film of **4.2**. c.-e.) Two-dimensional reciprocal (Q-) space diffraction patterns for thin films of: **4.1** (c) and **4.2** (d,e), with 2-D patterns computed from lattice parameters obtained with single crystal measurements of **4.2** overlaid as white circles and peaks indexed for unit cell orientations with either the a-axis ((100), d) or b-axis ((010), e) oriented along the surface normal.

values of **4.2** along Q_r with the a-xis oriented out-of-plane (Fig. 4.3e) and along Q_r when the b-axis is out-of-plane relative to the single crystal data may be explained as due to a slight expansion of the unit cell in the plane of the substrate due to the presence of solvent molecules. The fit results, together with the weak ring at Q=0.53 $Å^{-}$ and a series of sharp, highly textured rings at Q values > 1.5 $Å^{-1}$ (Figure C.5), suggests that two distinct crystallographic orientations relative to the substrate coexist in thin films of **4.2**, with the a-axis (100) and b-axis (010) respectively, oriented along the surface normal.

It is possible that the extreme difference in film crystallinity between **4.1** and **4.2** is the reason for the disparity in conductance of these films. However, we do not believe this is the case. Upon close inspection of the crystal structures of both **4.1** and **4.2**, it was observed that both clusters are spaced between 9 and 14 Å apart and have weak interactions between sulfurs on the periphery of neighboring clusters (4-5 Å).[9] If the mechanism of conductance was through a sulfur-sulfur interaction, it would be expected that a crystalline film would perform better than an amorphous film. Perhaps rather than morphology driving the film conductance, or lack thereof, we believe the proposed mechanism of conductance is responsible for the difference in morphology. Due to the extreme air sensitivity of **4.1**, it is expected that a small percentage of the clusters in the solution used for device fabrication are doped by oxygen. During device fabrication, the doped clusters act as impurities, and the interaction between doped and undoped clusters prevents the formation of crystalline films. In the case of **4.2**, the lack of doped clusters allows for pristine, crystalline films to be formed but prevents charge transport throughout the film.

Drop cast films of **4.1** and **4.2** were made from 20 mg/mL solutions of **4.1** or **4.2** in toluene. Solutions were dropped onto the same pre-patterned SiO_2 used for spin cast devices and left to dry slowly in a covered box within the glovebox. Films of **4.1** gave an average sheet resistance of 81 MΩ while those of **4.2** showed no measurable conductance (Table C.2). The sheet resistance of drop cast **4.1** is much lower than that of the spin cast films, most likely due to the difference in film thickness (170 nm for films of **4.1** and 420 nm for films of **4.2**). Calculation of resistivity using film thickness gave similar values for both spin cast and drop cast films. Both drop cast films, not surprisingly, appeared much thicker and rougher than their spin cast

counterparts by both optical microscopy and AFM (Figure C.3, C.4, C.13). Optical microscopy showed visible crystallinity in thin films of **4.2**, while **4.1** films were uneven and speckled (Figure C.3, C.4).

Thermal annealing of the spin cast and drop cast films led to an increase in conductance for **4.1** and no change in the insulating nature of **4.2** thin films (Figure C.6, C.7; Table C.3). Improvement in conductance of thin films with thermal annealing is generally contributed to better interactions between molecules within the film. It is interesting to note that thermal annealing had no impact on films of **4.2**. This suggests that conductance occurs due to a mechanism less dependent on morphology. However, further studies, such as GIXD, are necessary to explore the exact morphological changes that occur during annealing in this system.

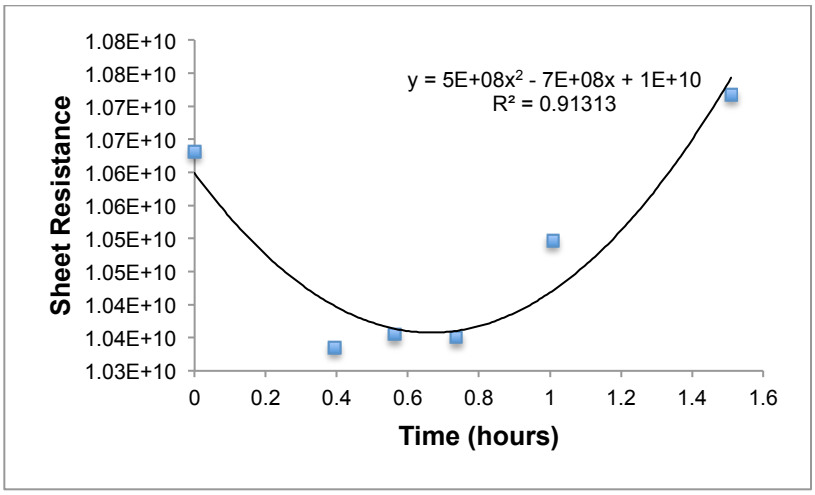

Figure 4.4. Short-term time dependence of spin cast films of **4.1**.

To test the proposed oxygen doping mechanism, we first monitored conductance of thin films of **4.1** over time. In the glovebox atmosphere with less than 1 ppm of oxygen, conductance increases after device fabrication for the first ~0.5 hours after which it begins to decrease at a slow rate (Figure 4.4, C.10). Devices of **4.1** remain conductive over >3 months, although the sheet resistance increases by at least an order of magnitude. Films that were annealed also showed an increase in sheet resistance over time. Other devices of **4.1** were exposed to atmospheric oxygen for 5 seconds, 30 seconds, and 10 minutes, with conductance

measurements taken after each exposure. After 5 seconds, conductance decreased by <5%. After 30 seconds, conductance was decreased by >70%. Exposure of the device to atmospheric oxygen for more than 2 minutes completely turned off conductance.

This data suggests that there is an optimal amount of doping that occurs within the first half hour of glovebox exposure. We suggest that oxygen is reduced, leaving behind a vacancy within the cluster core. An electron from a neighboring cluster can fill this vacancy, leaving behind a vacancy. This charge transport, either through hopping or tunneling, from one cluster to another allows for charges travel through the film. However, if doping levels exceed this optimal level, which happens over time within the glovebox or with short exposure to the atmosphere, the conductance decreases and eventually turns of. This over-oxidation leads to a surplus of vacancies, resulting in a lack of electrons available to move through the film. It is interesting to note that films of **4.2** left in atmosphere for > 2 months did not become conductive. This supports our hypothesis that **L4.2** is a highly insulating ligand that protects the core from oxidation via external dopants. A substrate surface control study using octyldecyltrichlorosilane-coated substrates verified that this doping effect is not from the substrate but solely from the atomosphere (Figure C.14).

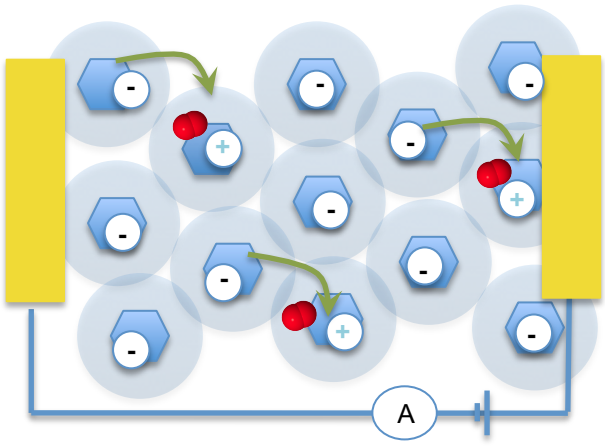

Figure 4.2. A cartoon of the proposed oxygen doping conductance mechanism. Blue hexagons indicate cluster cores. Light blue circles indicate organic ligand shell. Oxygen molecules shown in red. White circles indicate holes (+) and electrons (-). Green arrows demonstrate movement of electrons towards holes created by oxygen doping. Yellow rectangles represent gold electrodes.

This proposed oxygen doping mechanism of conductance is based on understanding thin film conductance at the molecular level. Single molecule conductance measurements demonstrated that the conjugation of the thiomethyl groups to the cluster core is what turned molecular conductance on or off, as well as impacting the kinetic access to core electrons. This kinetic access to core electrons translates into the conductance of the thin films. Thin films are often thought of as a collective material and are studied as such rather than focusing on the individual molecules that make up the film. Here, the difference in access to core electrons has a molecular origin, understood by the single molecule conductance results. The ease of access to the core electrons of **4.1**, but not **4.2**, results in a large difference in sensitivity to oxidation. This observation supports an oxygen doping mechanism for thin films of **4.1**, where core electrons are easily accessed by small amounts of oxygen, but not **4.2**, where core electrons are protected by the insulating ligands. Future work should include 4-point probe measurements of **4.1** thin films to further investigate the transport mechanism of the film, as well as a more detailed study of morphological differences. However, this system illustrates that lessons learned from single molecule conductance experiments can help to understand and perhaps eventually predict conductance of thin films.

4.3 Experimental

4.3.1 Synthesis

Materials were prepared according to the synthetic procedures outlined in chapter 3.

4.3.2 Substrate and Thin Film Preparation

Pre-patterned electrodes were fabricated using a Heidelber μPG 101 Laser Writer on a silicon substrate with 285 nm of thermally grown SiO_2. The source and drain electrodes were further thickened by evaporation of Cr/Au (1 nm/40 nm). Electrodes were patterned such that several devices were made on a single substrate with a fixed width of 50 μm and channel lengths varying from 3 μm to 30 μm (Figure 2a). A solution of 10 mg/mL of cluster in toluene was filtered through a 13mm syringe filter (0.45 μm, PVDF, Sterile, Fisherbrand) and then spin coated (SCS

G3-8 Spincoat Specialty Coating System) on top of the patterned substrate with a spin speed of 1200 rpm for one minute. Drop cast films were made by dropping a filtered solution of 20 mg/mL of cluster in toluene on a patterned substrate. Once the solution was dropped onto the substrate, the substrate was left in a covered box until dry (between 10 and 30 minutes).

4.3.3 Conductance Measurements

Conductance of the films was measured using an Agilent 4155C Semiconductor parameter analyzer and suss microtec EP4 probe station. Software used was I-CV lite system tools, Interactive characterization software, version 3.6.0 SP REL.

4.3.4 Atomic Force Microscopy

Non-contact atomic force microscopy (AFM) images were acquired at room temperature using a PSIA XE100. It should be noted that AFM was done under ambient conditions. Because of the air sensitivity of **4.1**, it is unknown how this significant oxygen exposure affected the morphology of the films. Measurements were made immediately upon removal from the glovebox to try and minimize this effect.

4.3.5 Optical Microscopy

Optical microscope images were obtained using a Nikon LV100 instrument with an Infinity1-3C camera. It should be noted that optical microscopy was done under ambient conditions. Because of the air sensitivity of **4.1**, it is unknown how this significant oxygen exposure affected the morphology of the films. Measurements were made immediately upon removal from the glovebox to try and minimize this effect.

4.3.6 Grazing Incidence X-Ray Diffraction (GIXD)

GIXD measurements were performed at the National Synchrotron Light Source (NSLS) of Brookhaven National Laboratory on beamline X-9 at a photon energy of 14.0 keV. The incident x-ray beam, k_{in}, has a grazing incidence angle with the sample surface. A Photonic Science WAXS

detector (pixel size of 0.11 mm) positioned a distance L from the sample, records the scattered beam, k_{out}. This is converted into an image of the reciprocal space (Q-space) with the scattering expressed as a function of the scattering vector $Q=k_{out}-k_{in}$. Here, the sample-to-detector distance L, calibrated with LaB_6 and AgBH polycrystalline standards, was 265 mm at beamline X9. An incident angle of 0.12° at which the signal from the film is optimized and that from the substrate is suppressed is shown here; a depth profile was also performed by varying the angle of the incident light and the sample surface from 0.07 to 0.20°. It should be noted that films of **4.1** and **4.2** were exposed to ambient atmosphere for under one minute. Because of the air sensitivity of **4.1**, it is unknown how this significant oxygen exposure affected the morphology of the films.

4.3.7 UV-vis Spectroscopy

Thin films of **4.1** or **4.2** were prepared on glass slides by spin coating (SCS G3-8 Spincoat Specialty Coating System) a solution of 10 mg/mL of cluster in toluene that had been filtered through a 13mm syringe filter (0.45 μm, PVDF, Sterile, Fisherbrand) with a spin speed of 1200 rpm for one minute. UV-vis spectra were recorded on a Shimadzu UV Spectrophotometer (UV-1800) that had been blanked with a clean glass slide. A film of **4.1** was recorded in air and another film was measured with exclusion of air by taping a second glass slide over the face of the film within the glovebox. The film of **4.2** was measured in air.

4.3.8 OTS Substrate and Thin Film Preparation

The 285 nm SiO_2 substrates were coated with a monolayer of octadecyltrichorosilane (OTS) by immersion in a toluene solution of OTS (5 mM) for 16 h at room temperature. Substrates were rinsed with chloroform, isopropyl alcohol and deionized water. The static contact angle (~108°) was measured on a Rame-Hart goniometer to confirm surface hydrophobicity of the OTS self-assembled monolayer (SAM). A 20 mg/mL solution of **4.1** or **4.2** was drop cast on top of the OTS coated substrate. Conductance measurements showed sheet resistance similar to that observed without OTS (Figure C.14).

4.4 Conclusion

The ability for atomically defined quantum dots to make conductive thin films was demonstrated. These films show conductivity values similar to those observed in monodisperse QD systems. An atomically defined quantum dot with a *para* thiomethyl substituted aromatic ligand gives conductive thin films, while *meta* substitution does not. This subtle change in substitution mimicked results from single molecule conductance measurements of the same molecules. Films of the two materials show different morphologies, with **4.1** giving an amorphous film and **4.2** giving a crystalline film. However thermal annealing, which increases the conductance of **4.1** while not impacting the insulating nature of **4.2** suggests that the disparity in conductance between these two films is not completely a result of morphological differences. A conductance mechanism based on doping of the **4.1** thin film with very low levels of oxygen is proposed. Preliminary data demonstrates that there is an optimal oxygen doping level.

4.5 Acknowledgements

The author would like to thank Jaeeun Yu for her assistance with device fabrication, measurement, and microscope work. Theanne Schiros should be recognized for performing the GIXD measurements and analysis. In addition, Xavier Roy and Ari Turkiewicz are recognized for their help with various parts of the synthesis.

4.6 References

[1] R. G. Chaudhuri, S. Paria, *Chem. Rev.* **2012**, *112*, 2373-2433.

[2] A. J. Nozik, M. C. Beard, J. M. Luther, M. Law, R. J. Ellingson, J. C. Johnson, *Chem. Rev.* **2010**, *110*, 6873-6890.

[3] M. G. Panthani, B. A. Korgel, *Annu. Rev. Chem. Biomol. Eng.* **2012**, *3*, 287-311.

[4] C. B. Murray, C. R. Kagan, M. G. Bawendi, *Annu. Rev. Mater. Sci.* **2000**, *30*, 545-610.

[5] M. G. Bawendi, M. L. Steigerwald, L. E. Brus *Annu. Rev. Phys Chem.* **1990**, *41*, 477-496.

[6] M. W. Degroot, J. F. Corrigan, *Compr. Coord. Chem. II.* **2004**, *7*, 57-123.

[7] S. M. Stuczynski, Y.-U. Kwon, M. L. Steigerwald, *J. Organomet. Chem* **1993**, *449*, 167-172.

[8] B. M. Boardman, J. R. Widawsky, Y. S. Park, C. L. Schenck, L. Venkataraman, M. L. Steigerwald, C. Nuckolls, *J. Am. Chem.Soc.* **2011**, *113*, 8455-8457.

[9] X. Roy, C. L. Schenck, S. Ahn, R. A. Lalancette, L. Venkataraman, C. Nuckolls, M. L. Steigerwald, *Angew. Chem. Int. Ed.* **2012**, *51*, 12473-12476.

[10] F. Chen, J. Hihath, Z. Huang, X. Li, J. J. Tao, *Annu. Rev. Phys. Chem.* **2007**, *58*, 535-564.

[11] Y. Selzer, D. L. Allara, *Annu. Rev. Phys. Chem.* **2006**, *57*, 593-623.

[12] R. L. McCreery, *Chem. Mater.* **2004**, *16*, 4477-4496.

[13] A. Nitzan, M. A. Ratner, *Science*, **2003**, *300*, 1384-1389.

[14] C. Joachim, J. K. Gimzewski, A. Aviram, *Nature*, **2000**, *408*, 541-548.

[15] S. V. Aradhya, L. Venkataraman, *Nature Nano.* **2013**, *8*, 399-410.

[16] M. Drndić, M. V. Jarosz, N. Y. Morgan, M. A. Kastner, M. G. Bawendi, *J. Appl. Phys.* **2002**, *92*, 7498-7503.

[17] N. Y. Morgan, C. A. Leatherdale, M. Drndić, M. V. Jarosz, M. A. Kastner, M. Bawendi, *Phys. Rev. B.* **2002**, *66*, 075339.

[18] D. Yu, C. Wang, P. Guyot-Sionnest, *Science.* **2003**, *300*, 1277-1280.

[19] S. Geyer, V. J. Porter, J. E. Halpert, T. S. Mentzel, M. A. Kastner, M. G. Bawendi, *Phys Rev. B.* **2010**, *82*, 155201.

Chapter 5. Expanding the Family of Nickel Telluride Molecular Clusters

5.1 Introduction

There has been little reported on the magnetic and electrical properties of solid-state nickel telluride. That which has been reported suggests that solid-state nickel telluride is a poor metallic conductor with paramagnetic or weak antiferromagnetic properties.[1-3] However, molecular clusters of nickel telluride have proven to be atomically precise, soluble, electron-rich materials with interesting magnetic properties.[4-10] More recently, metal chalcogenide molecular clusters have been investigated as nanoscale atomic building blocks for novel solid-state materials.[11] The properties of this class of solid-state materials are strongly dependent on the composition of the respective molecular cluster building blocks. For example, the solid state material prepared from $Ni_9Te_6(PEt_3)_8$ (**5.1**) co-crystallized with C_{60} fullerene demonstrated vastly different magnetic ordering at low temperatures when compared with the individual components or with that of other assembled materials, $Co_6Se_8PEt_3 \bullet 2C_{60}$ and $Cr_6Te_8PEt_3 \bullet 2C_{60}$.

Currently, only a few nickel telluride molecular clusters are known (Figure 1, **5.1**-**5.3**).[5,8] These molecules have been synthesized by reaction of bis(cyclooctadiene)nickel $Ni(COD)_2$ with a phosphine telluride. It was demonstrated that by adjusting the stoichiometry, the size of the resulting cluster could be controlled.[10] Using a 2:1 ratio of $Ni(COD)_2$ to triethylphosphine telluride (PEt_3Te), **5.1** was isolated.[10] Cluster **5.1** was transformed into a larger $Ni_{20}Te_{18}(PEt_3)_{12}$ (**5.2**) by adding three additional equivalents of PEt_3Te to a solution of **5.1** and PEt_3.[10] In addition, it was shown that **5.2** could be accessed directly by a 1:1 reaction of $Ni(COD)_2$ and PEt_3Te.[10] In this study, only triethylphosphine ligands were utilized. Another reported cluster is $Ni_3Te_2dppm_3$ (**5.3**, dppm = bis(diphenylphosphino)methane), which was isolated from a 1:1 reaction of $Ni(COD)_2$ with dppm, followed by addition of 2 equivalents of tri-n-propylphosphine telluride.[8]

We became interested in expanding this small library of available nickel telluride clusters because of the exciting properties observed for the clusters and most recently their assembled co-crystalline solid-state materials. In order to explore the potential of the cluster-assembled materials approach, development of synthetic strategies for diversifying the family of nickel

telluride nanoscale atomic building blocks is necessary. In addition, it is of interest to try and understand why different cluster structures form under certain synthetic conditions in the hopes of eventually predicting and designing cluster cores. In this chapter, we explore the impact of ligand structure on cluster formation. We also find that ligand exchange provides access to a cluster not synthesized directly from reaction of $Ni(COD)_2$ with phosphine telluride. Structural characterization and preliminary cluster properties are discussed.

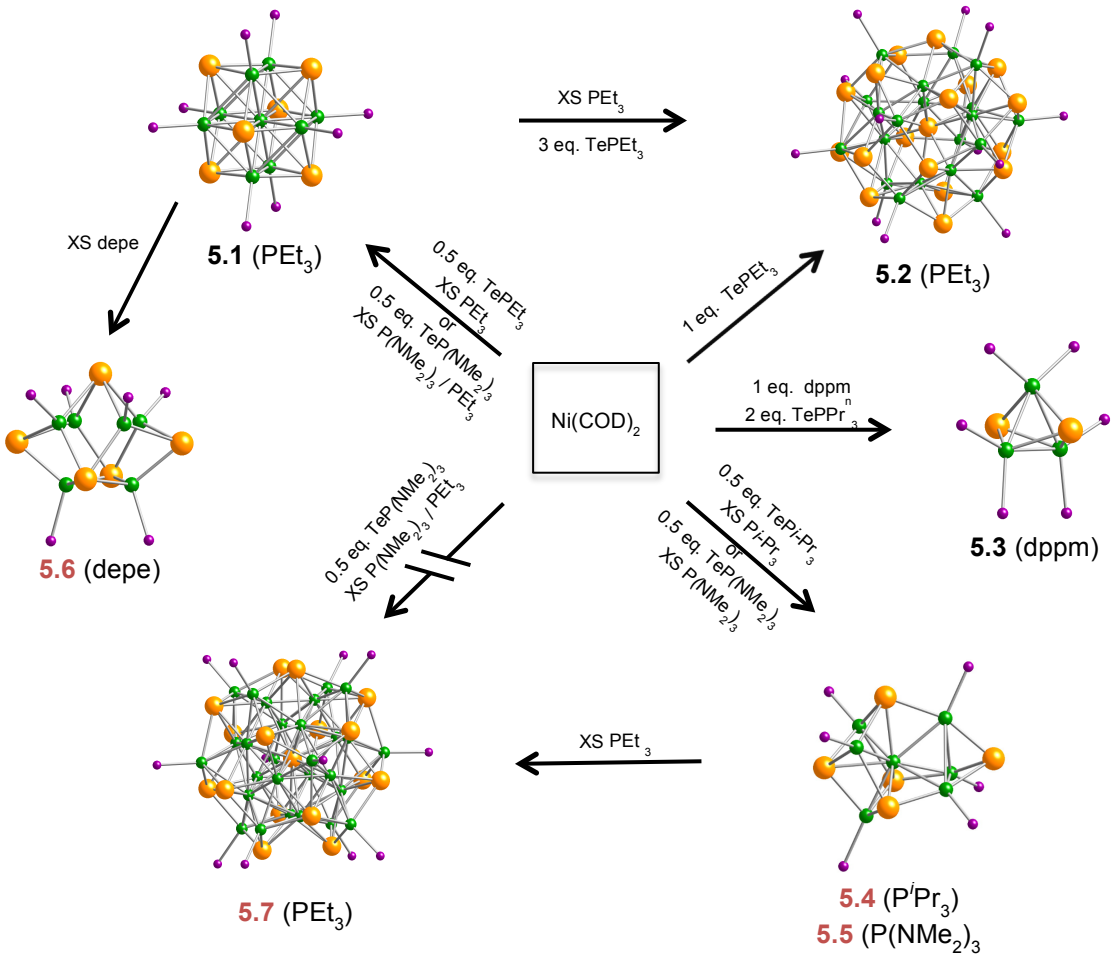

Figure 5.1. a) A schematic of the nickel telluride molecular clusters that result under different synthetic conditions. Atoms: nickel is green, tellurium is orange, phosphorus is purple. Phosphine substitution was omitted for clarity, however is described in parentheses below the molecule. Double slashed arrow indicates that reaction does not result in that cluster. Excess is represented as "XS." **5.1, 5.2**, and **5.3** have been previously reported. The labels of clusters reported for the first time in this chapter are shown in red.

5.2 Results and Discussion

Our initial investigation involved probing the effect of sterically bulky ligands on cluster formation. We chose triisopropylphosphine (P^iPr_3) as a capping ligand because it is electronically similar to PEt_3, but is much more sterically bulky. Previous syntheses of nickel telluride clusters with triethylphosphine involved reaction of phosphine telluride with $Ni(COD)_2$.[5,8,10] Incorporation of P^iPr_3 was achieved using the same method, although in our case producing a completely different cluster. Elemental tellurium was stirred with a large excess of P^iPr_3 in hexanes at room temperature to give a yellow solution. This solution was characterized by NMR spectroscopy to be the expected phosphine telluride, and was henceforth used *in situ*. Two equivalents of $Ni(COD)_2$, with respect to tellurium, were added directly to the phosphine telluride solution to give a dark brown, homogeneous solution. After stirring at room temperature for 20 minutes, the solution was filtered and left to crystallize overnight from the reaction mixture, giving dark brown-black crystals in 6 % yield.

The structure of this crystalline product was determined by single crystal X-ray diffraction (SCXRD) and confirmed by NMR, IR, and elemental analysis. Instead of forming the previously reported $Ni_9Te_6(PEt_3)_8$ (**5.1**) molecular cluster, the resulting structure was a smaller $Ni_7Te_5(P^iPr_3)_6$ (**5.4,** Figure 5.1). This result indicates that more sterically bulky ligands induce smaller cluster formation, a hypothesis that has previously been put forth.[12] The general bonding scheme of **5.2** is similar to that of other nickel telluride molecular clusters, with an outer covering of phosphine ligands each attached to a surface nickel atom and tellurium atoms bridging nickel atoms. A summary of select bond lengths can be found in Table 5.1. At first glance, one notices that this structure is quite asymmetric around the central nickel atom (Ni1). Ni1 is bonded to six outer nickel atoms in a distorted octahedron. Three of these outer six nickel atoms (Ni2) are 2.43 Å from the central nickel while the other three (Ni3) are at a distance of 2.66 Å. The Ni3 atoms are 2.89 Å apart from each other and form a triangle that is capped by a tellurium atom (Te1). The Ni2 atoms are not bonded to each other, with a interatomic distance of 3.583 Å, but are instead

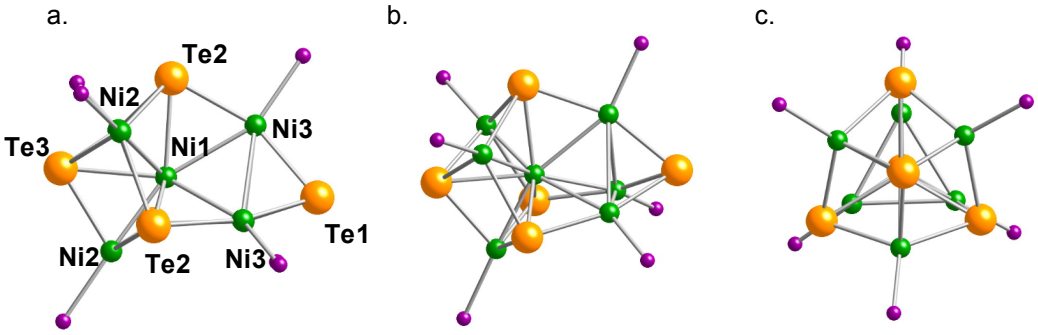

Figure 5.2. $Ni_7Te_5(L)_6$ cluster core, where L = P^iPr_3 for **5.4** or $P(NMe_2)_3$ for **5.5**. a) side view of cluster b) rotated side view of cluster c) front view of cluster.

Table 5.1. Select Distances (Å) found for **5.4.**

Ni1-Ni3	2.660(3)	Ni2-Ni2	3.582
Ni1-Ni2	2.428(3)	Ni2-Te2	2.552(3) 2.542(3)
Ni1-Te2	2.5197(6) 2.5182(9)	Ni3-Te1	2.430(2)
Ni1-Te3	2.728(3)	Ni3-Ni3	2.892(3)
Ni2-Te3	2.529(2)	Ni3-Te2	2.447(2)

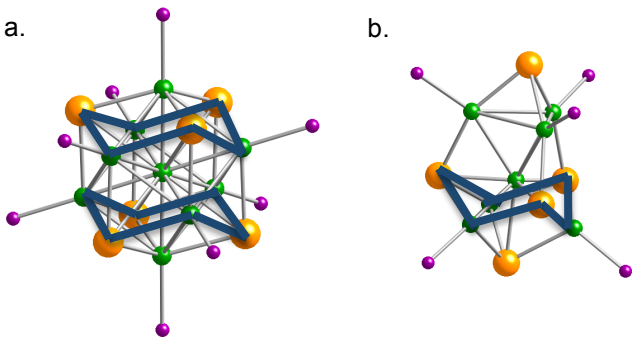

Figure 5.3. Comparison of the structure of **5.1** and **5.4**. Blue lines highlight the alternating Ni-Te chair structure within the cluster cores.

bonded to three tellurium atoms (Te2). These Te2 atoms are also coordinated to the central Ni1. Looking down the C_3 axis of the molecule, a six-membered ring in a chair conformation is formed by alternating Ni2 and Te2 atoms. The Ni2 face of this ring is capped by an additional tellurium (Te3). This six-membered ring centered on the central Ni1 is reminiscent of a fragment of the cubic cluster **5.1**. Figure 5.3 highlights this common structural motif within structures of **5.1** and **5.4**. This feature has previously been related to the NiAs structure of the δ-phase NiTe extended solid system.[6,13] It seems that the bulky P^iPr_3 ligands around the cluster core can only accommodate one of these structural motifs. The other half of the molecule must be smaller to make room for the bulkier ligands.

Changing the steric bulk of the phosphine ligand clearly has a large impact on the size and structure of the resulting cluster core. We then wondered whether changing the electronics of the ligands would have as large of an impact. We became interested in aminophosphine ligands, which have recently enjoyed much investigation in fields such as catalysis and coordination chemistry.[14-18] Aminophosphines are particularly attractive ligands because they (1) contain between one and three lone pairs, depending on how many amino groups are appended to the phosphine, (2) are easily synthesized and often commercially available, (3) are diverse in structure and reactivity, and (4) are easily modified through transamination reactions, opening the possibility of linked phosphines with diamines.[18] While aminophosphine chalcogenides have been studied in detail,[17-19] to the authors' knowledge there has been no report of metal chalcogenide clusters with aminophosphine ligands.

We chose to incorporate tris(dimethylamino)phosphine ($P(NMe_2)_3$) into a nickel telluride cluster because it is a structural relative of P*i*-Pr_3 and is very sterically similar. Using a synthetic procedure and stoichiometry analogous to that used for P*i*-Pr_3, elemental tellurium and $P(NMe_2)_3$ were stirred at room temperature in heptane. The resulting phosphine telluride solution was used *in situ*, with addition of $Ni(COD)_2$ causing an immediate color change to dark brown. Crystallization at room temperature gave shiny dark crystals in 23% yield. SCXRD was used to determine that the product of this reaction was isostructural to that of **5.4**, giving

$Ni_7Te_5(P(NMe_2)_3)_6$ (**5.5**). This indicates that the sterics of the phosphine dictate the structure of the resulting cluster more so than the electronics of the phosphine.

While the cluster structure of **5.4** and **5.5** are the same, they show significant differences in the crystal packing. This indicates that, while sterics dictate the cluster structure, ligand electronics dictate the intermolecular packing, presumably due to a difference in intermolecular interactions. Cluster **5.4** packs as a rhombohedral lattice system while cluster **5.5** is monoclinic. Looking at the ab plane of the crystal structure of **5.4**, the clusters are all oriented along their individual C_3 axes (Figure 5.4a). Within this packing, a hexagonal structure is apparent, where the

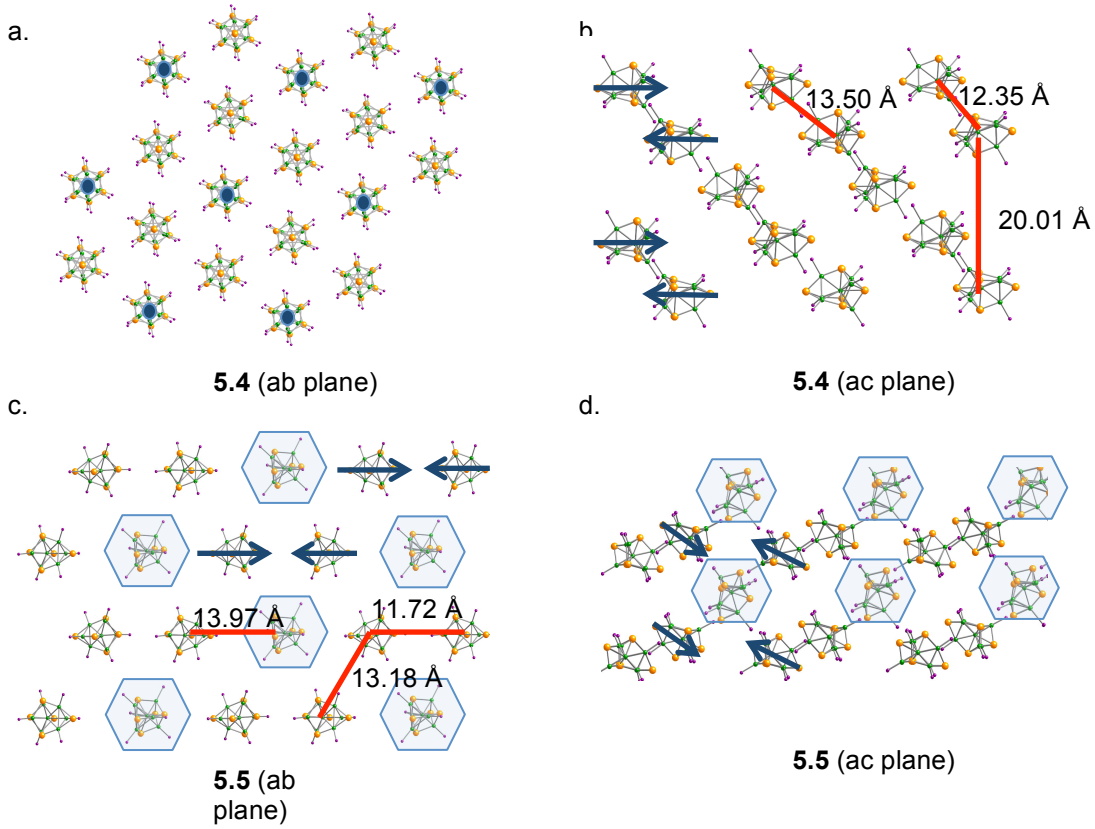

Figure 5.4. Crystal packing of **5.4** and **5.5**. Crystal packing of a) ab plane of **5.4** b) ac plane of **5.4** c) ab plane of **5.5** d) ac plane of **5.5**. Blue arrows in (b) point from Te1 to Te3. Blue dots in (a) indicate the head of the arrows. Blue hexagons in (c) and (d) are meant to highlight the point of disorder within the crystal structure. Red arrows indicate intermolecular distances from Ni1-Ni1.

clusters that make up the hexagonal packing are pointing in one direction, while the clusters in the center of the hexagon are pointed in the opposite direction (Figure 5.4a, blue dots). This ordering is apparent when viewing the crystal packing in the ac-plane, where layers are alternating in the cluster direction (Figure 5.4b, blue arrows). The “Te1” end of the clusters in a layer are pointing towards the “Te1” end of the clusters in the neighboring layer, and visa versa. Within each layer, clusters are spaced very far apart (20.01 Å, Ni1-Ni1) (Figure 5.4b, red lines). Clusters in neighboring layers are much closer together (12.35 or 13.50 Å, Ni1-Ni1), and the spacing is dependent on whether it is at a Te1-Te1 interface or the Te3-Te3 interface, respectively (Figure 5.4b, red lines).

Looking at the ab plane of cluster **5.5**, hexagonal-type packing is again apparent. However, the orientation of the molecules is quite different from that of **5.4**. The six molecules making up the hexagonal array appeared to be paired up. Blue arrows in Figure 5.4 highlight that the molecules within each pair have the Te1 end of each molecule pointing away. The spacing between the two molecules within the pair (11.72 Å) is much smaller than the distances between molecules in neighboring pairs (13.17-13.20 Å). This inter-pair distance is also much smaller than the distance between molecules within the pair and the molecule in the center of the hexagonal array (13.18-15.49 Å). This may indicate a stronger interaction of the molecules within the pair that is absent in the structure of **5.4**. It should be mentioned that the molecules in the center of the hexagonal array of **5.5** (highlighted with blue hexagon shadowing in Figure 5.4c, d) contain molecules with remarkable crystal packing disorder. It is apparent from the ac-plane that the C_3 axis of these molecules is off-center from the c-axis of the surrounding crystals by about 20^{o}. In addition, the molecule was found to point with either Te1-up or Te3-up within the structure. For the purposes of refining the crystal structure, one orientation was chosen throughout the structure.

While performing further characterization of **5.5** in solution, it was observed that this cluster was relatively unstable in solution and would frequently plate its container with a metallic looking material over a week’s time. This suggests that the $P(NMe_2)_3$ ligands are labile, providing an opportunity for ligand exchange. Cluster **5.5** was dissolved in heptane with a large excess of

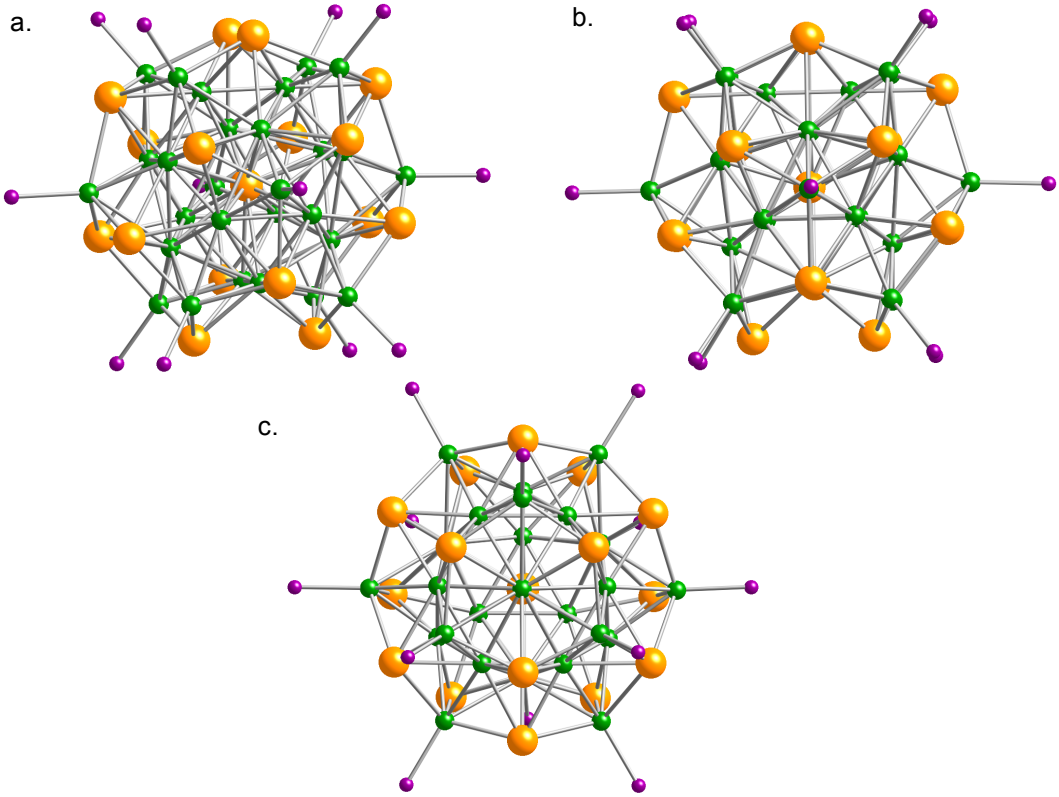

Figure 5.5. Molecular cluster **5.7**, the exchange product of **5.5** with an excess of PEt_3. Nickel (green), tellurium (orange), phosphorus (purple). a, b, and c are different views of the same cluster.

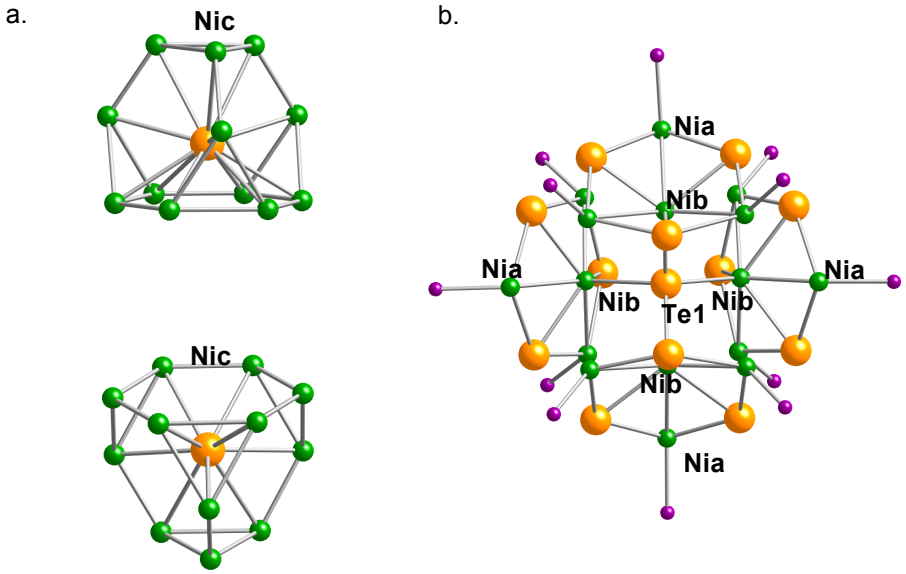

Figure 5.6. Deconstruction of cluster **5.7**. a) Two views of the inner twelve nickel atoms (green, Nic) bound to the central Te atom (orange, Te1). Other atoms in cluster **5.7** removed for clarity. b) Highlight of four central nickel atoms (green, Nib) closest to Te1. Nib atoms are each bound to three outer Nia atoms (green) and form a tetrahedron around Te1.

PEt_3 and left to crystallize for weeks. Small black crystals were obtained in extremely low yield. We hypothesized that this ligand exchange would either (1) maintain the cluster core structure while exchanging the $P(NMe_2)_3$ ligands for PEt_3 to give $Ni_7Te_5PEt_3$, (2) rearrange the cluster core and exchange the phosphine ligands to give the previously reported cluster **5.1**, or (3) give a completely different cluster. SCXRD data indicated that the latter was true, with the product having a structure of $Ni_{28}Te_{17}(PEt_3)_{12}$ (Figure 5.5, cluster **5.7**).

This cluster is quite complex, with three different nickel environments. There are twelve of the first type of nickel atom (Ni_a). These Ni_a atoms decorate the outside of the cluster and are bound to phosphine ligands. Ni_a atoms are also bonded to three tellurium atoms and three inner nickel atoms in a distorted capped trigonal prism, where the phosphine acts as the cap. There are sixteen inner nickel atoms, with four being in one environment (Ni_b) and twelve being in another (Ni_c) (Figure 5.6). Both Ni_b and Ni_c are bonded in a distorted tetrahedron to three outer tellurium atoms and the central tellurium atom. The distinction between these atoms is that Ni_b is bound to three Ni_a atoms while Ni_c is bound to two Ni_a atoms (Figure 5.5, 5.6b). Ni_b is bonded to an additional nine Ni_c atoms making Ni_b a thirteen coordinate system. The four Ni_b atoms form almost a perfect tetrahedron around the central tellurium atom, and are the closest nickel atoms to the central tellurium atom at a distance of 2.71-2.79 Å (Figure 5.6b). The Ni_c atoms are 2.88-2.93 Å from the central tellurium atom and have an eleven coordinate system (Figure 5.6a). They form a highly symmetrical fused hexagonal system within the cluster core.

Compared with the previously reported $Ni_{20}Te_{18}PEt_3$ (**5.2**) cluster, this cluster has a core that is much richer in nickel. This may be a result of the starting ratio of 1.4 Ni to 1 Te compared with the 1:1 ratio used for the synthesis of $Ni_{20}Te_{18}PEt_3$. The interesting magnetic properties that have been previously investigated for **5.2** make **5.7** an interesting target. However, the low yield of the synthesis of **5.7** made further characterization beyond SCXRD difficult. In an effort to find an improved route to **5.7**, we attempted to synthesize the cluster by reacting 0.5 equivalents of $Te(P(NMe_2)_3)$ with $Ni(COD)_2$ in an excess of $P(NMe_2)_3$, followed by immediate addition of excess PEt_3. After crystallizing for several days, black crystals were isolated and characterized by SCXRD to be a Ni_9Te_6 cluster core. This interesting result highlights the utility of ligand exchange

reactions for accessing additional nickel telluride cluster structures. This method of ligand exchange may be vital to discovering a host of new structures.

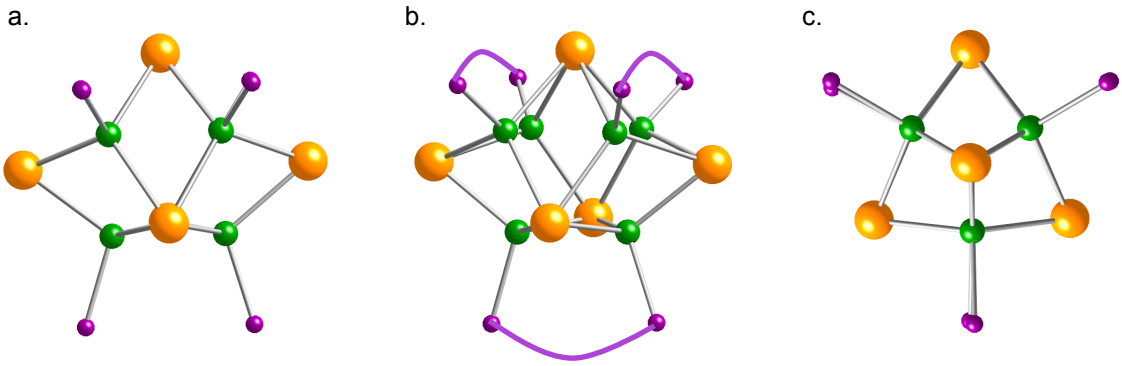

Figure 5.7. Molecular cluster **5.6**, the exchange product of **5.1** with an excess of DEPE. Nickel (green), tellurium (orange), phosphorus (purple). Ligand substitution is omitted for clarity, although purple connectors in (b) are a cartoon representation of the bridging depe ligands. a.-c. are different views of the same cluster.

In an effort to further explore the utility of ligand exchange for the development of novel cluster structures, we performed ligand exchange on **5.1** to replace PEt_3 ligands with (diethylphosphino)ethane (DEPE) ligands, a bridging ligand that is again an effectively bulky phosphine ligand. The resulting cluster **5.6** (Figure 5.1, 5.7) has a Ni_6Te_5 cluster core with three bidentate phosphines. While this structure is most certainly related to that of **5.4** and **5.5**, the clusters have several obvious differences. Cluster **5.6** lacks a central nickel atom and has two sets of three nickel atoms in a trigonal array that are eclipsed. With these structural features in mind, several conclusions can be drawn about why this structure is favored. As expected, the sterically bulky DEPE ligand forces a smaller size cluster. This ligand also requires that two nickel atoms be adjacent to each other and spaced at an appropriate distance for one DEPE to bridge the two. The distance between nickels bonded to the same phosphine ligand is 2.53-2.55 Å. Nickels within each trigonal array are separated by 2.65-2.69 Å. Both of these distances are much shorter than the Ni-Ni distances of **5.4** and **5.5**. This spacing requirement induced by the DEPE ligand is most likely the reason for the eclipsed sets of three nickel atoms and for the lack of a central nickel atom. The central nickel atom in **5.4** and **5.5** is coordinated to the outer six nickel atoms in a distorted octahedron, a coordination geometry not available with the eclipsed

sets of trigonal nickel atoms in **5.6**. In addition, the spacing constraints imposed by DEPE decreases the spacing of the cavity when compared to **5.2** and **5.3**.

Cluster **5.6** is also obviously structurally related to **5.3**, which has bridging (diphenylphosphino)methane (dppm) ligands. This dppm ligand can be considered even more sterically bulky than depe, and has a smaller distance between phosphines because the bridge has one carbon instead of two. These structural changes to the ligand impose that the bridged Ni atoms in the cluster be closer together in **5.3** and restrict the size of the resulting cluster even further. This follows nicely with our previous observations that an increase in steric bulk results in a decrease of cluster size. When comparing **5.3** with **5.6**, it looks as if the three nickel atoms in a trignoal array are a common element, with **5.3** having only one of these elements. Future work should explore whether **5.6** can be accessed directly by reaction of the Te(depe) with $Ni(COD)_2$, which is similar to the synthesis of **5.3**, or whether ligand exchange from **5.1** is necessary.

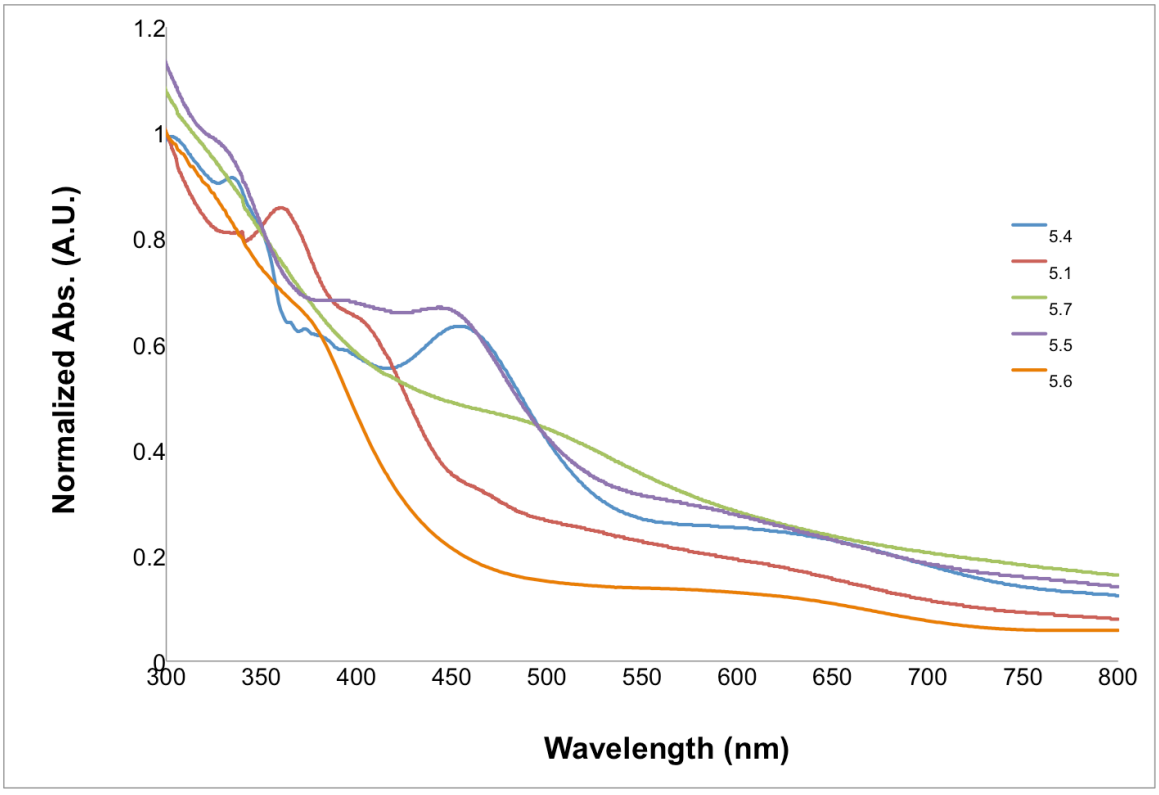

Figure 5.8. UV-visible absorption spectra of clusters **5.1**, **5.4**-**5.7**. Normalization is achieved by dividing each spectrum by the absorption maximum of that spectrum.

UV-visible absorption was used to preliminarily survey the difference in electronics between clusters within this family (Figure 5.8). The difference in spectra between clusters of different sizes demonstrates that core structure heavily impacts the electronics of the system. It is interesting to note that the spectra of **5.4** and **5.5** are extremely similar, indicating that the difference in electronics between P^iPr_3 and $P(NMe_2)_3$ is not significant enough to cause drastic changes to the core electronics. Cluster **5.4** and **5.5** have red-shifted absorption relative to **5.1** despite the fact that **5.1** has more metal and chalcogenide atoms in its core. The absorption profile of **5.1** is only slightly red-shifted relative to cluster **5.6**, even though the cluster core of **5.6** is much smaller than **5.1**. The fact that both larger (**5.1**) and smaller (**5.6**) clusters relative to **5.4** and **5.5** have a smaller absorption window may be related to the fact that the former are much more symmetrical structures than the latter. Further work could include calculations to probe the effect of symmetry on the electronics of these clusters. Cluster **5.7** has an extremely large absorption window with very broad features, reminiscent of thin film semiconductor UV-vis absorption profiles. This data indicates that the family of nickel telluride clusters is electronically complex and also extremely versatile, even with subtle structural changes. Further investigation into the electronics of this system will certainly unveil a wealth of interesting properties.

5.3 Experimental

5.3.1 Synthetic Details

5.3.1.1 General Information

Tellurium powder, bis(cyclooctadiene)nickel ($Ni(COD)_2$), triethylphosphine, triisopropylphosphine, and 1,2-bis(diethylphosphino)ethane were obtained from STREM Chemicals. Trisdimethylaminophosphine and all other reagents and solvents were purchased from Aldrich. Dry and deoxygenated hexanes, toluene, and THF were prepared by elution through a dual column solvent system (Glass Contour Solvent Systems). Other solvents were distilled from the appropriate drying agent (heptane and toluene-d_8 from sodium/benzophenone/tetraglyme, THF-d_8 from sodium/benzophenone). Unless otherwise noted, all reactions were carried out under nitrogen using standard schlenk techniques or in an argon-

filled glovebox. Only the IR peaks in the range 4000-1500 cm^{-1} are reported. All ^{1}H and ^{31}P NMR were recorded on a Bruker DRX300 (300 MHz), Bruker DRX400 (400 MHz), or Bruker DMX500 (500 MHz) spectrometer. Infrared (IR) spectra were obtained using a Perkin Elmer Spectrum 400 FTIR spectrometer using a PIKE ATR attachment.

5.3.1.2 Synthetic Procedures

Cluster 5.4 $[Ni_7Te_5(P^iPr_3)_6]$: To a 20-mL vial was added a stirbar, triisopropylphosphine (3.5 g, 22 mmol), and 5 mL of hexanes. While stirring, tellurium powder (0.115 g, 0.9 mmol) was added to the solution. The solution was allowed to stir at room temperature until all of the tellurium powder was dissolved (approximately 2 hours). $Ni(COD)_2$ (0.522 g, 1.9 mmol) was added, causing an immediate color change of the solution from clear yellow to a dark red-brown. The solution was allowed to stir at room temperature for 25 minutes before being filtered and left to crystallize in a glovebox freezer at -30°C for 5 days. Crystals were rinsed with 1 mL of hexanes five times and allowed to dry to give dark black-brown crystals. Yield: 22 mg, 6 %.

IR (ATR) = 2948, 2928, 2869 cm^{-1}

Triisopropylphosphine telluride: ^{1}H NMR (400 MHz, [d_8-THF], 298 K): δ = 1.23-1.29 (18H, m), 2.18-2.28 (3H, m). ^{31}P NMR (162 MHz, [d_8-THF], 298 K): δ = 42.32 ppm.

Cluster 5.5 $[Ni_7Te_5(P(NMe_2)_3)_6]$: To a 20-mL vial was added a stirbar, tris(dimethylamino)phosphine (2.43 g, 13.6 mmol), and 5 mL of cyclohexane. While stirring, tellurium powder (0.075 g, 0.59 mmol) was added to the solution. The solution was allowed to stir at room temperature until all of the tellurium powder was dissolved (approximately 30 minutes). $Ni(COD)_2$ (0.323 g, 1.2 mmol) was added, causing an immediate color change of the solution from cloudy yellow to a dark red-brown. The solution was allowed to stir at room temperature for 25 minutes before being filtered and left to crystallize at room temperature for 5 days. Crystals were rinsed with 1 mL of heptane ten times followed by rinsing with 1 mL of hexanes six times and allowed to dry. Resulting crystals were black. Yield: 55 mg, 23 %.

^{1}H NMR (400 MHz, [d_8-toluene], 298 K): δ = 2.58-2.59 (108H, m).

^{31}P NMR (162 MHz, [d_8-toluene], 298 K): δ = 142 (broad peak).

IR (ATR) = 3000, 2880, 2863, 2841, 2818, 2784, 1647 cm^{-1}.

Elem. Anal. Calc. for $C_{36}H_{108}N_{18}Ni_7P_6Te_5$: C, 21.32; H, 5.37; N, 12.43; Ni, 20.26; P, 9.16; Te, 31.46. Found: C, 20.34; H, 5.12; N, 11.60; Ni, 21.04; P, 8.25; Te, 32.69.

Tris(dimethylamino)phosphine telluride: ^{1}H NMR (400 MHz, [d_8-toluene], 298 K): δ = 2.27-2.30 (18H, m). ^{31}P NMR (162 MHz, [d_8-toluene], 298 K): δ = 59.21 (broad peak).

Cluster 5.7 [$Ni_{28}Te_{17}(PEt_3)_{12}$]: Cluster **5.5** (0.032 g, 0.016 mmol) was dissolved in heptane in a 20-mL vial with a stirbar. Triethylphosphine (0.025 g, 0.21 mmol) was added, and the resulting reaction mixture was stirred for 10 minutes. The solution was filtered and left to crystallize for one week. Yield: 1 mg, 4.5 %.

Cluster 5.6 [$Ni_6Te_5(DEPE)_3$]: Solid **5.1** (0.105 g, 0.0466 mmol) was dissolved in 5 mL of toluene by stirring for 1h. The dark solution was filtered and depe (0.189 g, 0.916 mmol) was added. After shaking briefly, the solution was allowed to stand at room temperature overnight to produce large dark crystals. Yield: 32 mg, 36%.

^{1}H NMR (400 MHz, [d_8-toluene], 298 K): δ = 1.29 (48H, m, broad), 1.07-1.03 (24H, m)

IR (ATR) = 3031, 2970, 2931, 2864, 1741 cm^{-1}.

Elem. Anal. Calc. for $C_{30}H_{72}Ni_6P_6Te_5$: C, 22.40; H, 4.51; Ni, 21.89; P, 11.55; Te, 39.65. Found: C, 22.14; H, 4.40; Ni, 19.30; P, 9.71; Te, 36.02.

5.3.3. UV-visible Spectroscopy

Absorption spectra were taken on a Shimadzu UV-1800 spectrophotometer. All spectra were taken under nitrogen in a 1-cm quartz cuvette following a recording of the background spectrum.

5.4 Acknowledgements

The author would like to thank Xavier Roy for helpful discussions as well as his assistance with synthesis and characterization. Ari Turkeiwicz should also be recognized for his contribution to the synthesis and characterization of these molecules. Roger Lalancette and Theo Seigrist should be acknowledged for their role in SCXRD measurements and analysis. The author would like to thank Mike Steigerwald for the helpful discussions that guided this project.

5.5 Conclusions

In this chapter, we have expanded the family of nickel telluride clusters by two methods. First, we incorporated bulky phosphine ligands to synthesize a Ni_7Te_5 cluster core. Both P^iPr_3 and $P(NMe_2)_3$ gave the same core, despite being electronically different. The second method utilized ligand exchange of **5.5** with PEt_3 to give an extremely large $Ni_{28}Te_{17}(PEt_3)_{12}$ cluster and of **5.1** with a bridging phosphine to give $Ni_6Te_5depe_3$. These two methods open up a host of possibilities given the number of ligands and the large set of clusters now known for this family. UV-vis spectroscopy highlights that small changes in cluster structure have large impacts on the electronic structure of the system. In addition, it demonstrates the potential for this class of molecules for electronic applications.

5.6 References

[1] E. Uchida, H. Kondoh, *J. Phys. Soc. Jap.* **1956**, *11*, 21-27.

[2] N. Umeyama, M. Tokumoto, S. Yagi, M. Tomura, K. Tokiwa, T. Fujii, R. Toda, N. Miyakawa, S.-I. Ikeda, *Jap. J. Appl. Phys.* **2012**, *51*, 053001.

[3] A. K. Dua, R. P. Agarwala, *Thin Solid Films.* **1971**, *8*, 307-315.

[4] T. T. M. Palstra, M. L. Steigerwald, A. P. Ramirez, Y.-U. Kwon, S. M. Stuczynski, L. F. Schneemeyer, J. V. Waszczak, J. Zaanen, *Phys. Rev. Lett.* **1993**, *71*, 1768-1771.

[5] J. G. Brennan, T. Siegrist, S. M. Stuczynski, M. L. Steigerwald, *J. Am. Chem. Soc.* **1989**, *111*, 9240-9241.

[6] Z. Nomikou, B. Schubert, R. Hoffmann, M. L. Steigerwald, *Inorg. Chem.* **1992**, *31*, 2201-2209.

[7] T. T. M. Palstra, M. L. Steigerwald, A. P. Ramirez, J. Zaanen, *Physica B.* **1994**, *199*, 619-621.

[8] G. M. Ferrence, P. E. Fanwick, C. P. Kubiak, *Chem. Commun.* **1996**, 1575-1576.

[9] P. Wix, G. E. Kostakis, V. A. Blatov, D. M. Proserpio, S. P. Perlepes, A. K. Powell, *Eur. J. Inorg. Chem.* **2013**, 520-256.

[10] M. L. Steigerwald, S. M. Stuczynski, Y.-U. Kwon, D. A. Vennos, J. G. Brennan, *Inorg. Chim. Acta.* **1993**, *212*, 219-224.

[11] X. Roy, C.-H. Lee, A. C. Crowther, C. L. Schenck, T. Besara, R. A. Lalancette, T. Siegrist, P. W. Stephens, L. E. Brus, P. Kim, M. L. Steigerwald, C. Nuckolls, *Science*. **2013**, DOI: 10.1126/science.1236259.

[12] M. L. Steigerwald, T. Siegrist, E. M. Gyorgy, B. Hessen, Y.-U. Kwon, S. M. Tanzler, *Inorg. Chem.* **1994**, *33*, 3389-3395.

[13] J. Barstad, F. Grønvold, E. Røst, E. Vestersjø, *Acta Chem. Scand.* **1966**, *20*, 2865.

[14] D. Benito-Garagorri, V. Bocokić, K. Mereiter, K. Kirchner, *Organomet.* **2006**, *25*, 3817-3823.

[15] D. K. Dutta, J. D. Woollins, A. M. Z. Slawin, D. Konwar, M. Sharma, P. Bhattacharyya, S. T. Aucott, *J. Organomet. Chem.* **2006**, *691*, 1229.

[16] R. M. Ceder, C. García, A. Grabulosa, F. Karipcin, G. Muller, M. Rocamora, M. Font-Bardía, X. Solans, *J. Organometal. Chem.* **2007**, *692*, 4005-4019.

[17] C. Romming, A. J. Iverson, J. Songstad, *Acta Chem. Scand.* **1980**, *A34*, 333.

[18] J. Gopalakrishnan, *Appl. Organometal. Chem.* **2009**, *23*, 291-318.

[19] T. Q. Ly, A. M. Z. Slawin, J. D. Woollins, *J. Chem. Soc., Dalton Trans.* **1997**, 1611-1616.

Appendix A. Supplemental Information for Chapter 2

A.1. Fluorescence Quenching and Quantum Yield Determination Experimental Analysis

A.1.1. Fluorescence Quenching with C_{60}

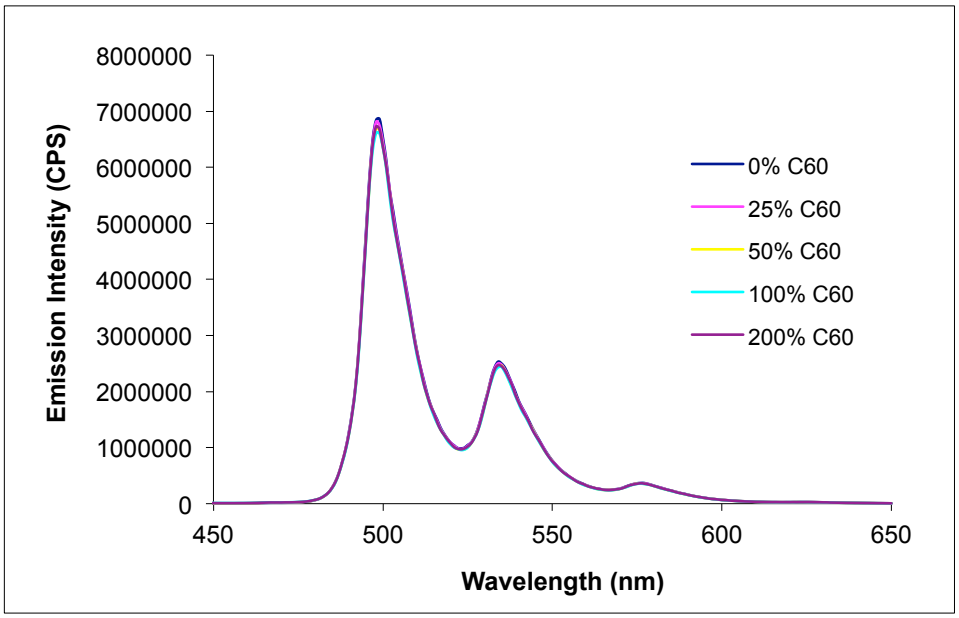

Figure A.1. Fluorescence spectra of **2.2** (1.0 x 10^{-6} M in CH_2Cl_2) with addition of 0%-200% C_{60}. Excited at 500 nm. Calculated association constant was 1.6 x 10^2.

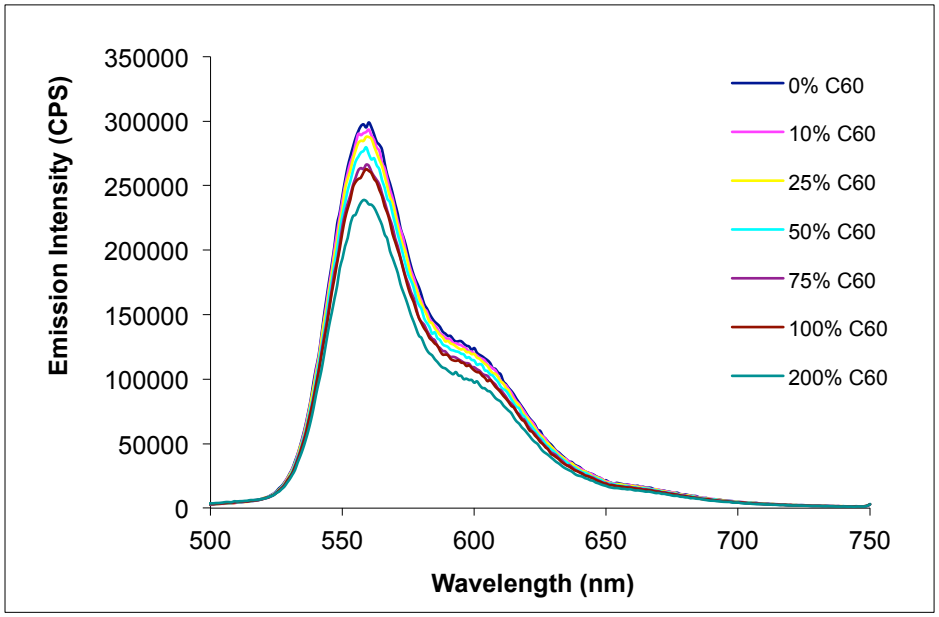

Figure A.2. Fluorescence spectra of **2.3** (1.0 x 10^{-6} M in CH_2Cl_2) with addition of 0%-200% C_{60}. Excited at 600 nm. Calculated association constant was 1.4 x 10^5.

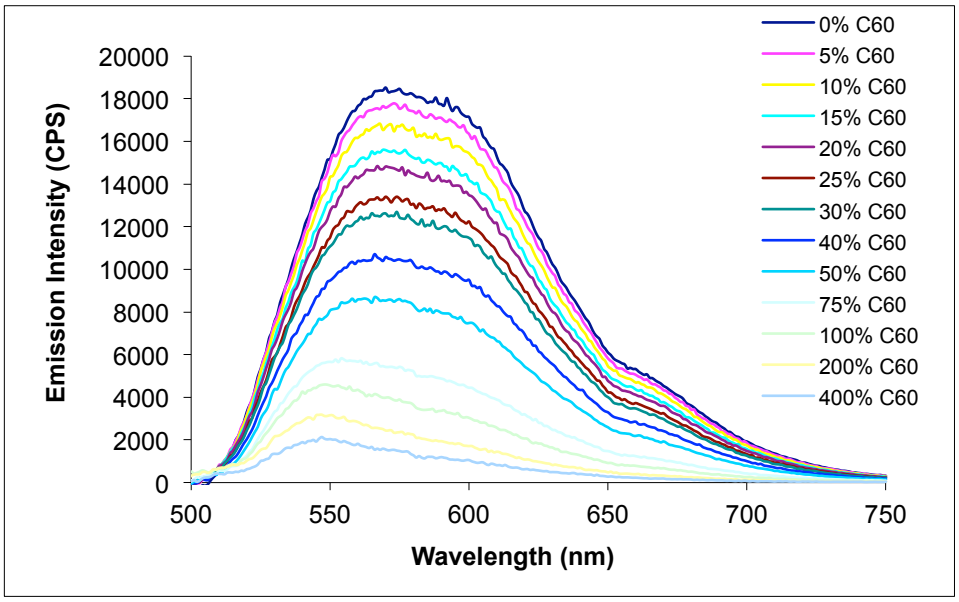

Figure A.3. Fluorescence spectra of **2.4** (1.0 x 10^{-9} M in CH_2Cl_2) with addition of 0%-400% C_{60}. Excited at 600 nm. Calculated association constant was 5 x 10^6.

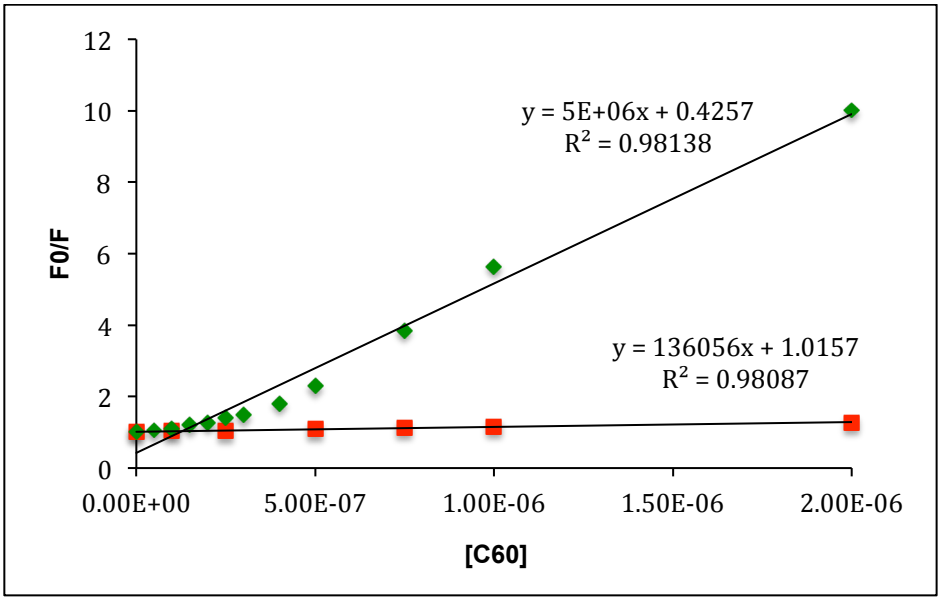

Figure A.4. Stern-Volmer plot of the ratio of initial fluorescence of **2.3** (red) and **2.4** (green) to fluorescence at a given C_{60} concentration versus C_{60} concentration. Slope of each line represents the association constant.

A.1.2. Fluorescence Quenching with $PC_{60}BM$

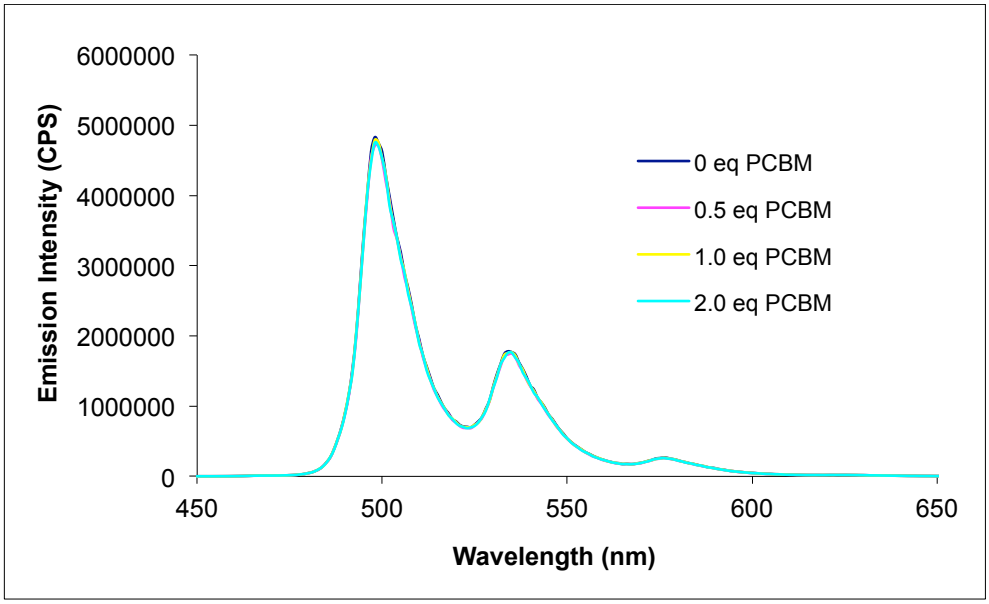

Figure A.5. Fluorescence spectra of **2.2** 1.0 x 10^{-9} M in CH_2Cl_2) with addition of 0-2.0 equivalents of $PC_{60}BM$. Excited at 500 nm. No measurable association.

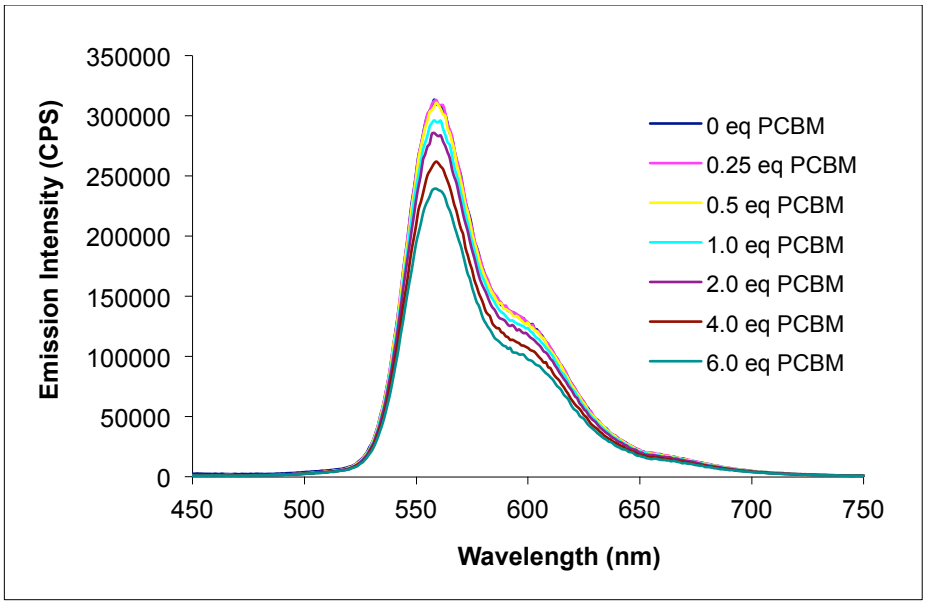

Figure A.6. Fluorescence spectra of **2.3** (1.0 x 10^{-9} M in CH_2Cl_2) with addition of 0-6.0 equivalents of $PC_{60}BM$. Excited at 600 nm. Calculated association constant was 5.4 x 10^4.

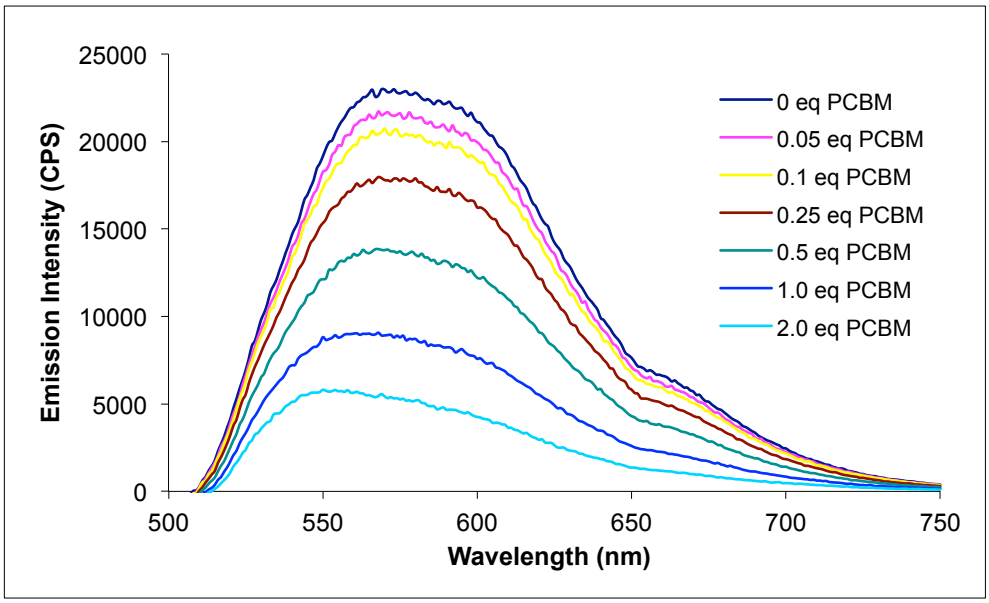

Figure A.7. Fluorescence spectra of **2.4** (1.0×10^{-9} M in CH_2Cl_2) with addition of 0-2.0 equivalents of $PC_{60}BM$. Excited at 600 nm. Calculated association constant was 1.4×10^6.

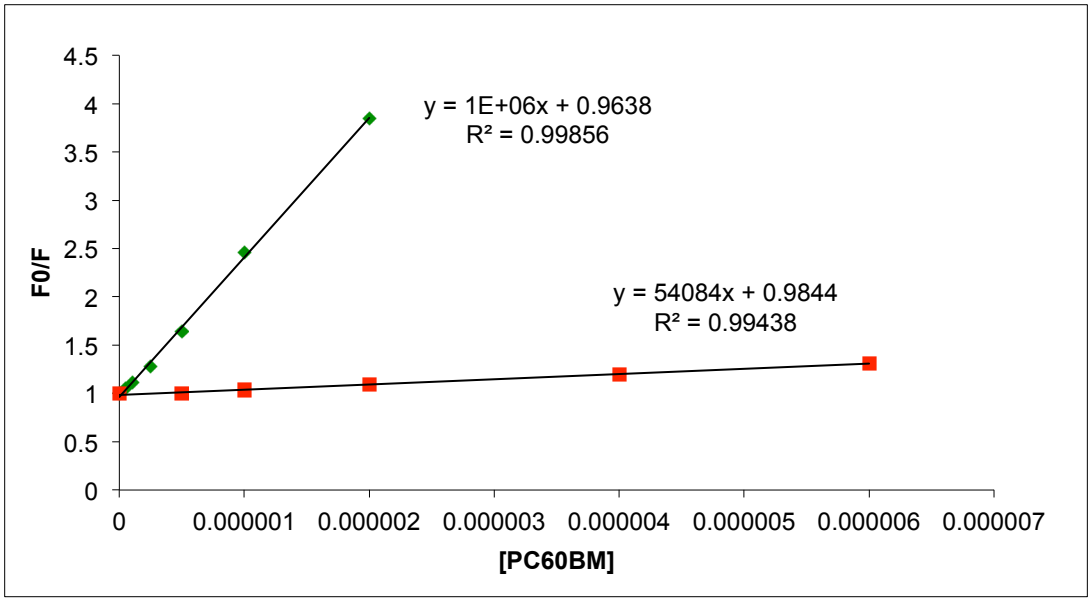

Figure A.8. Stern-Volmer plot of the ratio of initial fluorescence of **2.3** (red) and **2.4** (green) to fluorescence at a given $PC_{60}BM$ concentration versus $PC_{60}BM$ concentration. Slope of each line represents the association constant.

A.2. NMR Titration Experiments

A.2.1 NMR Titration Experiments with 2.2 and $PC_{60}BM$

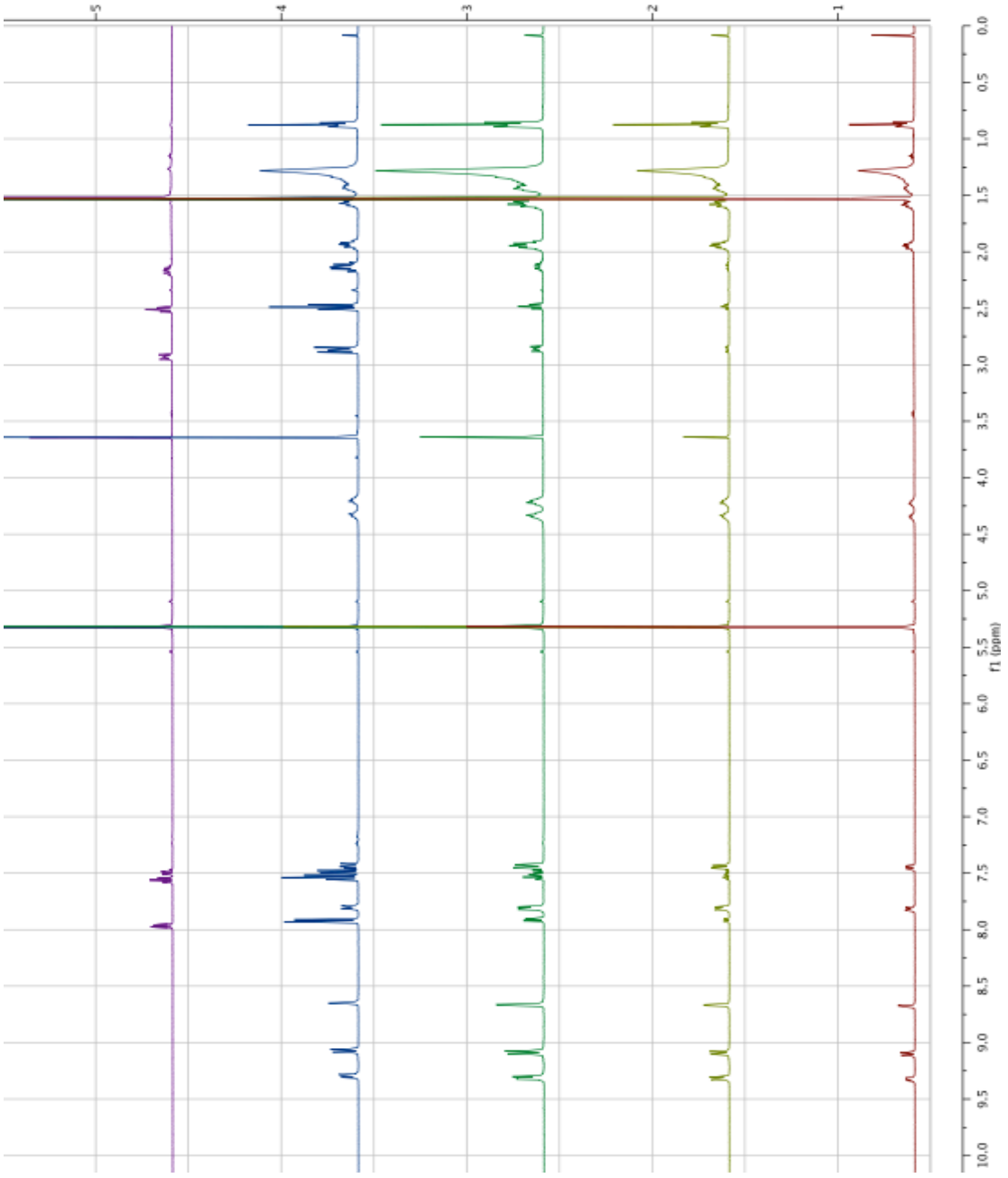

Figure A.9. ^{1}H NMR spectra in CD_2Cl_2 of **2.2** (1-red). **2.2** with 0.5 eq. $PC_{60}BM$ (2-yellow), **2.2** with 1.0 eq. $PC_{60}BM$ (3-green), **2.2** with 5.0 eq. $PC_{60}BM$ (4-blue), and $PC_{60}BM$ (5-purple).

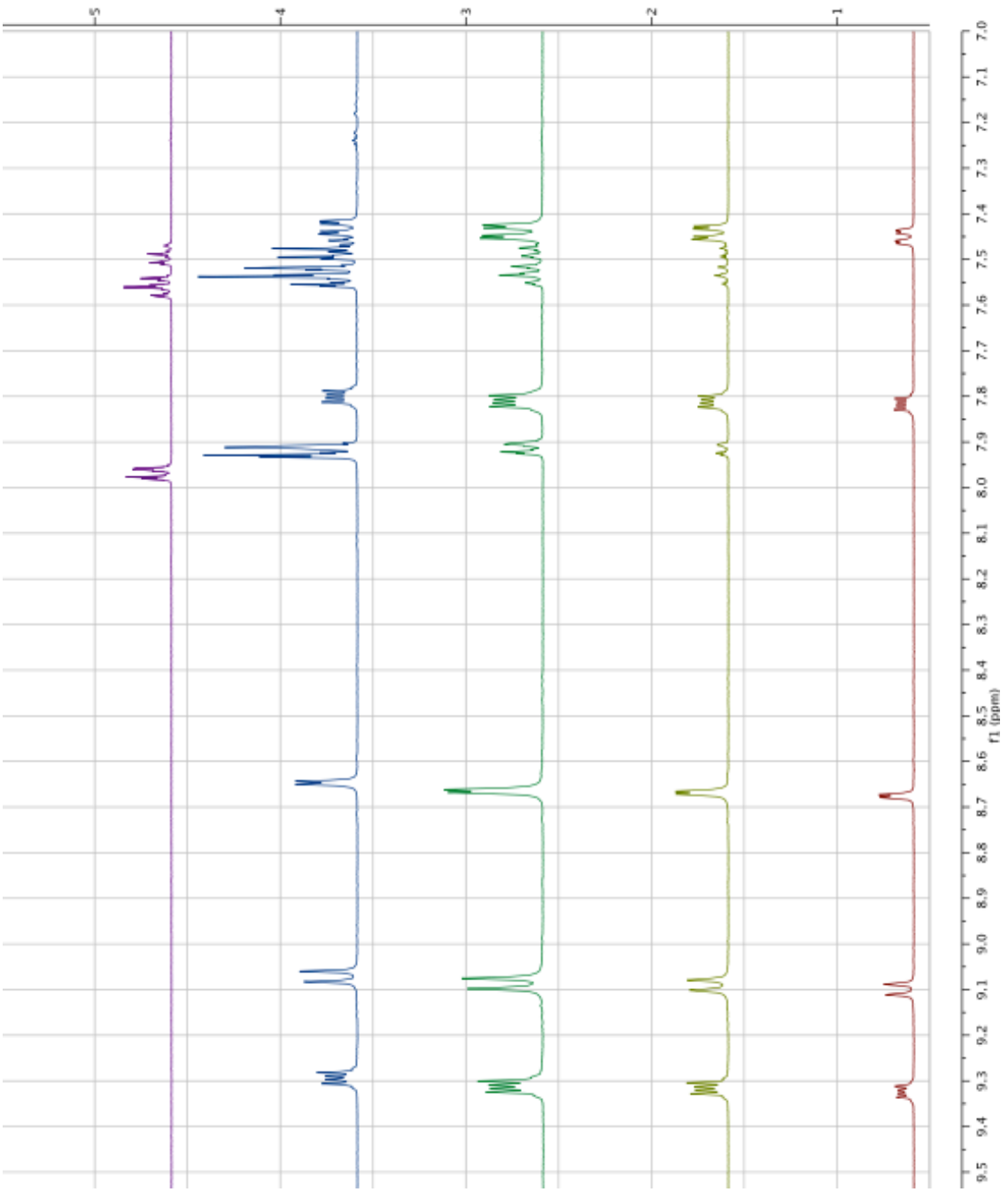

Figure A.10. Aromatic region of ^{1}H NMR spectra in CD_2Cl_2 of **2.2** (1-red). **2.2** with 0.5 eq. $PC_{60}BM$ (2-yellow), **2.2** with 1.0 eq. $PC_{60}BM$ (3-green), **2.2** with 5.0 eq. $PC_{60}BM$ (4-blue), and $PC_{60}BM$ (5-purple).

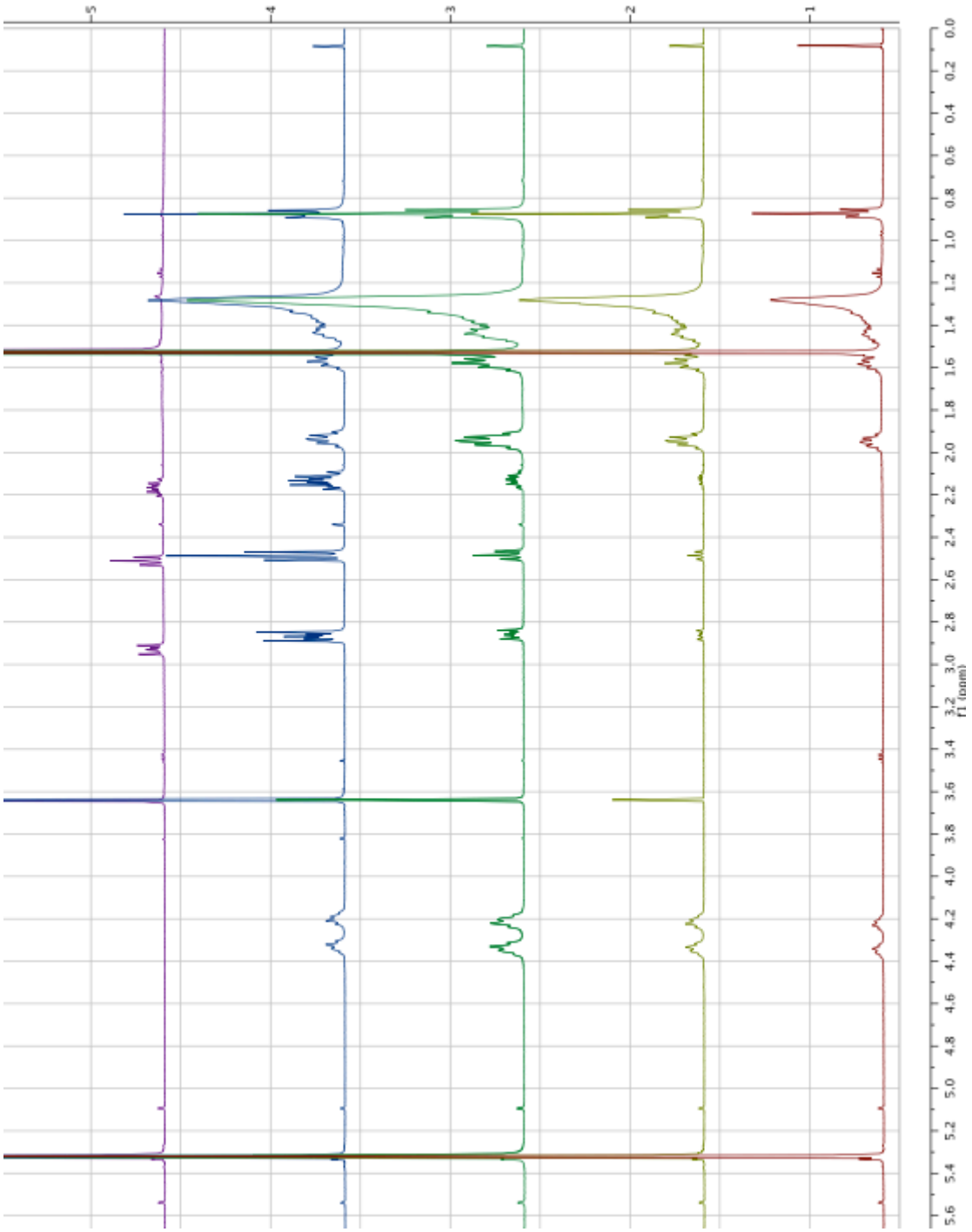

Figure A.11. Aliphatic region of ^{1}H NMR spectra in CD_2Cl_2 of **2.2** (1-red). **2.2** with 0.5 eq. $PC_{60}BM$ (2-yellow), **2.2** with 1.0 eq. $PC_{60}BM$ (3-green), **2.2** with 5.0 eq. $PC_{60}BM$ (4-blue), and $PC_{60}BM$ (5-purple).

A.2.2 NMR Titration Experiments with 2.3 and $PC_{60}BM$

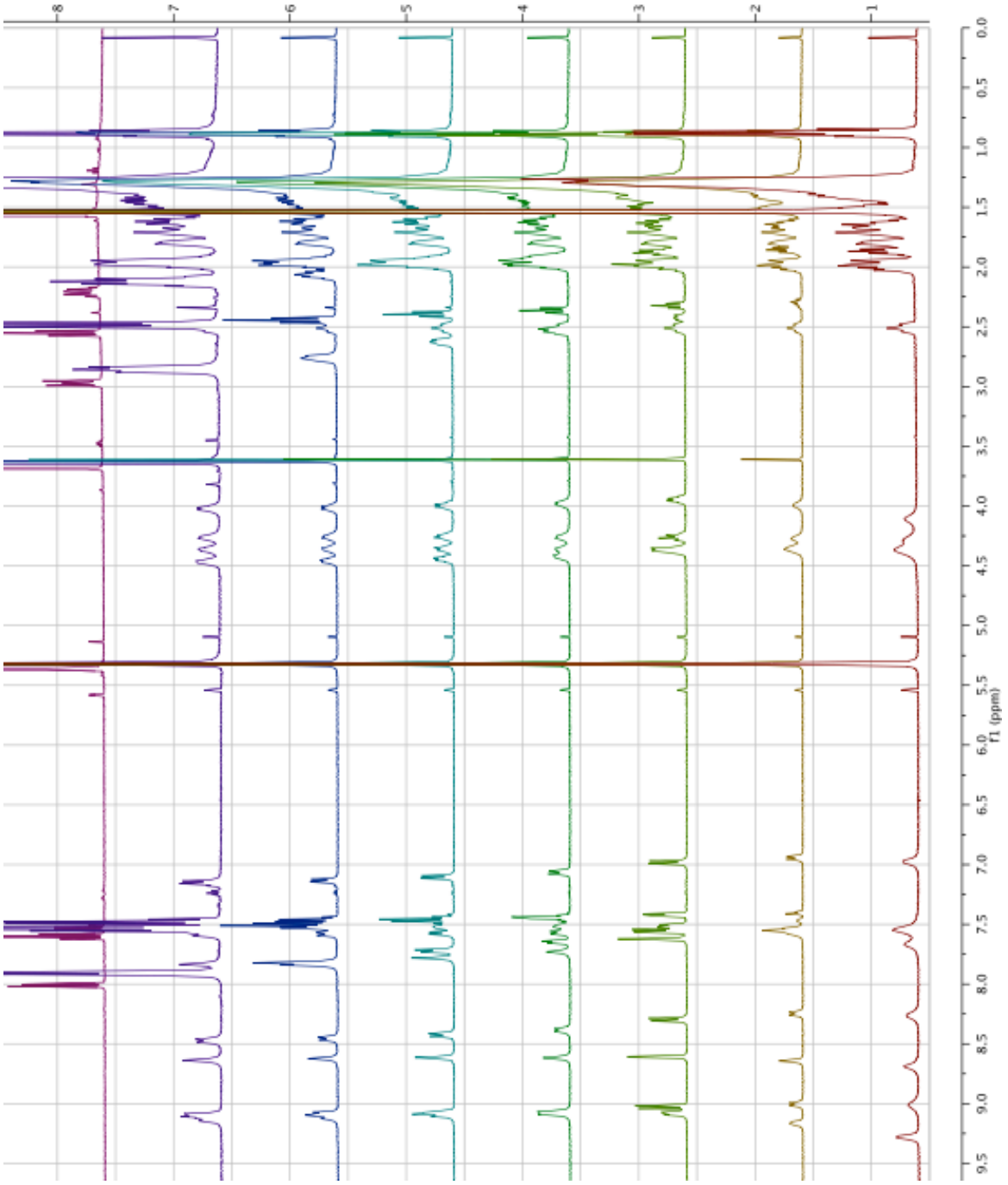

Figure A.12. ^{1}H NMR spectra in CD_2Cl_2 of **2.3** (1-red). **2.3** with 0.24 eq. $PC_{60}BM$ (2-yellow), **2.3** with 0.51 eq. $PC_{60}BM$ (3-yellow-green), **2.3** with 0.77 eq. $PC_{60}BM$ (4-green), **2.3** with 1.07 eq. $PC_{60}BM$ (5-blue-green), **2.3** with 2.0 eq. $PC_{60}BM$ (6-blue), **2.3** with 4.95 eq. $PC_{60}BM$ (7-purple), and $PC_{60}BM$ (8-maroon).

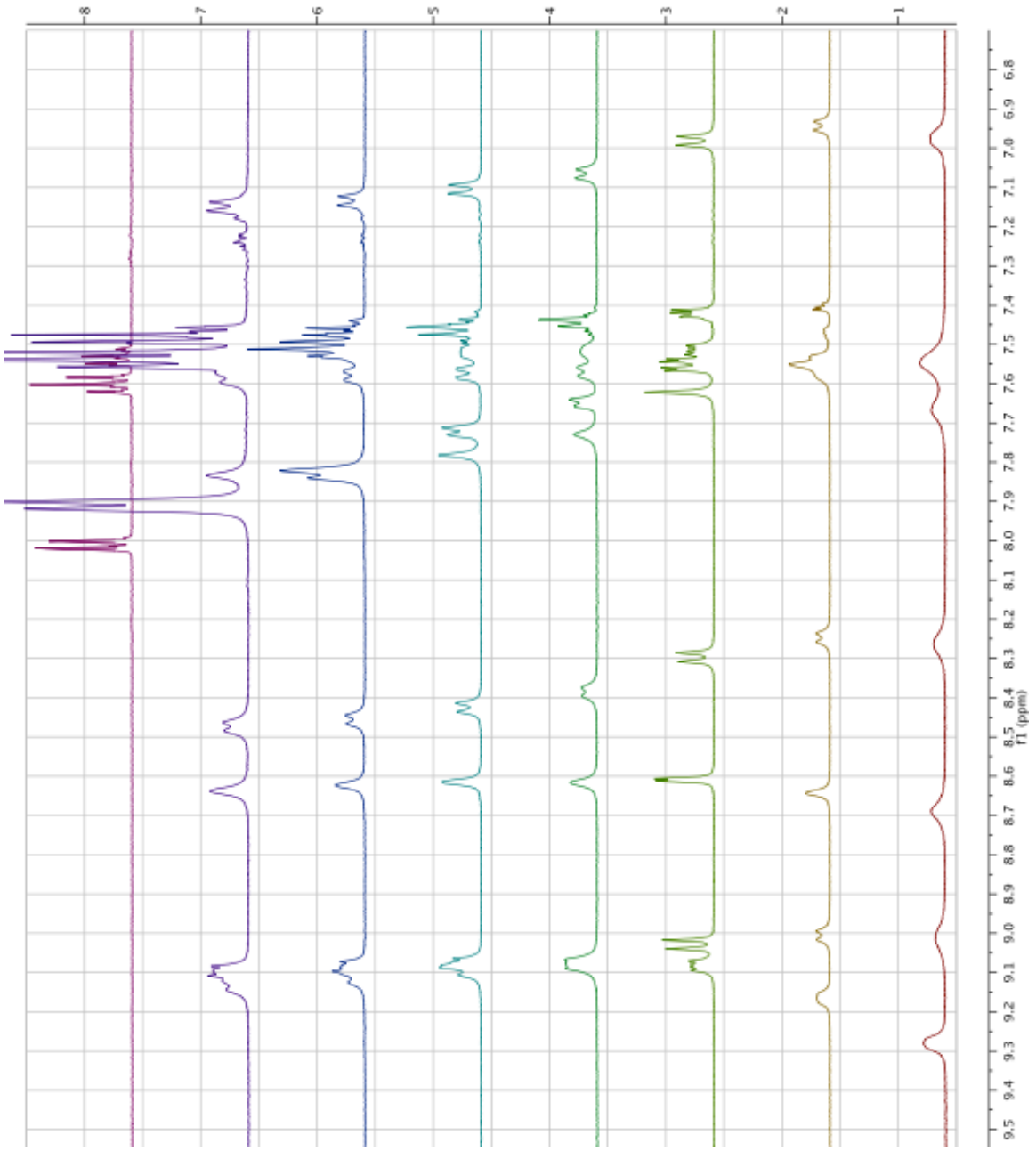

Figure A.13. Aromatic region of ^{1}H NMR spectra in CD_2Cl_2 of **2.3** (1-red). **2.3** with 0.24 eq. $PC_{60}BM$ (2-yellow), **2.3** with 0.51 eq. $PC_{60}BM$ (3-yellow-green), **2.3** with 0.77 eq. $PC_{60}BM$ (4-green), **2.3** with 1.07 eq. $PC_{60}BM$ (5-blue-green), **2.3** with 2.0 eq. $PC_{60}BM$ (6-blue), **2.3** with 4.95 eq. $PC_{60}BM$ (7-purple), and $PC_{60}BM$ (8-maroon).

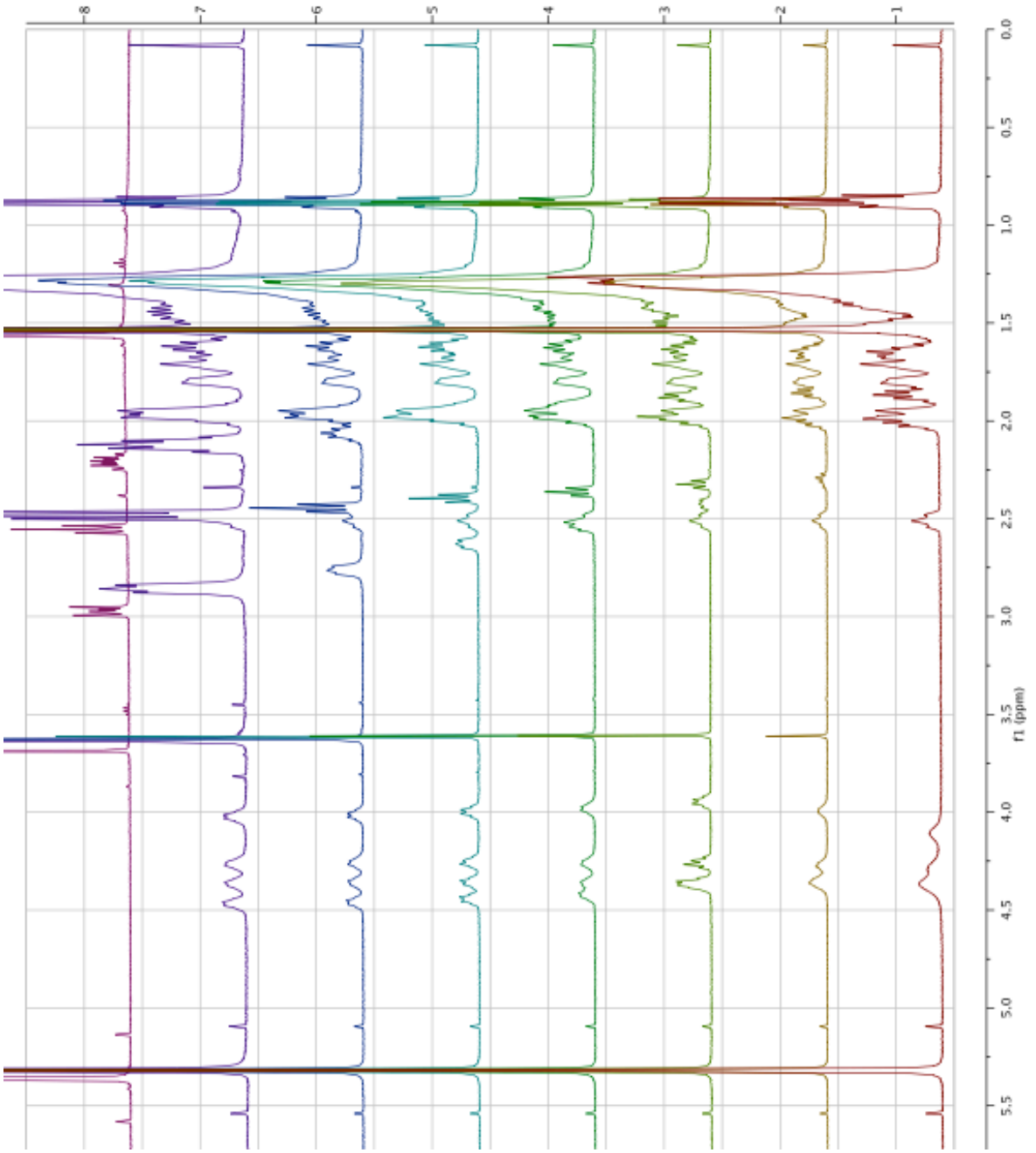

Figure A.14. Aliphatic region of ^{1}H NMR spectra in CD_2Cl_2 of **2.3** (1-red). **2.3** with 0.24 eq. $PC_{60}BM$ (2-yellow), **2.3** with 0.51 eq. $PC_{60}BM$ (3-yellow-green), **2.3** with 0.77 eq. $PC_{60}BM$ (4-green), **2.3** with 1.07 eq. $PC_{60}BM$ (5-blue-green), **2.3** with 2.0 eq. $PC_{60}BM$ (6-blue), **2.3** with 4.95 eq. $PC_{60}BM$ (7-purple), and $PC_{60}BM$ (8-maroon).

A.2.3 NMR Titration Experiments with 2.4 and $PC_{60}BM$

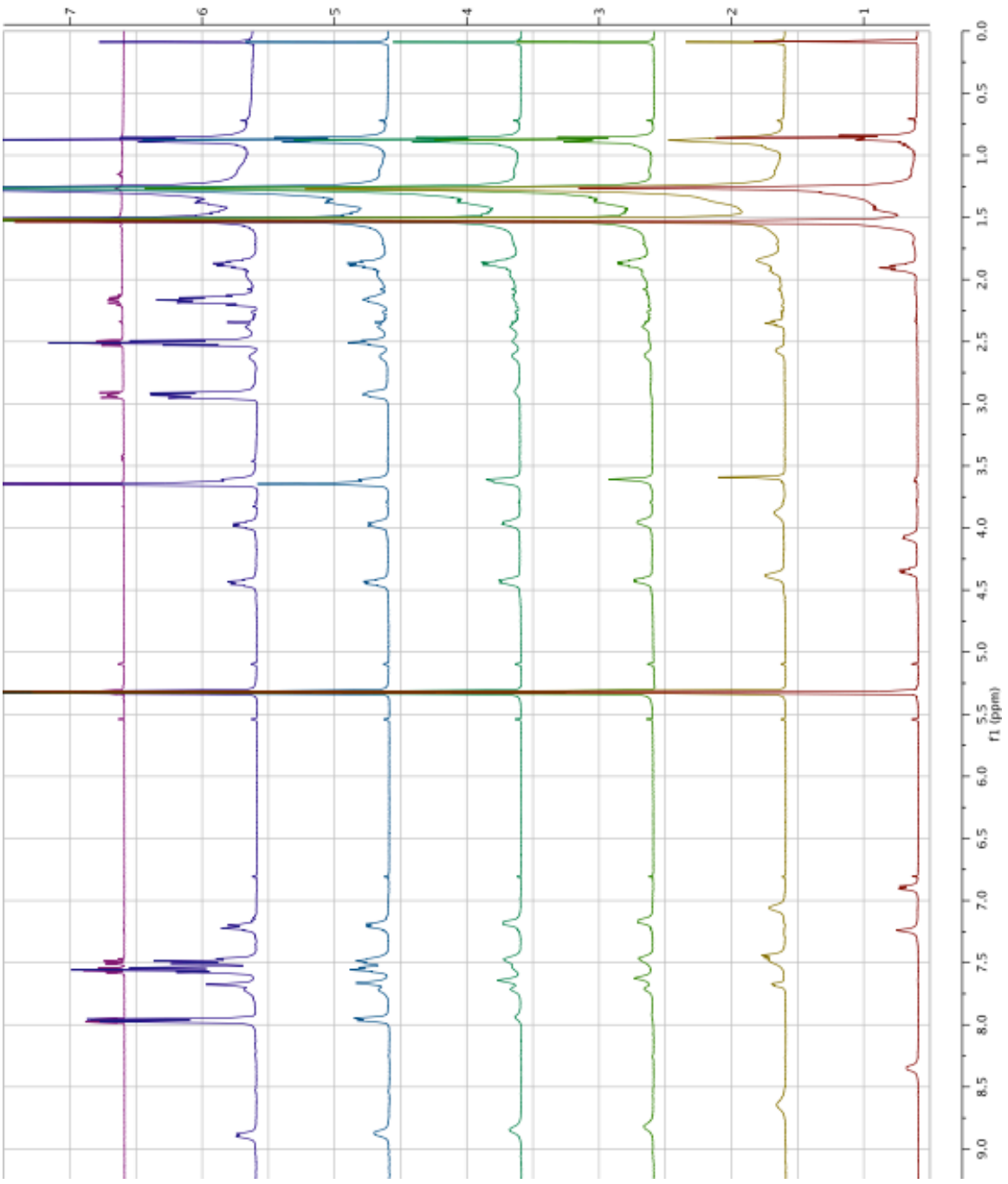

Figure A.15. ^1H NMR spectra in CD_2Cl_2 of **2.4** (1-red). **2.4** with 0.5 eq. $PC_{60}BM$ (2-yellow), **2.4** with 0.77 eq. $PC_{60}BM$ (3-yellow-green), **2.4** with 1.0 eq. $PC_{60}BM$ (4-green), **2.4** with 2.0 eq. $PC_{60}BM$ (5-blue), **2.4** with 5.0 eq. $PC_{60}BM$ (6-purple), and $PC_{60}BM$ (7-maroon).

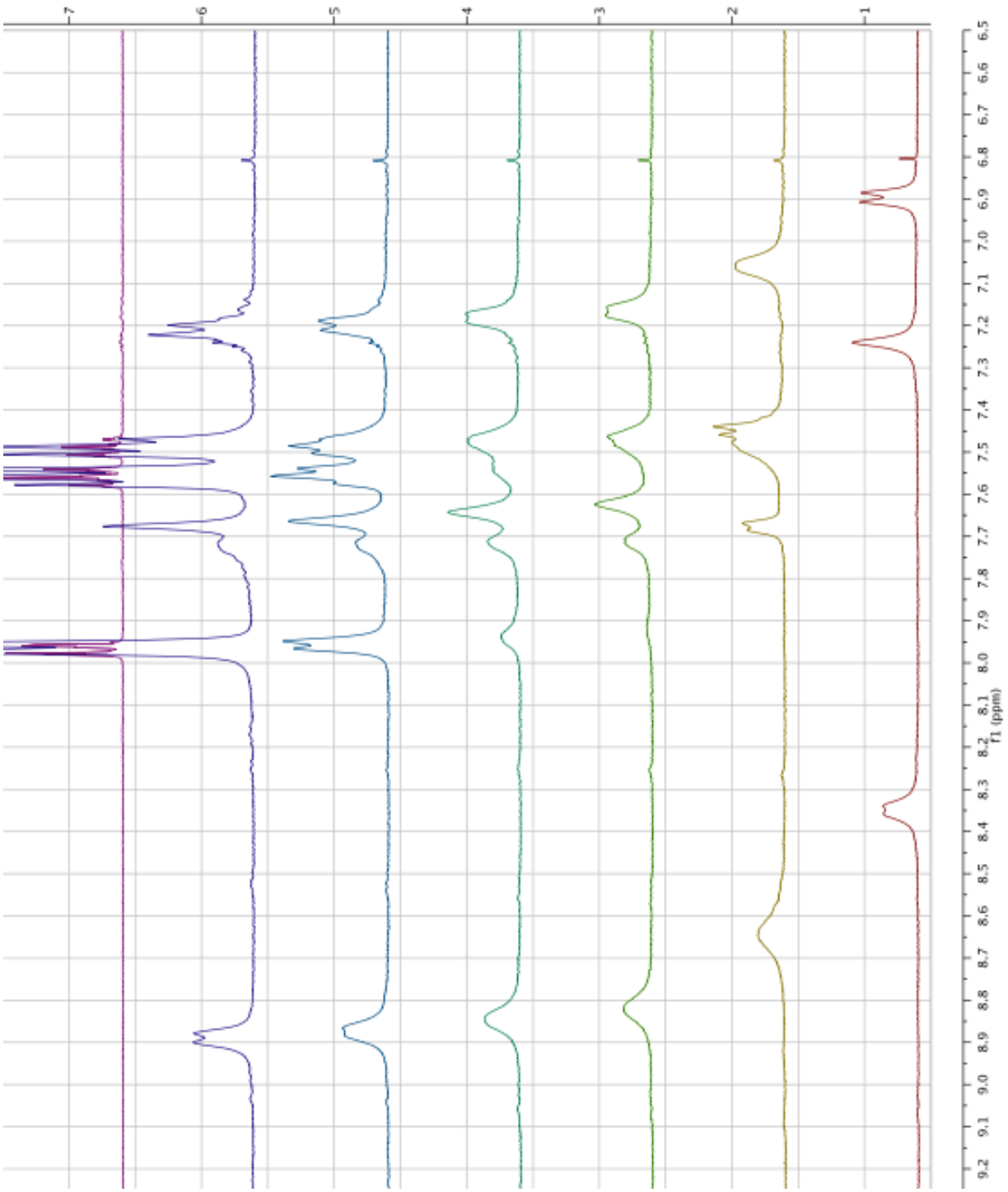

Figure A.16. Aromatic region of ^{1}H NMR spectra in CD_2Cl_2 of **2.4** (1-red). **2.4** with 0.5 eq. $PC_{60}BM$ (2-yellow), **2.4** with 0.77 eq. $PC_{60}BM$ (3-yellow-green), **2.4** with 1.0 eq. $PC_{60}BM$ (4-green), **2.4** with 2.0 eq. $PC_{60}BM$ (5-blue), **2.4** with 5.0 eq. $PC_{60}BM$ (6-purple), and $PC_{60}BM$ (7-maroon).

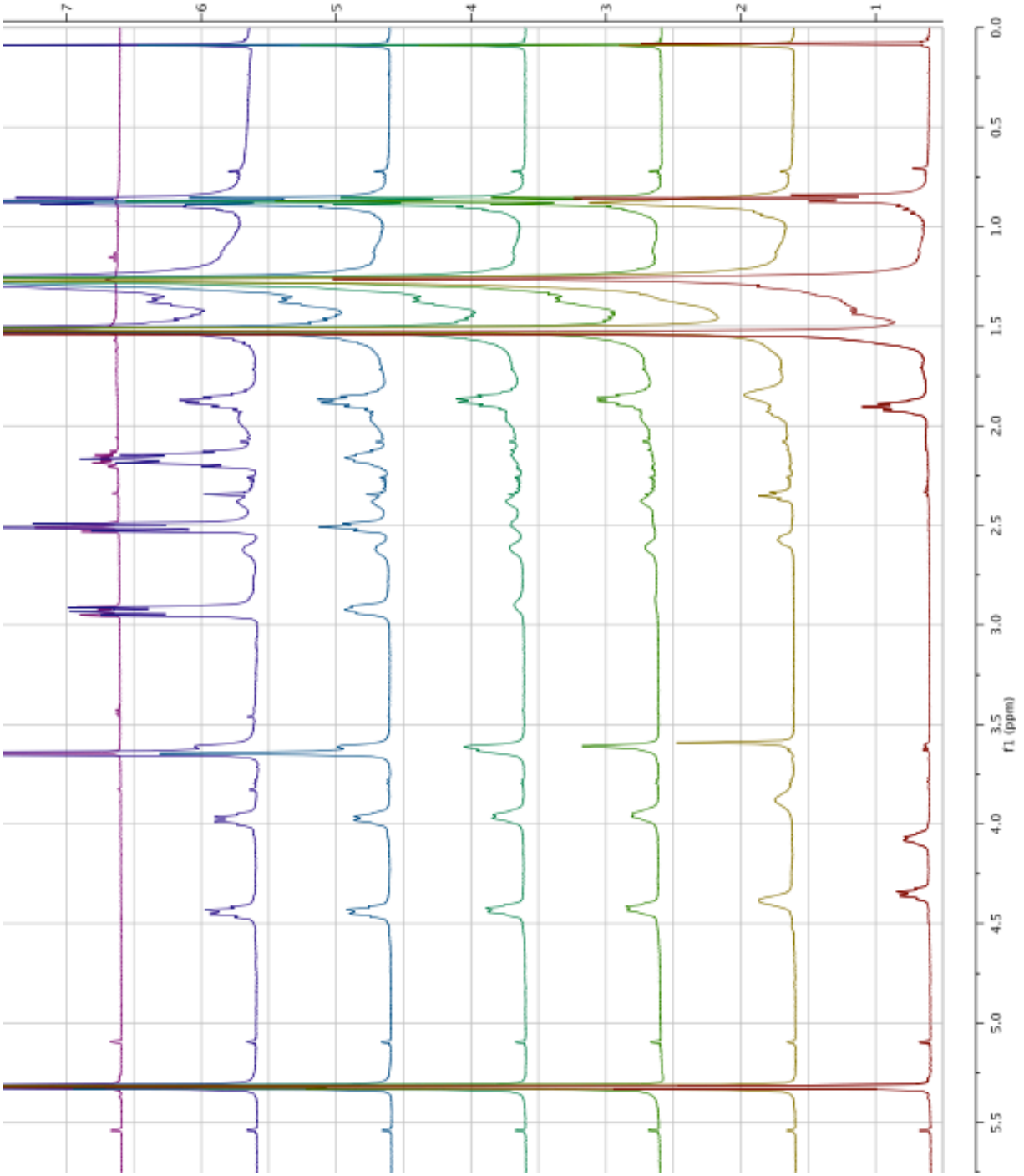

Figure A.17. Aliphatic region of ^{1}H NMR spectra in CD_2Cl_2 of **2.4** (1-red). **2.4** with 0.5 eq. $PC_{60}BM$ (2-yellow), **2.4** with 0.77 eq. $PC_{60}BM$ (3-yellow-green), **2.4** with 1.0 eq. $PC_{60}BM$ (4-green), **2.4** with 2.0 eq. $PC_{60}BM$ (5-blue), **2.4** with 5.0 eq. $PC_{60}BM$ (6-purple), and $PC_{60}BM$ (7-maroon).

A.3. ^{1}H NMR Spectra

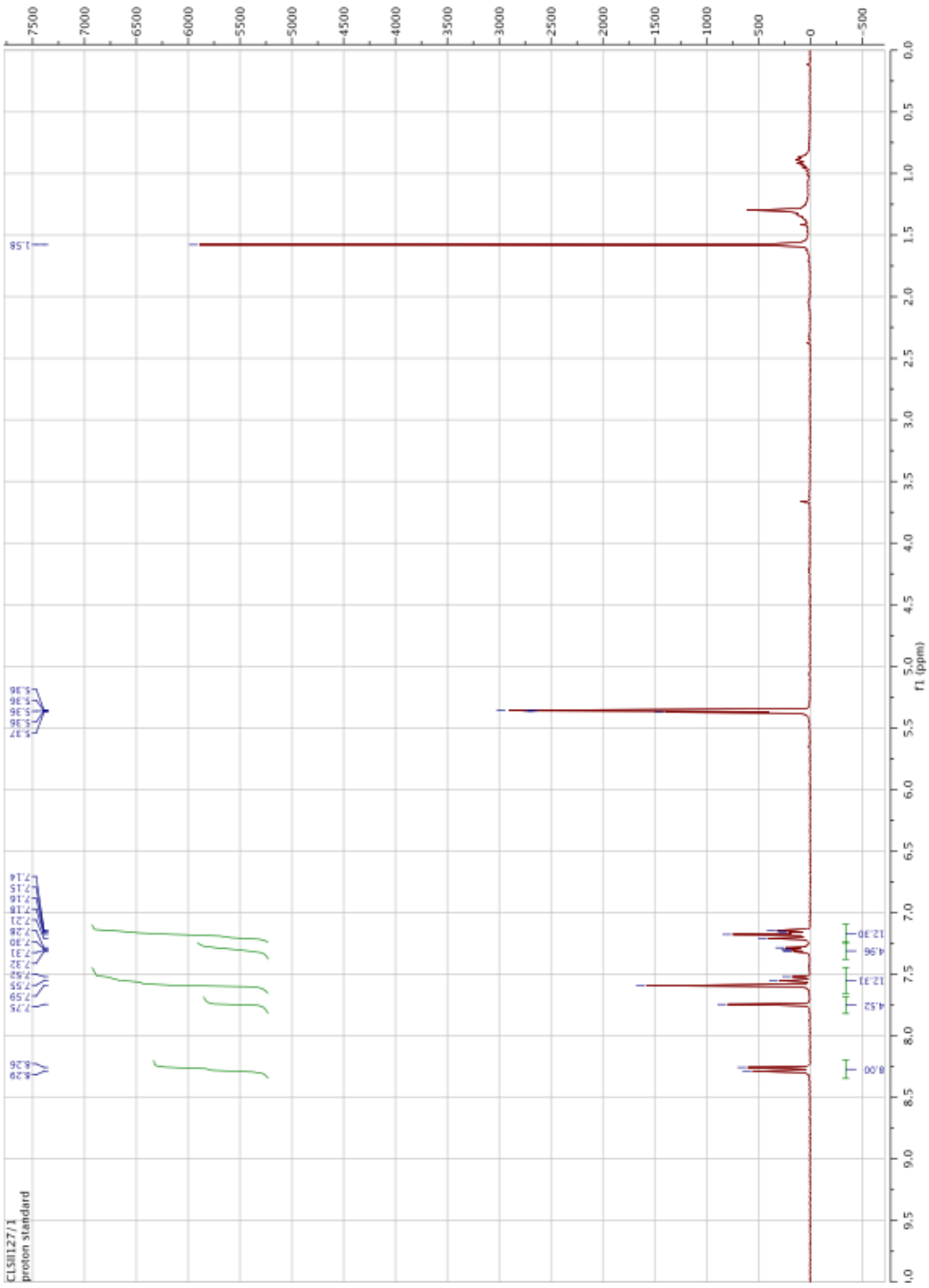

Figure A.18. ^{1}H NMR spectra in CD_2Cl_2 of **2.14**

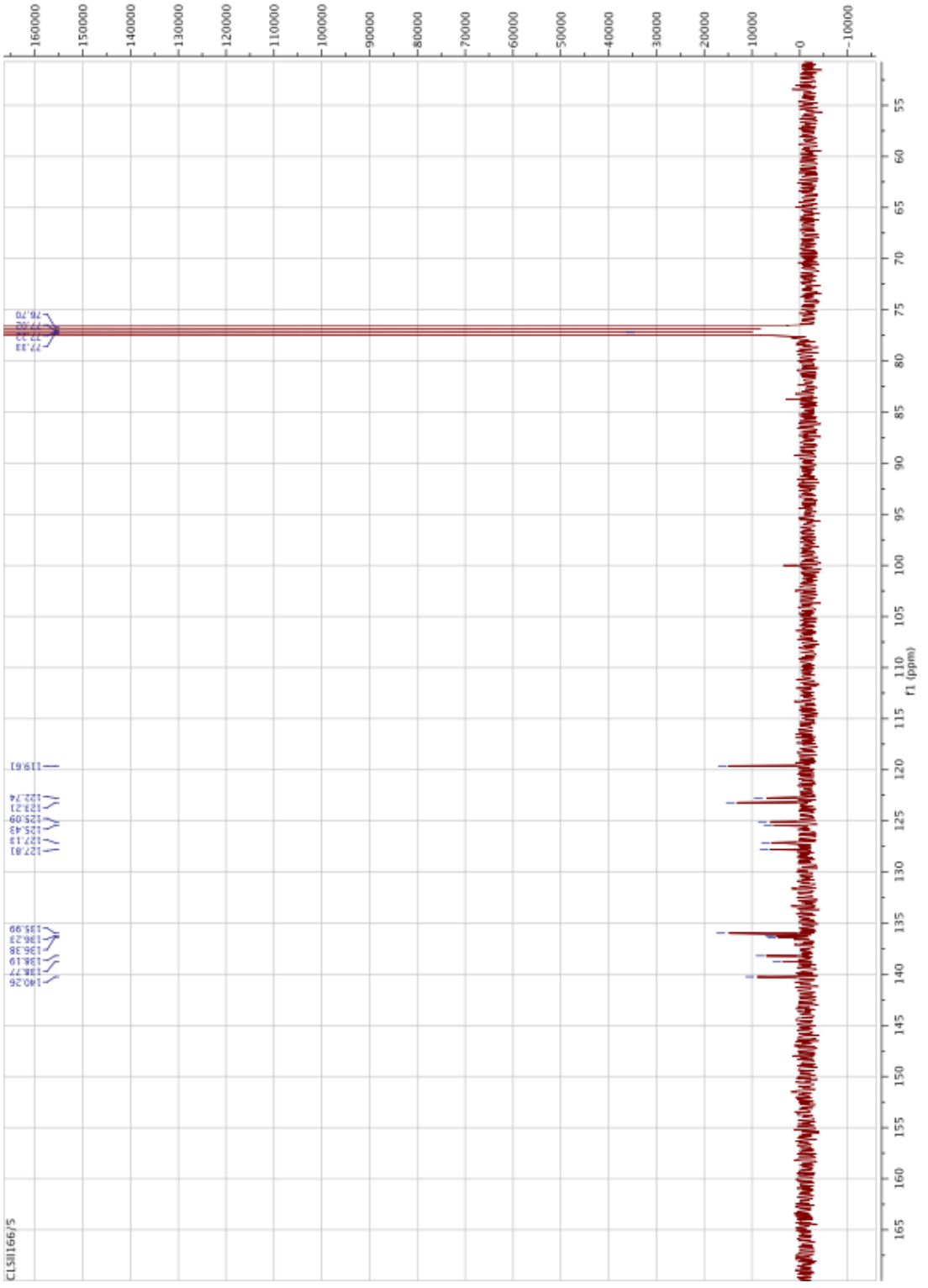

Figure A.19. ^{13}C NMR spectra in CD_2Cl_2 of **2.14**

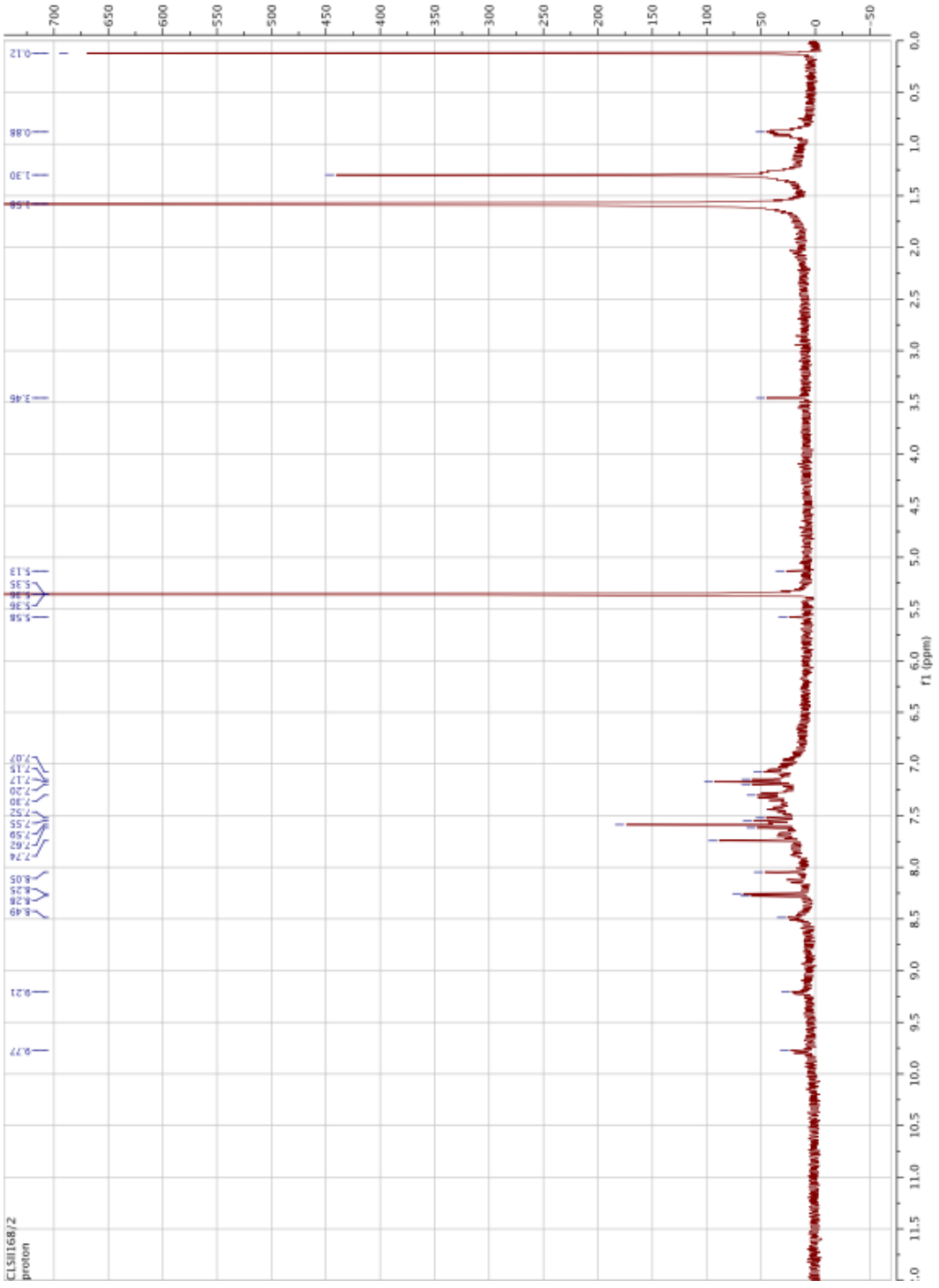

Figure A.20. ^{1}H NMR spectra in CD_2Cl_2 of **2.9** (after photocyclization).

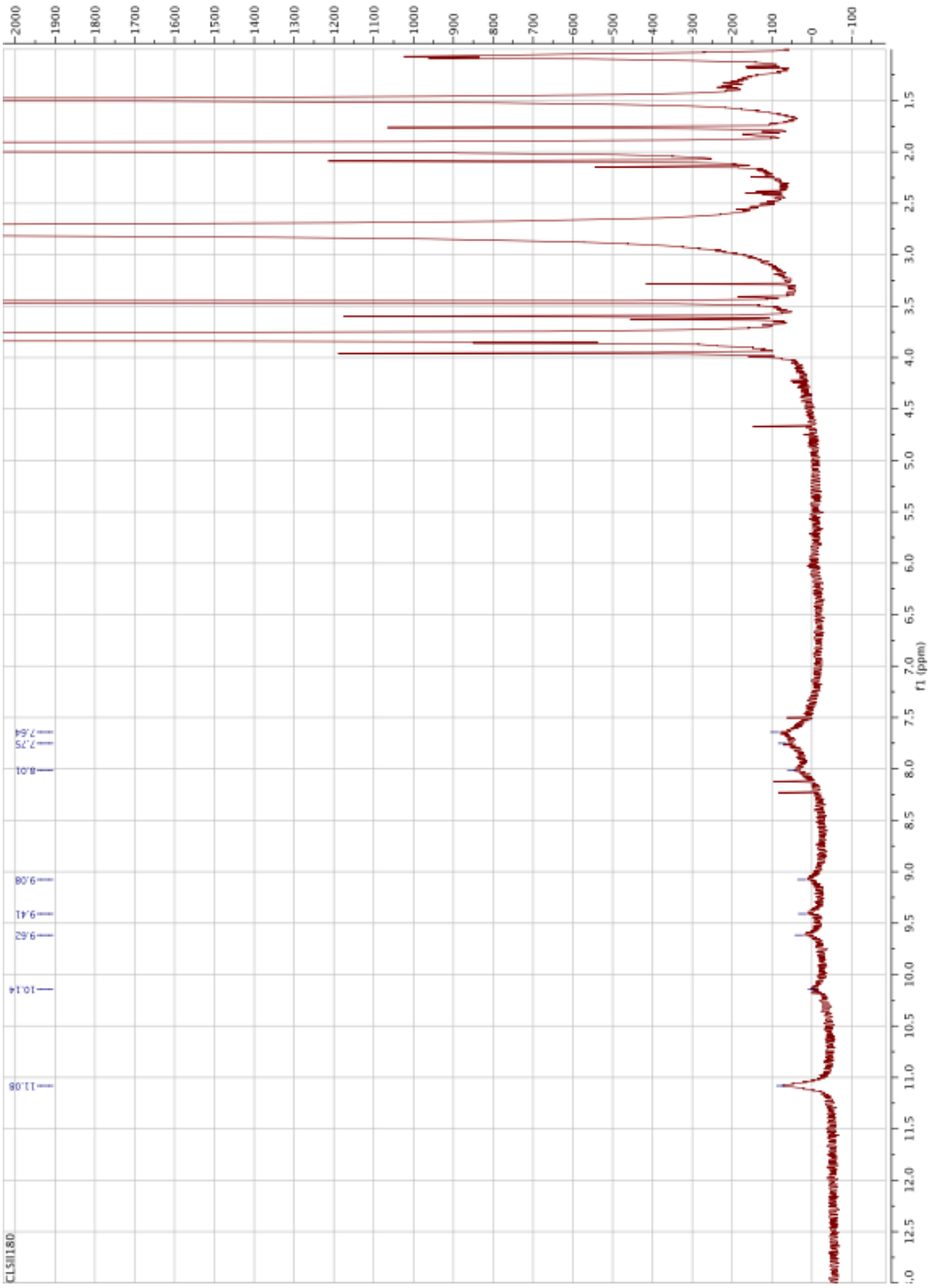

Figure A.21. ^{1}H NMR spectra in d8-tetrahydrofuran of **2.9** (after Scholl conditions).

Appendix B. Supplemental Information for Chapter 3

B.1 Conductance Data

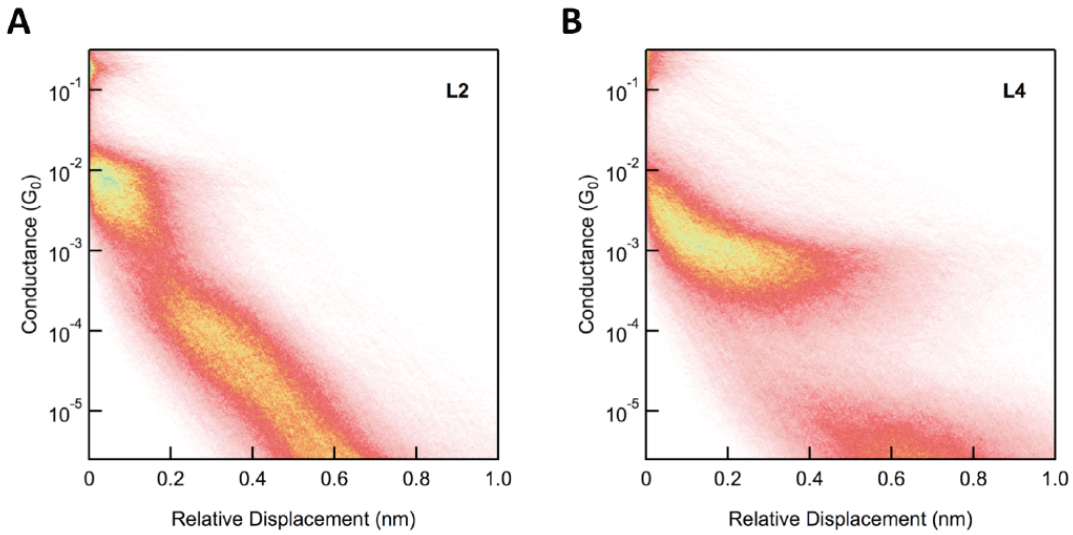

Figure B.1. Two-dimensional histograms showing ligand conductance as a function of STM tip-sample displacement for compounds (A) **L3.2** and (B) **L3.4**. These histograms are generated using a logarithmic binning with 10 bins/decade. The displacement dimension was binned linearly. The color scale indicates the average number of counts per trace in a given conductance-displacement bin.

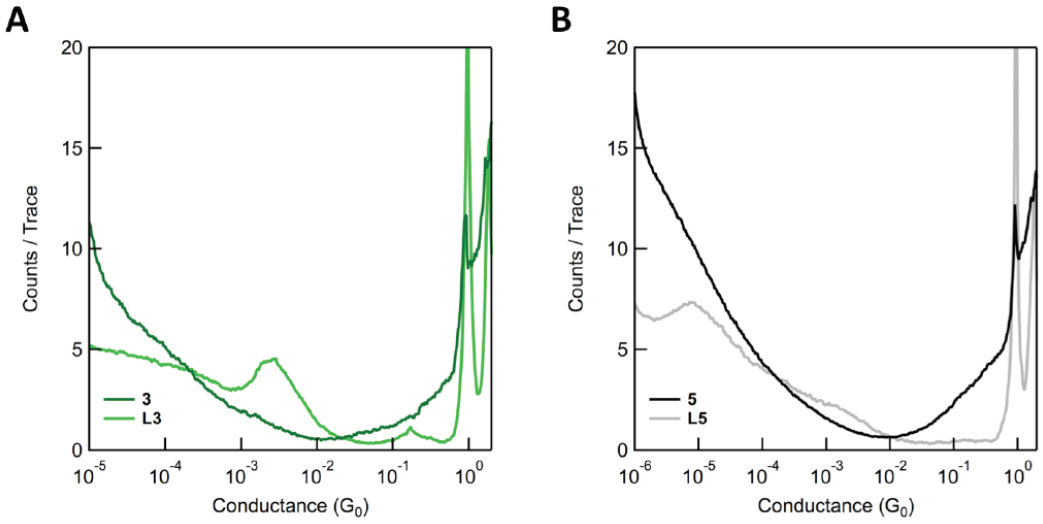

Figure B.2. One-dimensional logarithm-binned conductance histograms of (A) **3.3** (dark green) and **L3.3** (light green) and (B) **3.5** (black) and **L3.5** (grey). Bin size is 100/decade.

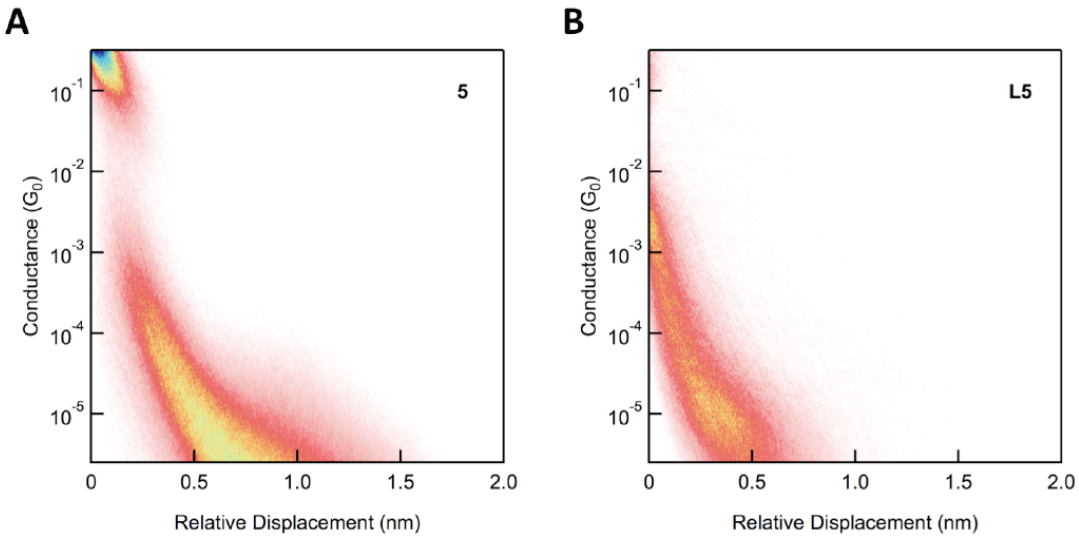

Figure B.3. Two-dimensional histograms showing conductance as a function of STM tip-sample displacement for compounds (A) **3.5** and (B) **L3.5**. These histograms are generated using a logarithmic binning with 10 bins/decade. The displacement dimension was binned linearly. The color scale indicates the average number of counts per trace in a given conductance-displacement bin.

B.2 UV-vis Absorption Spectroscopy

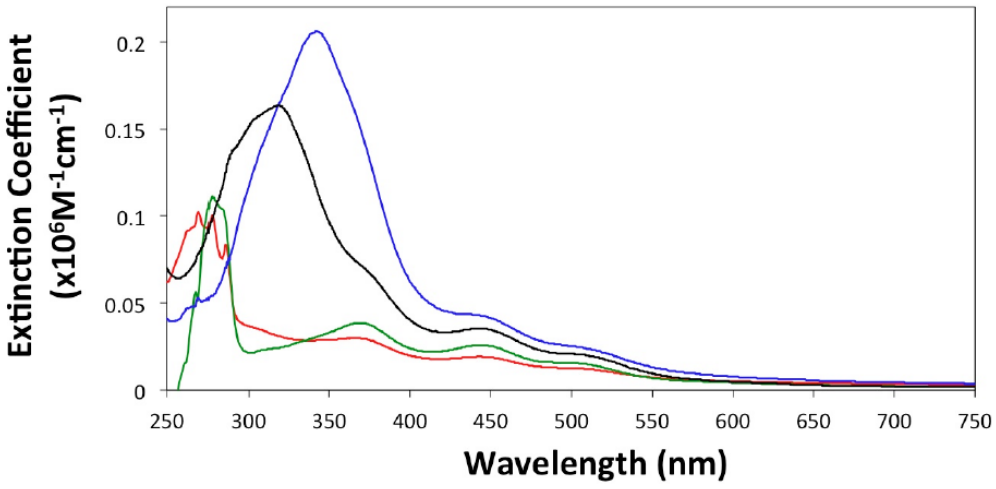

Figure B.4. UV-vis spectra of clusters **3.2**-**3.5** taken in dry and degassed THF with the following concentrations: **3.2**, 5.5 μM (red); **3.3**, 5.8 μM (green); **3.4**, 3.3 μM (blue); **3.5**, 3.3 μM (black)

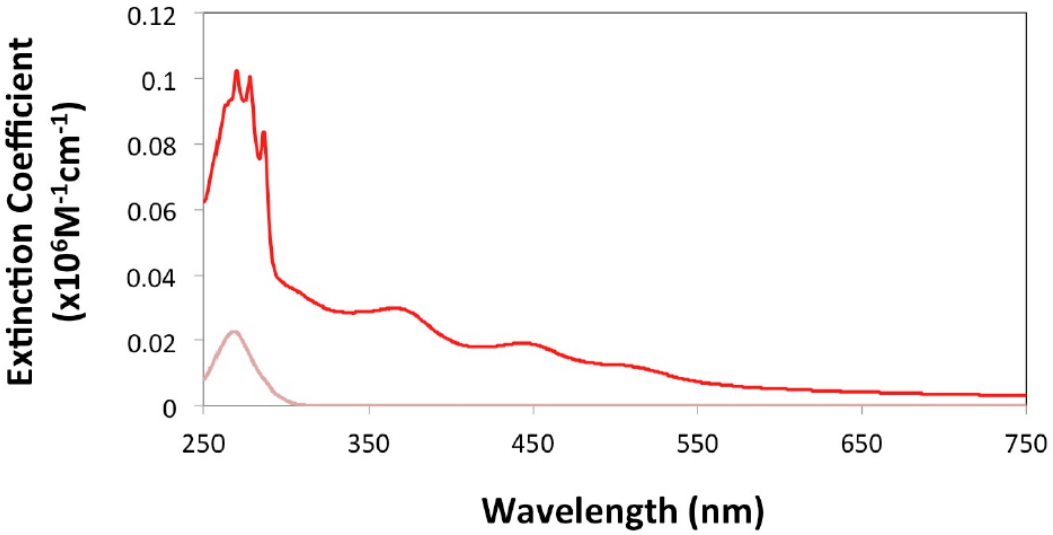

Figure B.5. UV-vis spectra taken in dry and degassed THF with the following concentrations: **3.2**, 5.5 μM (red); **L3.2**, 26.0 μM (pink).

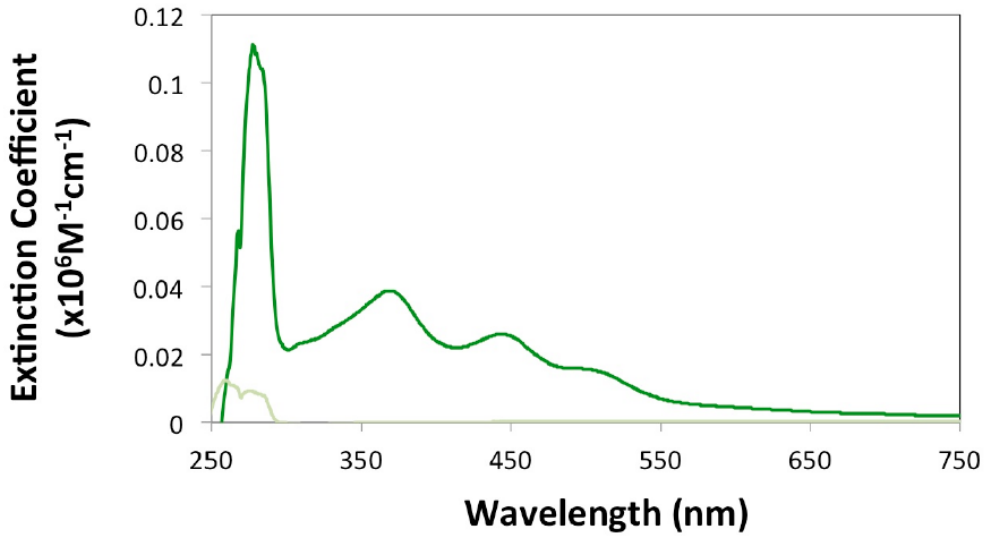

Figure B.6. UV-vis spectra taken in dry and degassed THF with the following concentrations: **3.3**, 5.8 μM (dark green); **L3.3**, 51.0 μM (light green).

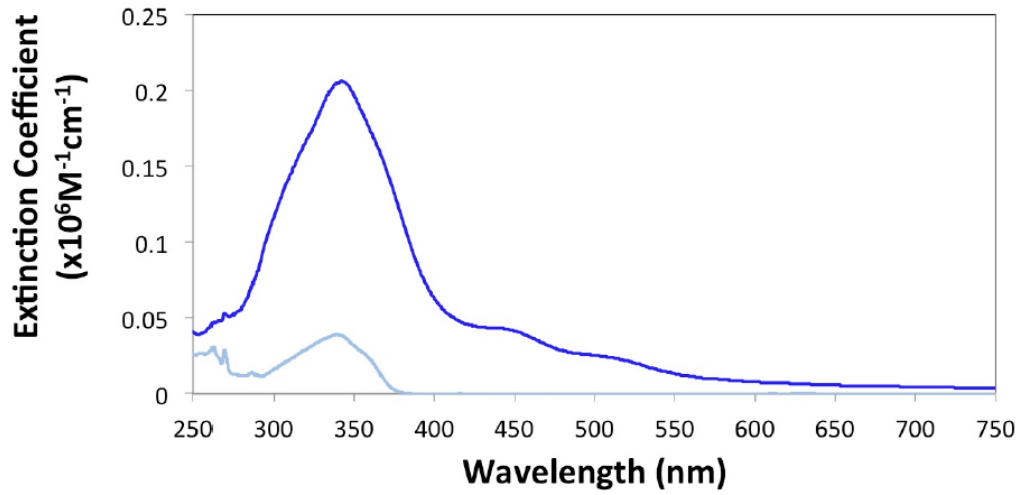

Figure B.7. UV-vis spectra taken in dry and degassed THF with the following concentrations: **3.4**, 3.3 μM (dark blue); **L3.4**, 4.1 μM (light blue).

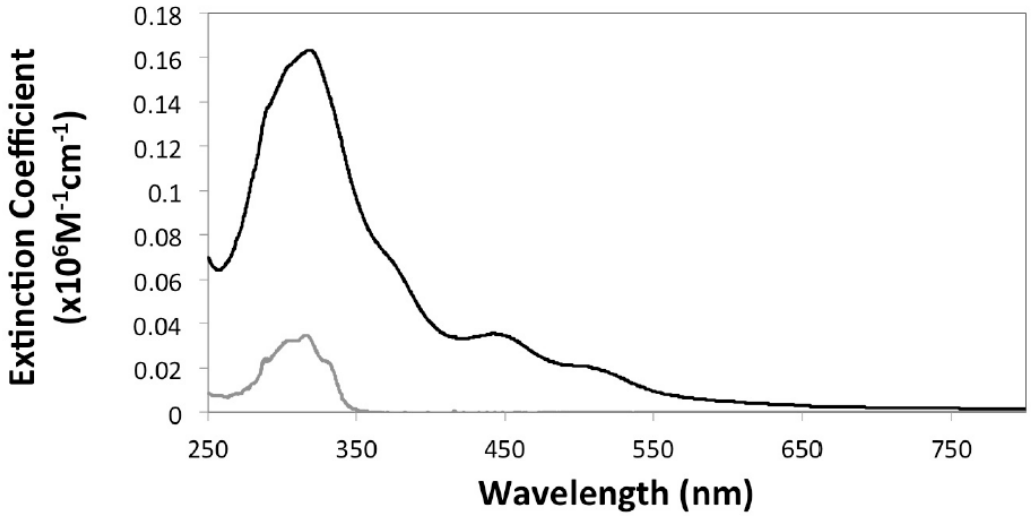

Figure B.8. UV-vis spectra taken in dry and degassed THF with the following concentrations: **3.5**, 3.3 μM (black); **L3.5**, 2.9 μM (gray).

B.3 Cyclic Voltammetry

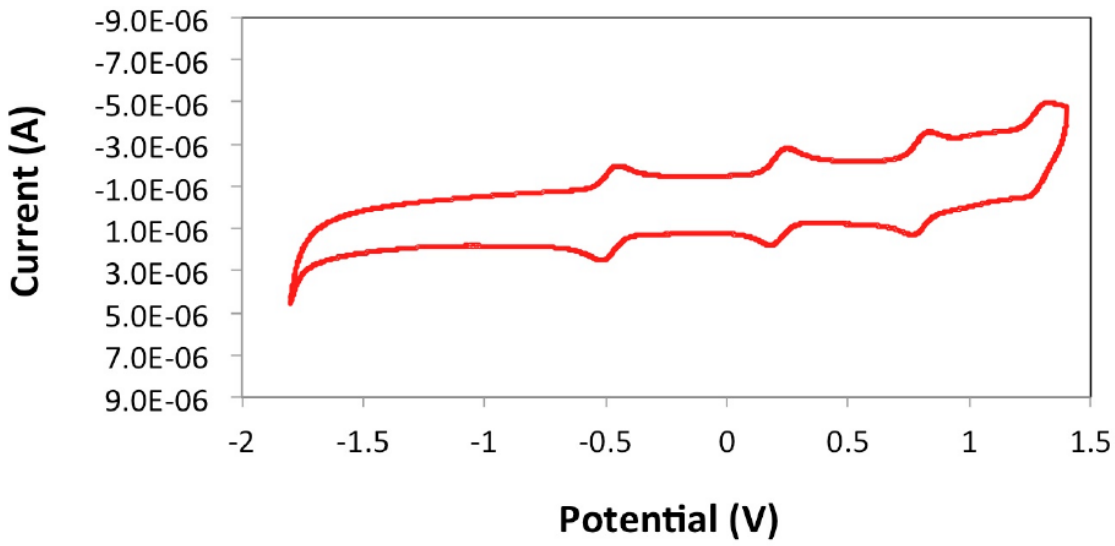

Figure B.9. CV trace of **3.2** in 0.1 M $TBAPF_6$ in dichloromethane vs. $Ag^+/AgCl$.

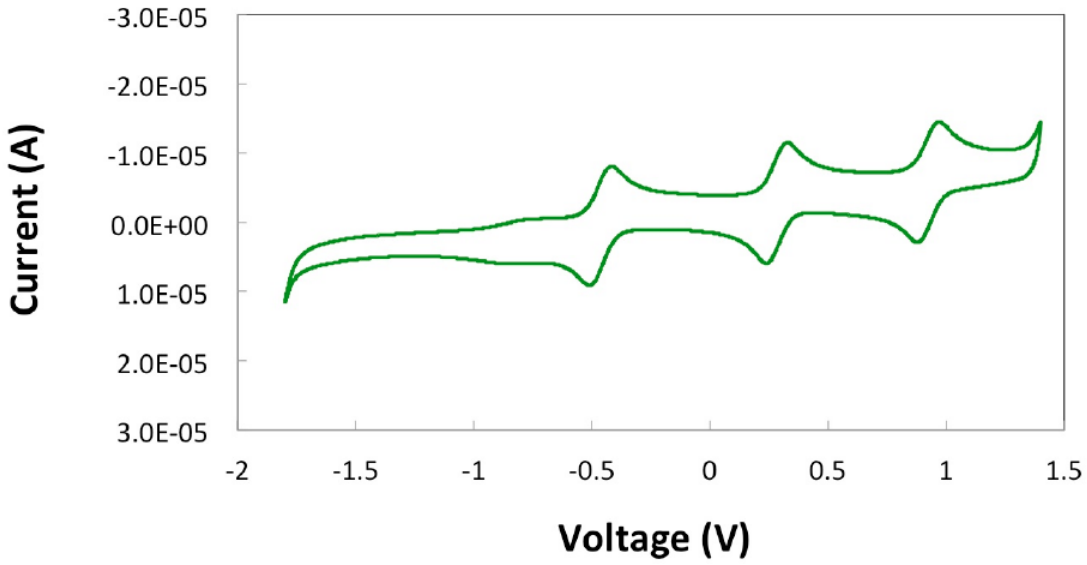

Figure B.10. CV trace of **3.3** in 0.1 M $TBAPF_6$ in dichloromethane vs. $Ag^+/AgCl$.

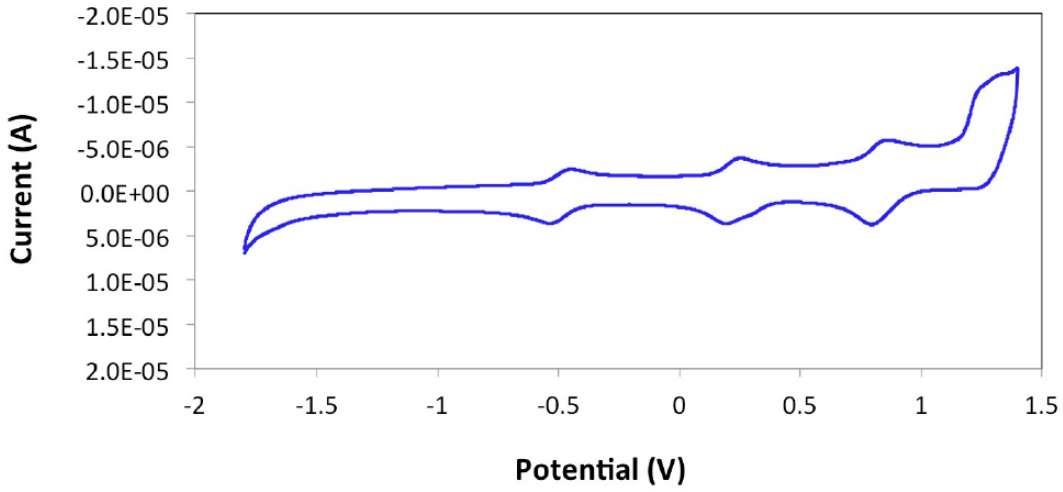

Figure B.11. CV trace of **3.4** in 0.1 M $TBAPF_6$ in dichloromethane vs. Ag^+/AgCl.

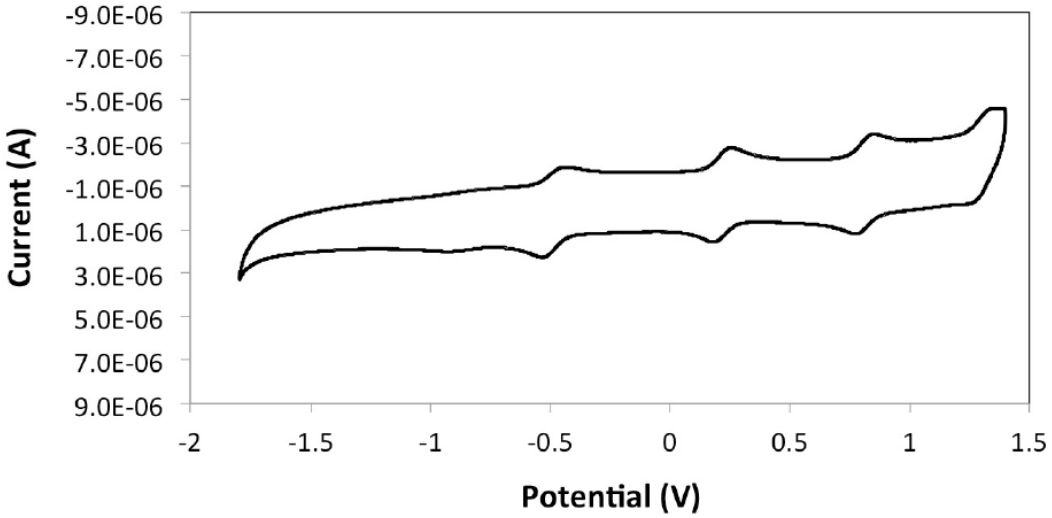

Figure B.12. CV trace of **3.5** in 0.1 M $TBAPF_6$ in dichloromethane vs. Ag^+/AgCl.

B.3 Crystallography

Table B.1. Selected crystallographic data for clusters **3.1**-**3.3**.

Compound	**1**	**2**	**3**
Formula	$C_{36}H_{90}Co_6P_6Se_8$	$C_{66}H_{102}Co_6P_6S_6Se_8$	$C_{66}H_{102}Co_6P_6S_6Se_8$
MW	1694.16	2258.98	2258.98
Lattice type	Hexagonal	Monoclinic	Triclinic
Space group	$R\bar{3}$	$C2/c$	$P\bar{1}$
a (Å)	17.1179(2)	27.8535(4)	11.7100(4)
b (Å)	17.1179(2)	16.8649(2)	13.1148(4)
c (Å)	19.5825(3)	21.5166(2)	15.1233(5)
α (°)	90	90	73.504(1)
β (°)	90	125.605(1)	74.179(2)
γ (°)	120	90	68.884(1)
V (Å^3)	4969.35(11)	8217.8(2)	2039.40(12)
Z value	3	4	1
D_{calc} (g cm^{-3})	1.698	1.826	1.839
T (K)	298	100	100
GOF on F^2	1.07	1.03	1.03
R_1 [$F^2 > 2\sigma(F^2)$]	0.031	0.033	0.054
wR_2 (all data)	0.086	0.080	1.151

Table B.2. Selected crystallographic data for clusters **3.4** and **3.5**.

Compound	**4**	**5**
Formula	$C_{114}H_{138}Co_6P_6S_6Se_8$, $2(C_7H_8)$	$C_{108}H_{126}Co_6P_6Se_8$
MW	3056.02	2595.17
Lattice type	Monoclinic	Hexagonal
Space group	$P2_1/c$	$R\bar{3}$
a (Å)	11.8387(2)	17.7839(2)
b (Å)	45.8633(7)	17.7839(2)
c (Å)	11.7945(2)	28.5185(4)
α (°)	90	90
β (°)	93.493(7)	90
γ (°)	90	120
V (Å^3)	6392.07(18)	7811.08(17)
Z value	2	3
D_{calc} (g cm^{-3})	1.588	1.655
T (K)	100	100
GOF on F^2	1.23	1.06
R_1 [$F^2 > 2\sigma(F^2)$]	0.045	0.045
wR_2 (all data)	0.094	0.106

B.4 DFT Calculations

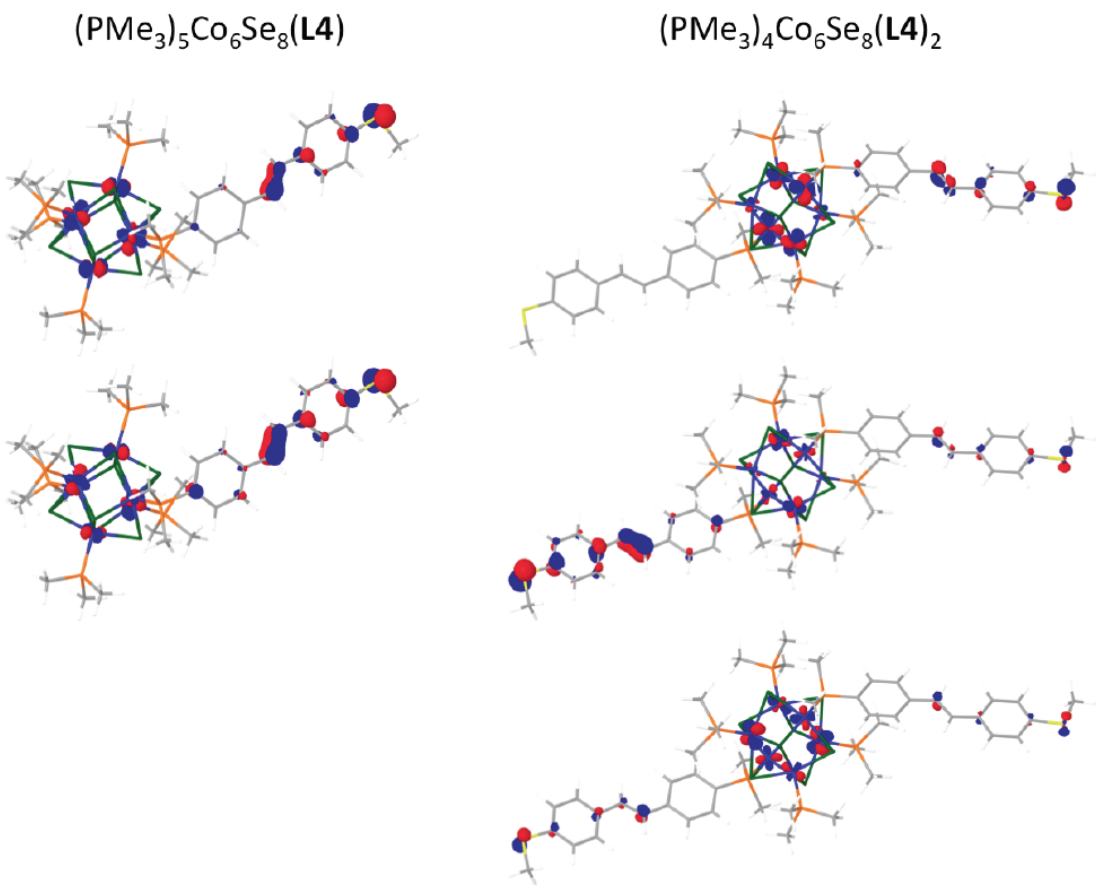

Figure B.13. Model computational studies of cluster **3.4** using density functional theory. The orbitals associated with the sulfur pπ lone pairs for the models $(PMe_3)_5Co_6Se_8$(**L3.4**) and $(PMe_3)_4Co_6Se_8$(**L3.4**)$_2$ are shown.

Appendix C. Supplemental Information for Chapter 4

C.1 Conductance Data for Spin Cast Films

Table C.1. Summary of contact resistance and sheet resistance of 7 spin cast films of cluster **4.1**. Cluster **4.2** films showed no measurable conductance.

	Contact R (MΩ)	Sheet R (MΩ)
Chip 1	57.2	487
Chip 2	103	1.21×10^{3}
Chip 3	98.7	96.7
Chip 4	134	1.03×10^{3}
Chip 5	269	1.09×10^{3}
Chip 6	32.3	212
Average sheet resistance of seven chips: 833 MΩ		

C.2 Conductance Data for Drop Cast Films

Table C.2. Summary of contact resistance and sheet resistance of six drop cast films of cluster **4.1**. Cluster **4.2** films showed no measurable conductance.

	Contact R (MΩ)	Sheet R (MΩ)
Chip 1	5.61	38.6
Chip 2	6.15	58.9
Chip 3	6.35	55.3
Chip 4	27.0	57.5
Chip 5	34.7	114
Chip 6	30.0	161
Average sheet resistance of seven chips: 80.9 MΩ		

C.3 Optical Microscope Images of Spin Cast and Drop Cast Films

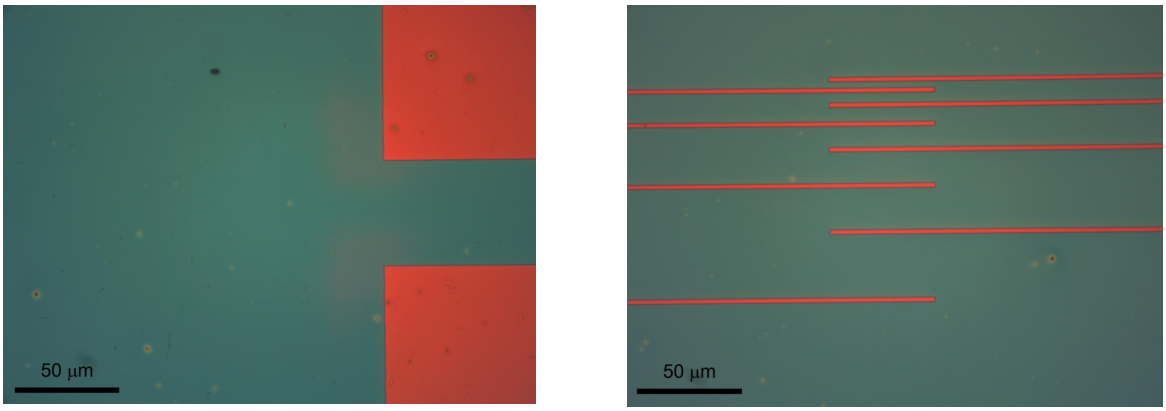

Figure C.1. Optical microscope images of spin cast films of **4.2**. Scale bar = 50 µm.

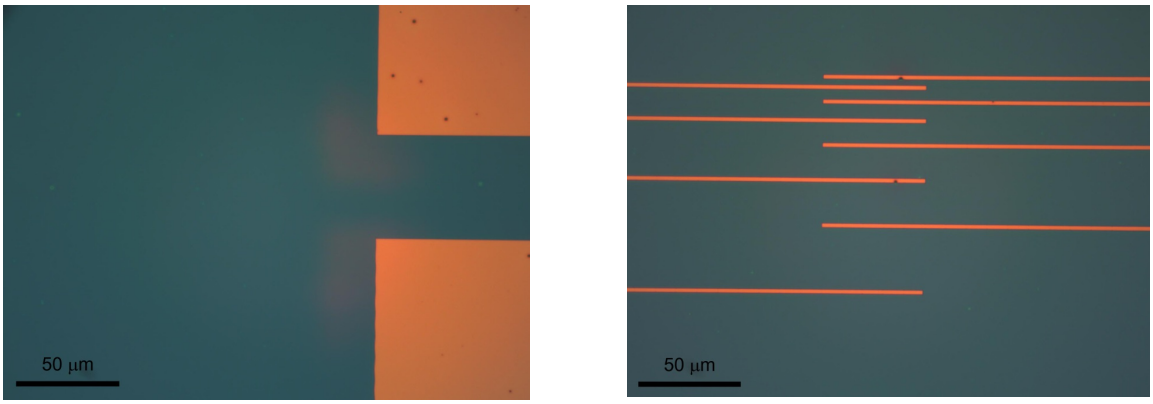

Figure C.2. Optical microscope images of spin cast films of **4.1**. Scale bar = 50 µm.

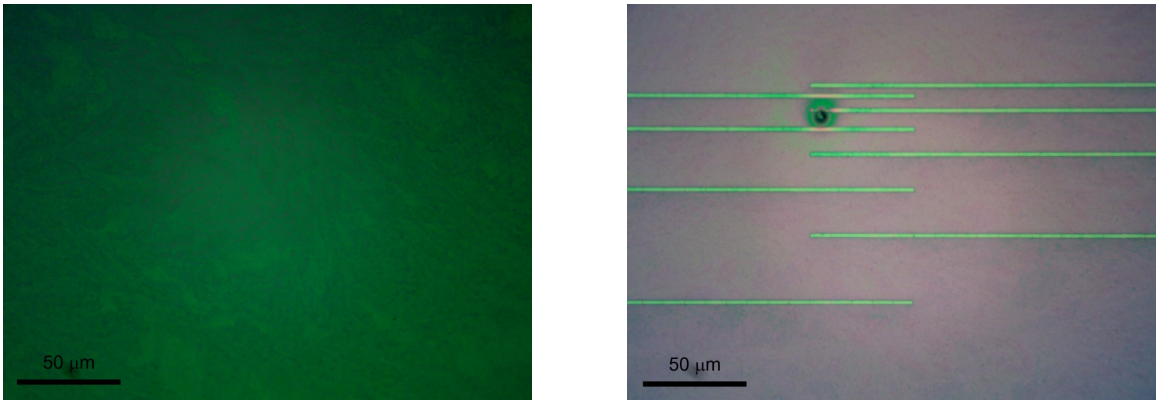

Figure C.3. Optical microscope images of drop cast films of **4.2**. Scale bar = 50 µm.

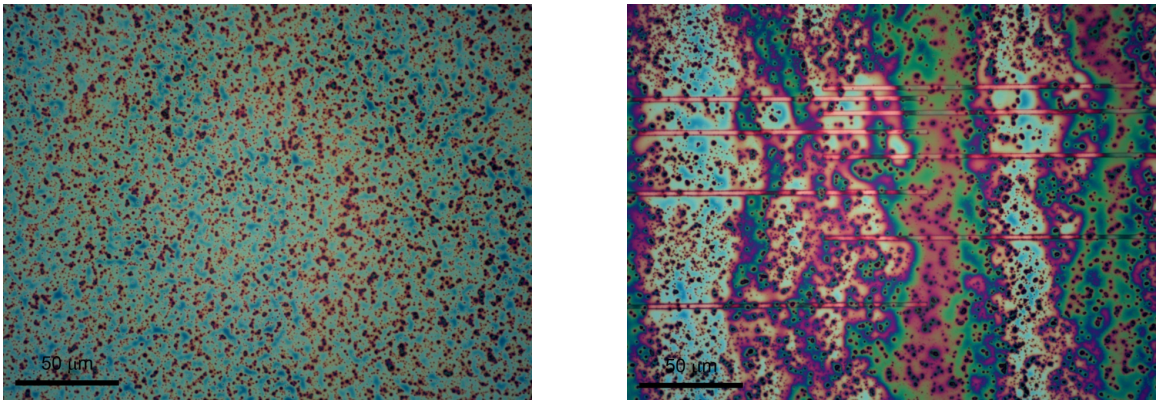

Figure C.4. Optical microscope images of drop cast films of **4.1**. Scale bar = 50 µm.

C.4 Grazing Incidence X-Ray Diffraction (GIXD)

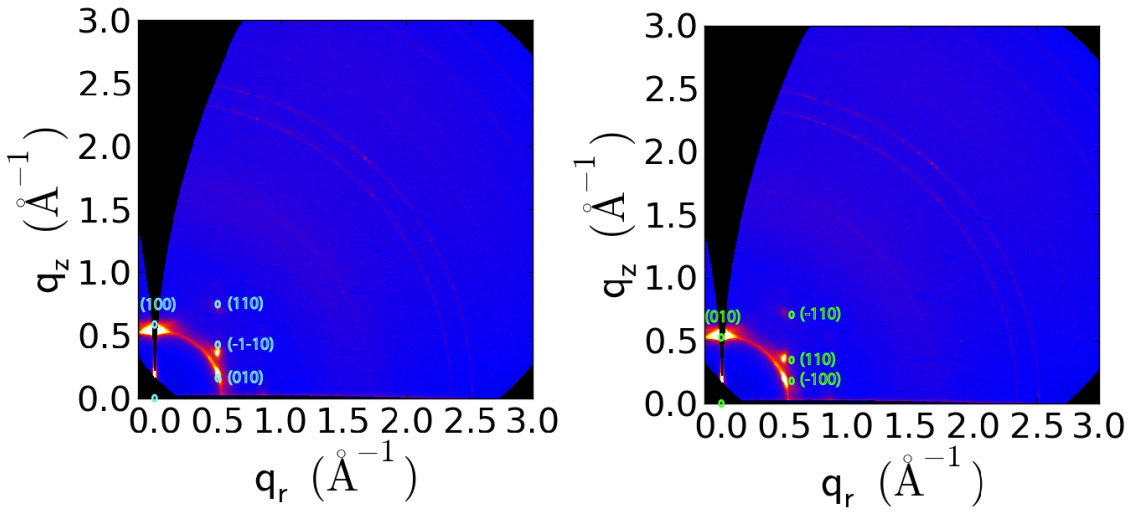

Figure C.5. Two-dimensional reciprocal (Q-) space diffraction patterns for spin cast thin film of **4.2** with 2-D patterns computed from lattice parameters obtained with single crystal measurements of **4.2** overlaid as white circles and peaks indexed for unit cell orientations with either the a-axis ((100), left) or b-axis ((010), right) oriented along the surface normal.

C.5 Thermal Annealing Data

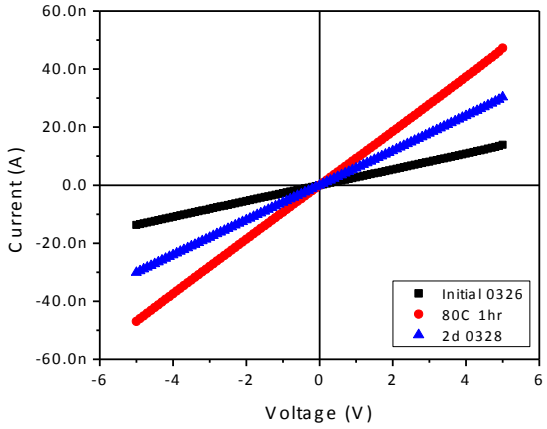

Figure C.6. I-V plot of a spin cast film of **4.1** before (black) and after (red) annealing for one hour at 80°C. Blue curve is the conductance of the film of **4.**1 after two days. Spin cast thin film of **4.2** showed no measureable conductance before or after annealing.

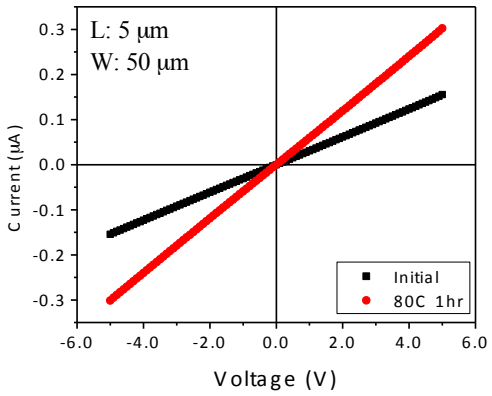

Figure C.7. I-V plot of a drop cast film of **4.1** before (black) and after (red) annealing for one hour at 80°C. Drop cast thin film of **4.2** showed no measureable conductance before or after annealing.

Table C.3. Summary of contact resistance and sheet resistance before and after annealing for spin cast (green) and drop cast (purple) films.

	Contact Resistance	Sheet Resistance
Before Annealing (Spin Cast)	**174 MΩ**	**1.78 MΩ**
After Annealing (Spin Cast)	**48.2 MΩ**	**0.522 MΩ**
Before Annealing (Drop Cast)	**27.0 MΩ**	**57.5 MΩ**
After Annealing (Drop Cast	**14.1 MΩ**	**29.3 MΩ**

C.6 Oxygen Exposure Data

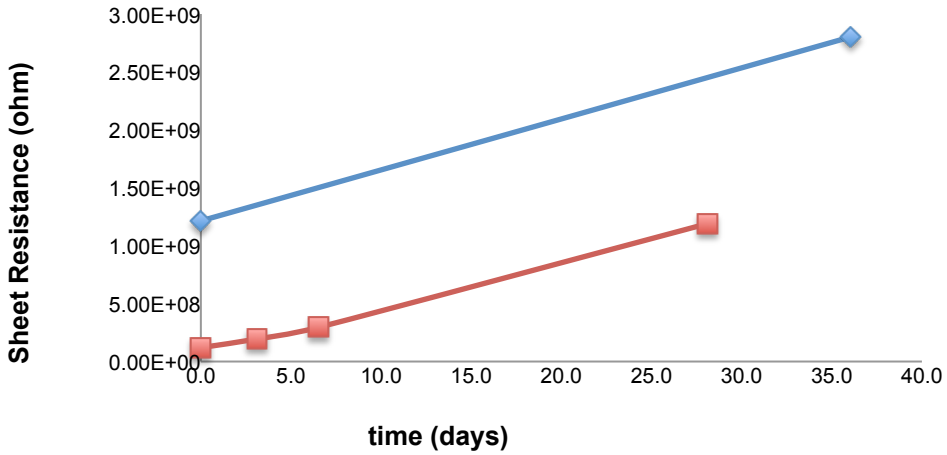

Figure C.8. Sheet resistance of thermally annealed films kept in a glovebox over many days. Blue curve is time dependence of spin cast film of **4.1**. Red curve is time dependence of drop cast film of **4.1**.

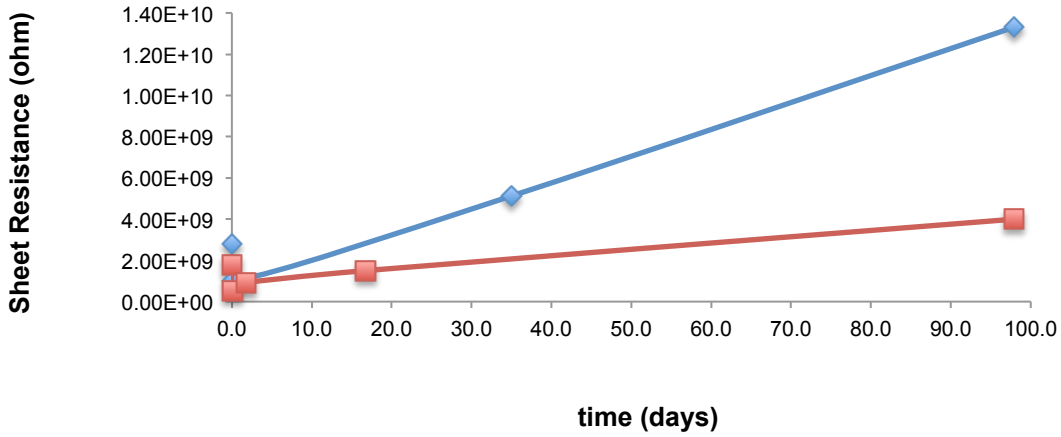

Figure C.9. Sheet resistance of thermally annealed films kept in a glovebox over many days. Curves represent data from different spin cast films.

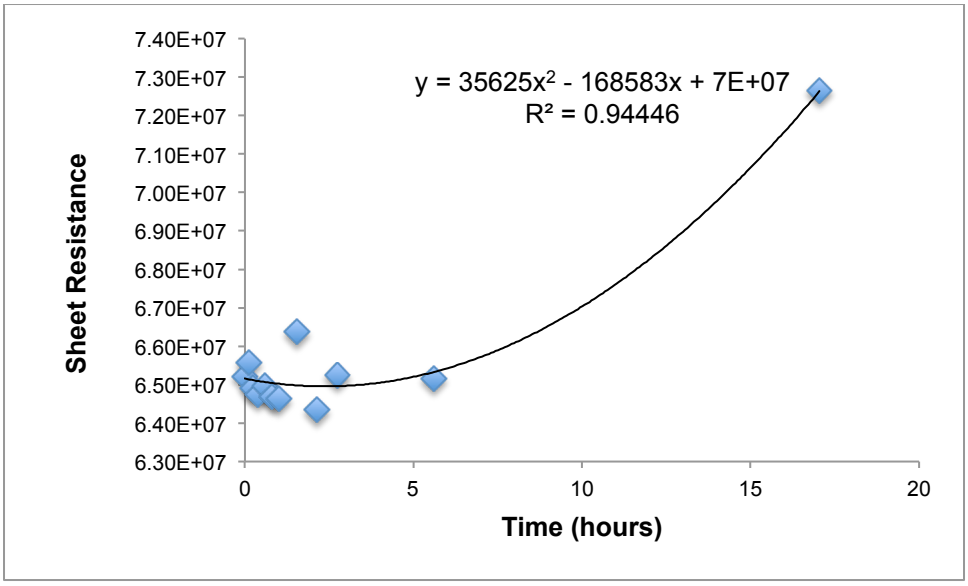

Figure C.10. Short-term time dependence of drop cast films of **4.1**.

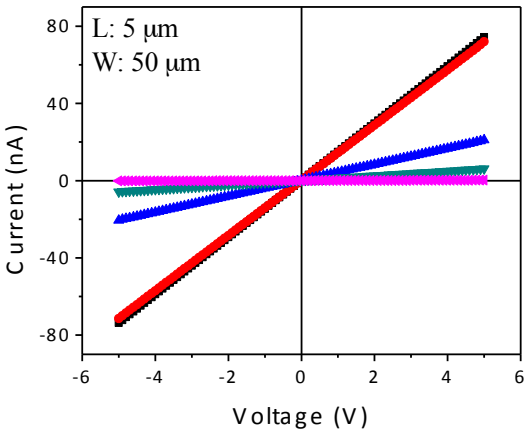

Figure C.11. Measured I-V curve of drop cast films of **4.1** with increasing exposure to oxygen. Initial conductance (black), 5 seconds O_2 exposure (red), 20 seconds O_2 exposure (blue), 2 minutes O_2 exposure (green), 10 minutes O_2 exposure (pink)

C.7 UV-vis Spectroscopy

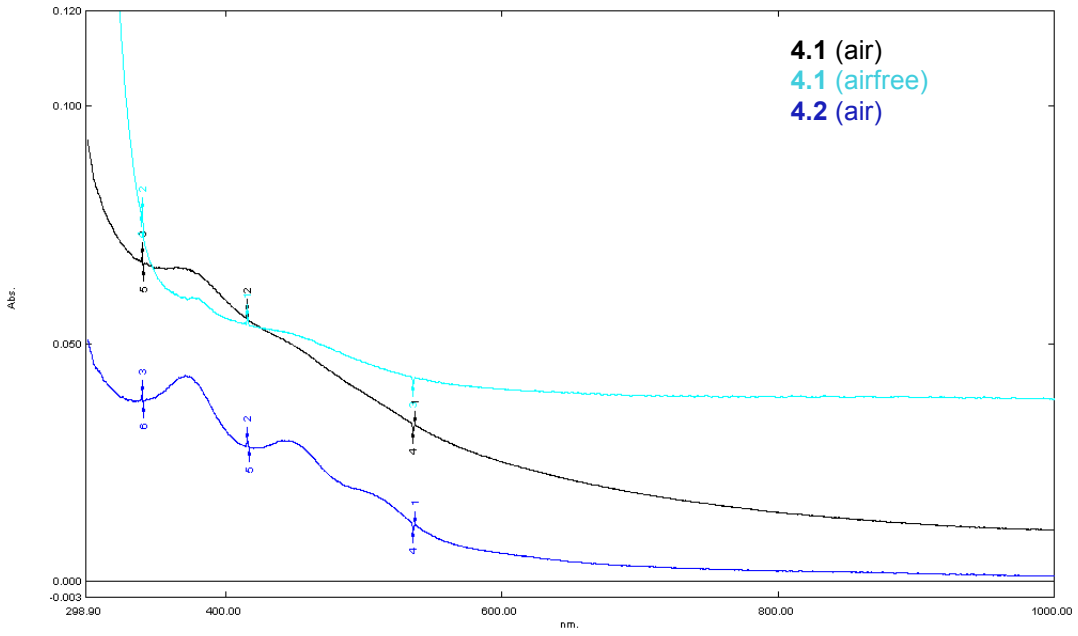

Figure C.12. Spin cast thin films of **4.1** in air (black) and encapsulated in nitrogen (light blue) and of **4.2** in air.

C.8 Atomic Force Microscopy

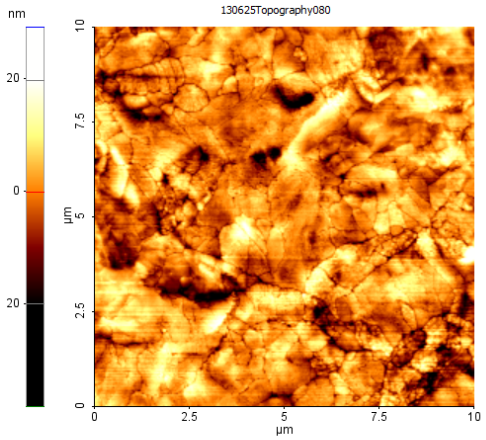

Figure C.13. AFM image of a drop cast film of **4.2**. AFM data for the drop cast film of **4.1** was extremely rough with fluctuations >150 nm.

C.9 OTS Treated Device Conductance

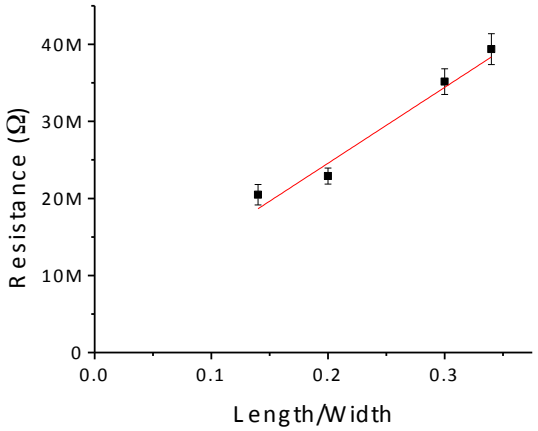

Figure C.14. Film of drop cast **4.1** on octadecyltrichlorosilane (OTS) treated substrates. Plot of resistance versus length to width ratio. Sheet resistance is 98.5 MΩ and contact resistance is 4.87 MΩ. Film thickness is unknown.

Appendix D. Supplemental Information for Chapter 5

D.1 Crystallography

Crystals of **5.4**, **5.6**, and **5.7** were measured on a Bruker SMART CCD APEX II diffractometer (Bruker. *APEX2*. Version 2.0-2. Bruker AXS Inc., Madison, Wisconsin, USA **2006**) using a fine-focus sealed-tube graphite monochromator Cu K_α source (λ = 1.54178 Å). Data were collected and integrated using the Bruker SAINT software package (Bruker. *SAINT*. Version 7.23 A. Bruker AXS Inc., Madison, Wisconsin, USA **2005**). The structures were solved using SHELXTL.

The single crystal x-ray diffraction data of **5.5** was collected using an Oxford Diffraction Xcalibur-2 CCD diffractometer with graphite monochromatized Mo K_α radiation. The crystal was mounted in a cryoloop under Paratone-N oil and cooled to 100K with an Oxford Diffraction Cryojet system. The collected frames were analyzed using the Crysalis program package. Integrated intensities were corrected for absorption using the Gaussian integration method.

Table D.1. Select crystallographic data for clusters **5.5** and **5.4**.

	$Ni_7Te_5(P(NMe_2)_3)_6$ (5.5)	$Ni_7Te_5(P(i\text{-}Pr)_3)_6$ (5.4)
chemical formula	$C_{36}H_{108}N_{18}Ni_7P_6Te_5$	$C_{54}H_{126}Ni_7P_6Te_5$
***a*, Å**	38.1015(12)	20.0164(17)
***b*, Å**	21.2045(7)	20.0164(17)
***c*, Å**	26.2160(8)	34.069(3)
α, deg	90	90.00
β, deg	95.063(3)	90.00
γ, deg	90	120.00
***V*, Å^3**	21097.8	11821.2
Z	0	6
formula weight	2028.1	2010.3
space group	C c	R -3
R(F_o or F_o^2)		7.7

Table D.1. Select crystallographic data for clusters **5.6** and **5.7**.

	$Ni_{28}Te_{17}(PEt_3)_{12}$ (5.7)	$Ni_6Te_5DEPE_3$ (5.6)
chemical formula	$C_{72}H_{180}Ni_{28}P_{12}Te_{17}$	$C_{30}H_{68}Ni_6P_6Te_5$
***a*, Å**	25.2371(4)	19.5354(7)
***b*, Å**	25.2371(4)	10.5279(4)
***c*, Å**	34.7358(6)	11.6637(4)
α, deg	90	90
β, deg	90	90
γ, deg	120	90
***V*, Å^3**	19159.6	2398.84
Z	6	2
formula weight	5231.02	1604.9
space group	R -3	$Pmn2_1$
R(F_o or F_o^2)	7.1	5.25